USGS
science for a changing world

هيئة المساحة الجيولوجية السعودية
SAUDI GEOLOGICAL SURVEY

Ambient Seismic Noise Tomography of the Kingdom of Saudi Arabia

Chapter N of
Active Volcanism on the Arabian Shield—Geology, Volcanology, and Geophysics of Northern Harrat Rahat and Vicinity, Kingdom of Saudi Arabia

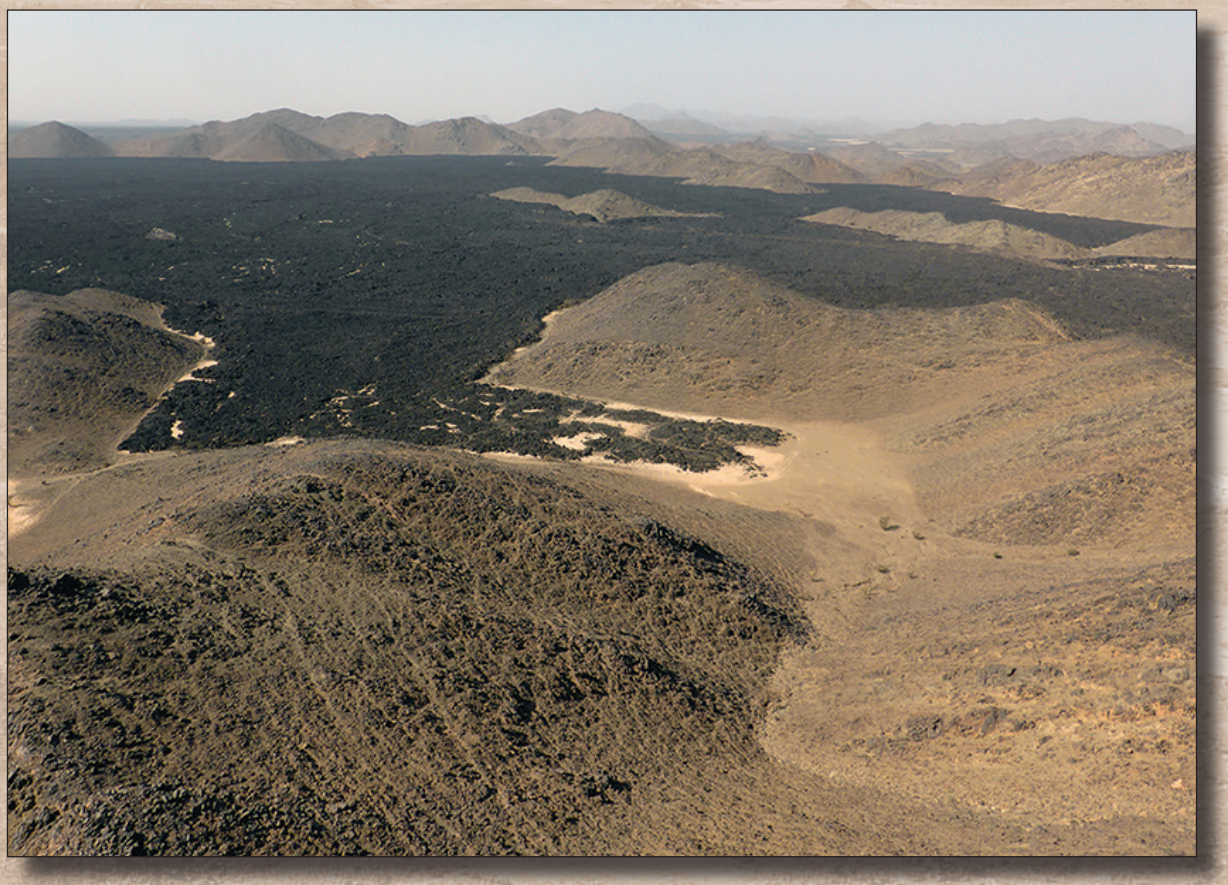

U.S. Geological Survey Professional Paper 1862
Saudi Geological Survey Special Report SGS–SP–2021–1

U.S. Department of the Interior
U.S. Geological Survey

Cover. Oblique aerial photograph looking northwest toward the basalt of Southern Fingers lavas that fill low topography between hills of metamorphosed volcanic and volcaniclastic rocks belonging to the Proterozoic Al Ays Group of the Hijaz terrane. The basalt of the Southern Fingers is one of three large, nearly contemporaneous basalt flows (collectively called the Five Fingers lavas) that erupted about 24 thousand years ago at the northeast edge of Harrat Rahat. U.S. Geological Survey photograph by A.T. Calvert, February 6, 2017. Background image shows northern Harrat Rahat lava flows, maars, and lava domes. U.S. Geological Survey photograph by Andrew Calvert, January 25, 2012..

Ambient Seismic Noise Tomography of the Kingdom of Saudi Arabia

By Francesco Civilini, Walter D. Mooney, Martha K. Savage, and John Townend

Chapter N of

Active Volcanism on the Arabian Shield—Geology, Volcanology, and Geophysics of Northern Harrat Rahat and Vicinity, Kingdom of Saudi Arabia

Edited by Thomas W. Sisson, Andrew T. Calvert, and Walter D. Mooney

U.S. Geological Survey Professional Paper 1862
Saudi Geological Survey Special Report SGS–SP–2021–1

U.S. Department of the Interior
U.S. Geological Survey

U.S. Geological Survey, Reston, Virginia: 2023

For more information on the USGS—the Federal source for science about the Earth, its natural and living resources, natural hazards, and the environment—visit https://www.usgs.gov/ or call 1–888–ASK–USGS (1–888–275–8747).

For an overview of USGS information products, including maps, imagery, and publications, visit https://store.usgs.gov/.

Suggested citation:
Civilini, F., Mooney, W.D., Savage, M.K., and Townend, J., 2023, Ambient seismic noise tomography of the Kingdom of Saudi Arabia, chap. N *of* Sisson, T.W., Calvert, A.T., and Mooney, W.D., eds., Active volcanism on the Arabian Shield—Geology, volcanology, and geophysics of northern Harrat Rahat and vicinity, Kingdom of Saudi Arabia: U.S. Geological Survey Professional Paper 1862 [also released as Saudi Geological Survey Special Report SGS–SP–2021–1], 57 p., https://doi.org/10.3133/pp1862N.

ISSN 2330-9612 (print)
ISSN 1044-7102 (online)

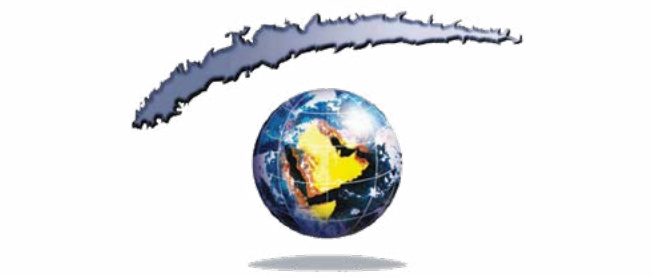

Ministry of Industry and Mineral Resources
BANDAR BIN IBRAHIM BIN ABDULLAH AL-KHORAYEF, Minister and SGS Chairman

Saudi Geological Survey
Abdullah bin Mufter Al-Shamrani, Chief Executive Officer

Saudi Geological Survey, Jiddah, Kingdom of Saudi Arabia: 2023

Contents

Figures

Tables

Conversion Factors

International System of Units to U.S. customary units

Multiply	By	To obtain
	Length	
centimeter (cm)	0.3937	inch (in.)
millimeter (mm)	0.03937	inch (in.)
meter (m)	3.281	foot (ft)
kilometer (km)	0.6214	mile (mi)
	Area	
square kilometer (km^2)	0.3861	square mile (mi^2)
	Rate	
kilometer per second (km/s)	0.6214	mile per second (mi/s)
	Density	
gram per cubic centimeter (g/cm^3)	62.4220	pound per cubic foot (lb/ft^3)

Temperature in degrees Celsius (°C) may be converted to degrees Fahrenheit (°F) as °F = (1.8 × °C) + 32.

Abbreviations

A.H.	in the year of the Hijra
AFTAN	automatic frequency-time analysis
C.E.	Common Era
FTAN	frequency-time analysis
Hz	hertz
M_L	local magnitude
M_w	moment magnitude
P-wave	compressional wave
RR	radial-radial (a cross-correlated component of the Green's function matrix)
SGS	Saudi Geological Survey
S-wave	shear wave
TT	tranvserse-transverse (a cross-correlated component of the Green's function matrix)
USGS	U.S. Geological Survey
V_P	P-wave velocity
V_P/V_S	P-wave to S-wave velocity
V_S	S-wave velocity
ZZ	vertical-vertical (a cross-correlated component of the Green's function matrix)

Active Volcanism on the Arabian Shield
Edited by T.W. Sisson, A.T. Calvert, and W.D. Mooney
U.S. Geological Survey Professional Paper 1862
Saudi Geological Survey Special Report SGS–SP–2021–1

Chapter N

Ambient Seismic Noise Tomography of the Kingdom of Saudi Arabia

By Francesco Civilini,[1] Walter D. Mooney,[1] Martha K. Savage,[2] and John Townend[2]

Abstract

Harrat Rahat is a Cenozoic volcanic field in the west-central part of the Kingdom of Saudi Arabia, 150 kilometers east of the Red Sea, and is the site of the most recent eruption in the country (1256 C.E.; 654 in the year of the Hijra). The city of Al Madīnah lies at the north end of Harrat Rahat, and its volcanic and seismic risks are frequently reassessed. In 2009 C.E. an earthquake swarm at Harrat Lunayyir, 200 km west-northwest of Al Madīnah, produced significant shaking and some building damage in nearby communities, which prompted a revision of seismic hazard models for the region. A network of seismic stations on this volcanically active western side of the Arabia Plate was installed, and stations were also added in the tectonically active northern part of the country. Although regional earthquakes may be used to determine the crustal structure of the western Arabia Plate, such crustal models are hindered by insufficient numbers of earthquakes in the stable plate interior. Tomography studies can be used to infer material properties of the subsurface, such as presence of partial melt, and are beneficial for volcanic hazard assessments. We use ambient seismic noise to compute Rayleigh and Love surface-wave dispersion maps between 5 and 12 second periods for a subset of seismic stations within and near northern Harrat Rahat. The surface-wave maps are inverted to produce shear-wave velocities using a neighborhood algorithm and interpolated into a pseudo three-dimensional model. The distributions of surface-wave and shear-wave velocities are heterogenous, varying from ±3–8 percent. However, low velocities are not restricted to Harrat Rahat. We observed a difference between Rayleigh- and Love-wave velocities that extends north of the site of the 1256 C.E. eruption and coincides with a low gravity anomaly. We obtain a shear-wave velocity increase of 10–15 percent between 15- and 25-kilometers depth, which is consistent with the presence of a transition between the felsic upper crust and the mafic lower crust of the Arabian Shield. The average shear-wave velocities of the upper and lower crust are estimated to be 3.64 and 3.95 kilometers per second using Rayleigh waves and 3.53 and 4.16 kilometers per second using Love waves, which are in good agreement with the results of other geophysical surveys in this area. The modest magnitude of the low-velocity anomalies within the crust and their locations extending well beyond the limits of Harrat Rahat indicate that they are not caused by a crustal magma chamber. If magma chambers exist, they are smaller than can be imaged with our seismological method (resolution corresponds to a 15-kilometer wavelength), deeper than 30 kilometers, or shallower than 5 kilometers with a small velocity contrast. The last possibility is discounted by weak-to-absent surface geothermal activity and by a lack of shallow seismicity that characterizes other areas with known shallow magmas, such as Hawai‘i. We then expanded our work to the entire Arabian Shield with principally the same methodology to look at large-scale regional patterns. We found modest shear-wave velocity deviations on the order of only ±3 percent, which are within expected ranges for lithological variation.

Introduction

Shear-wave (S-wave) crustal velocity models provide critical information about the composition and other physical properties of the crust (Christensen, 1996). Ambient seismic noise tomography is a highly effective means of extracting the S-wave velocity structure (Shapiro and Campillo, 2004) in regions where earthquakes are scarce (Saygin and Kennet, 2010; Overduin and others, 2015). This method is useful for the study of the crustal velocity structure of the Arabian Shield because of the paucity of local earthquakes in the interior of the Arabia Plate (Youssef, 2015), which severely limits the application of local earthquake tomography. The Saudi Arabia National Seismic network produces seismic recordings that are well suited to the application of ambient noise tomography. In this study, we focus on the northern Harrat Rahat volcanic field, which is the site of the most recent volcanic eruption in the Kingdom of Saudi Arabia (1256 C.E.; 654 in the year of the Hijra [A.H]; fig. 1) (Camp and others, 1987; Dietterich and others, 2019, 2023). Of particular interest is the possible presence of substantial seismic shear-wave velocity reductions (that is, 10 percent or

[1]U.S. Geological Survey.

[2]Victoria University of Wellington, New Zealand.

greater reduction) that could indicate the presence of a crustal magma chamber, which has been reported at some other active magmatic systems (Flinders and others [2018] and references therein).

The velocity structure of the mantle beneath Saudi Arabia was recently determined using teleseismic earthquake data with periods from 20 to 143 seconds, whose wavelengths are too large to effectively probe the crust (Yao and others, 2017). In contrast, the ambient noise signal peaks approximately at periods between 7 and 14 seconds (Bonnefoy-Claudet and others, 2006), so it can provide details of the crust not detected by Yao and others (2017). We use ambient noise methods to determine surface-wave and shear-wave velocities for northern Harrat Rahat (latitudes >24° N.). The northern part of Harrat

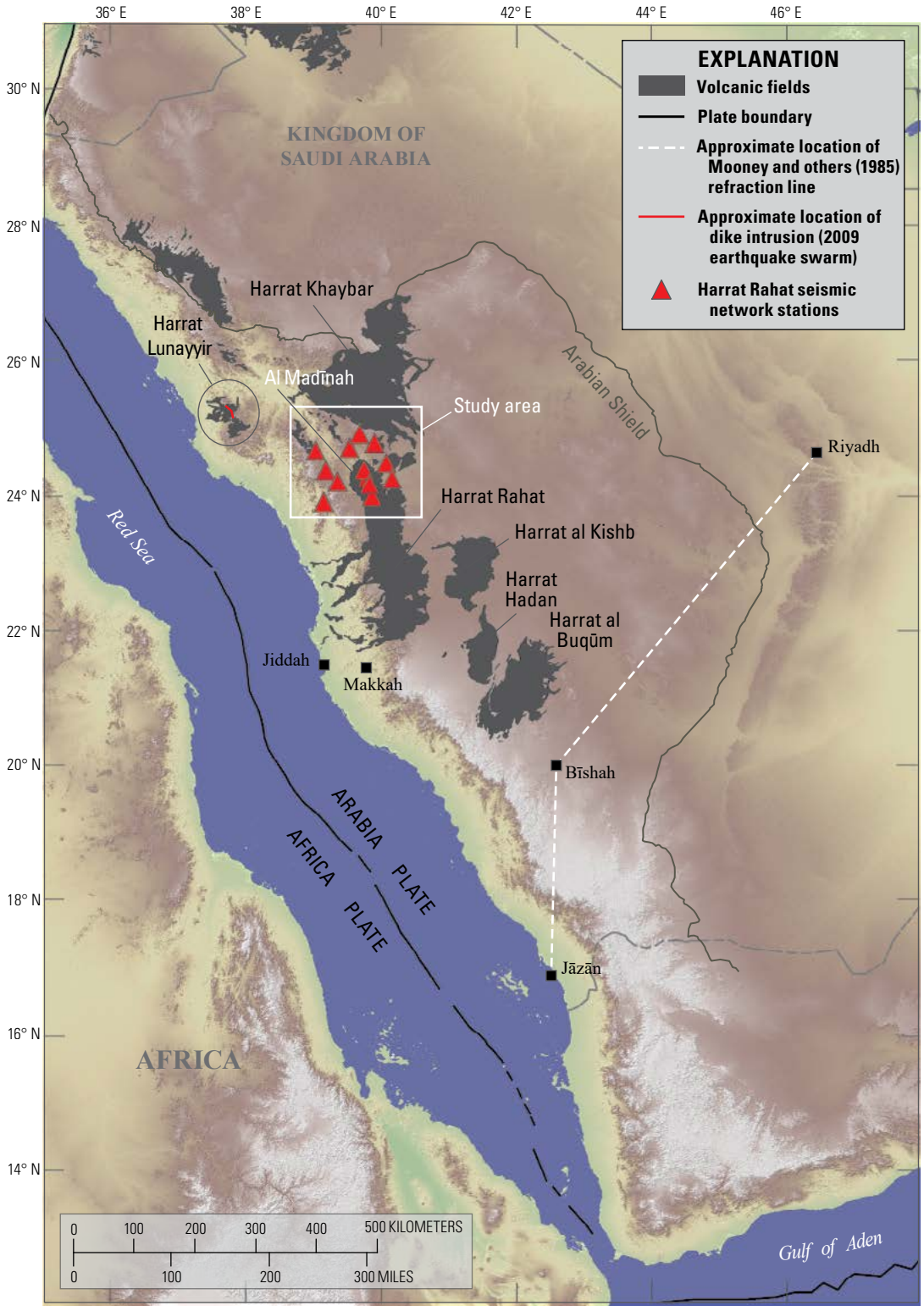

Base map from Earth Explorer GTOPO30 DEM dataset

Figure 1. Map of the Red Sea and Arabian Peninsula region showing the geologic and geographic context surrounding the study area in northern Harrat Rahat. The location of the harrats (volcanic fields) was obtained from Camp and Roobol (1992) and Pollastro and others (1999), and the location of the Harrat Lunayyir dike intrusion during the 2009 earthquake swarm is from Baer and Hamiel (2010).

Rahat, also called Harrat al Madīnah (Moufti and others, 2012a), will be referred to as northern Harrat Rahat throughout this chapter (fig. 1). This project is part of an overall effort by the U.S. Geological Survey (USGS) and the Saudi Geological Survey (SGS) to assess volcanic and seismic hazards within Saudi Arabia.

Harrat Rahat has a low level of background seismicity (generally moment magnitude [M_w] < 3) that is hypothesized to be associated with faulting owing to crustal extension and fluid movement at depth (Johnson and Kattan, 2012). Notable seismic activity in this area includes an earthquake swarm that occurred between November 11 and December 28, 1999, which consisted of 500 events that ranged in local magnitude (M_L) from 1.1 to 2.3 (fig. 2) (Mokhtar and others, 2013).

The most recent earthquake swarm in Saudi Arabia occurred at Harrat Lunayyir (fig. 1), which is located approximately 200 kilometers (km) west-northwest of Al Madīnah (fig. 2). From April 18 to May 19, 2009, more than 4,000 earthquakes as large as M_w 4 and seven events larger than M_w 4 were recorded. The swarm, which was the largest ever recorded in the region, had a peak magnitude of M_w 5.7, and was caused by the intrusion of an approximately 12-km-long and 2.5-meter (m)-thick dike within the top 10 km of the crust (Baer and Hamiel, 2010; Pallister and others, 2010). Owing to a pair of earthquake swarms (1999 and 2009), the eruption in 1256 C.E. (654 A.H.) and geological evidence for other relatively young volcanism (Camp and Roobol, 1989, 1991) in the vicinity of Al Madīnah, a place of great cultural significance, northern Harrat Rahat area has been the focus of many geological and geophysical studies. These studies can be used to test the accuracy of ambient noise tomography results that can then be expanded to the rest of the country, where supporting datasets are not available. A recent compressional wave (P-wave) tomographic study hypothesized that two magma chambers may be present in the crust below Harrat Rahat (Abdelwahed and others, 2016). Our primary objective is to use ambient noise methods to test this hypothesis and, if correct, to image this feature.

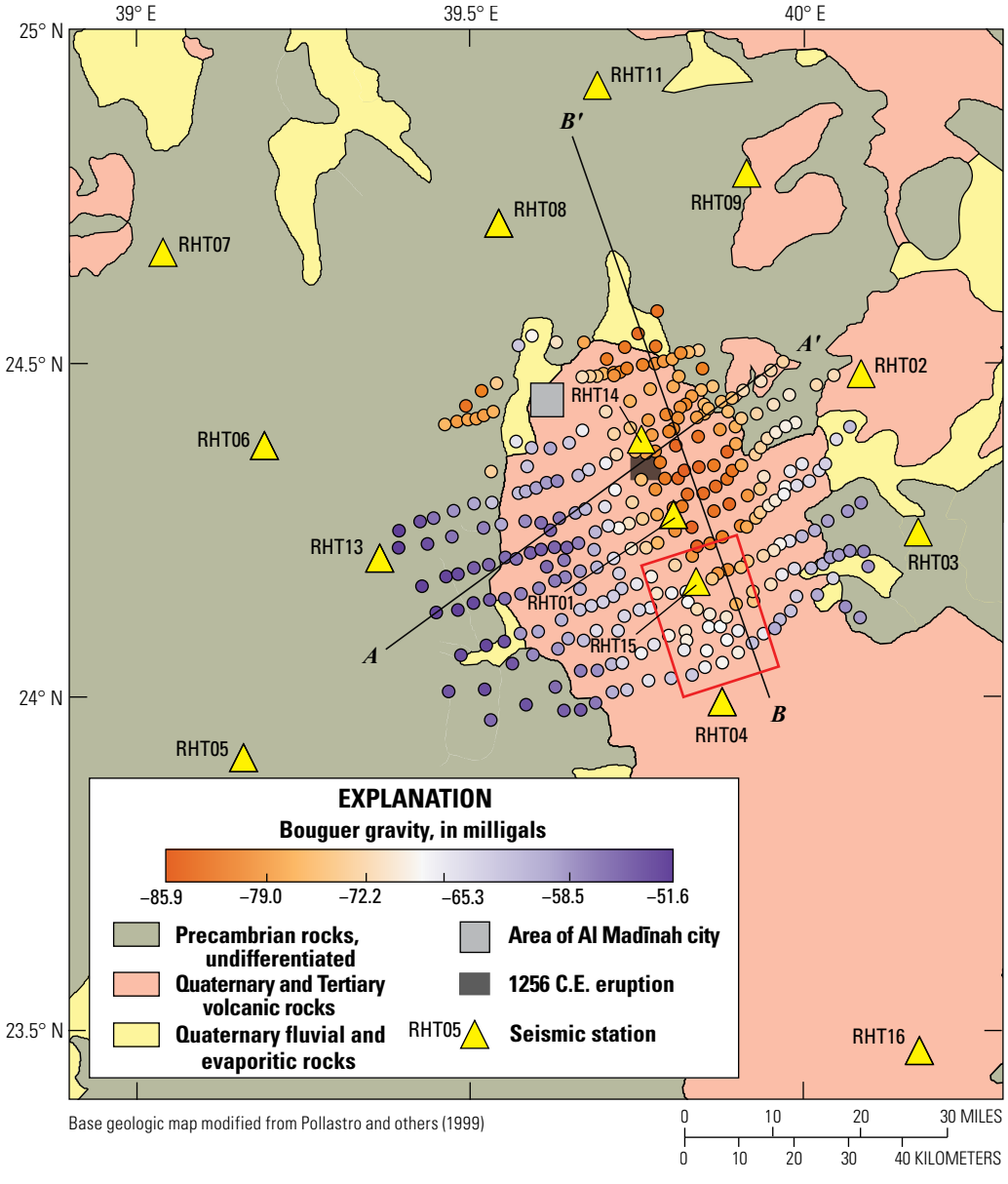

Figure 2. Map of northern Harrat Rahat study area (location in fig. 1) showing surface geology (Pollastro and others, 1999, as in Pellaton, 1981) and complete Bouguer gravity (Langenheim and others, 2019, 2023). Cross sections *A*–*A*′ and *B*–*B*′ are discussed in the "Cross Sections" section. Red box marks the epicentral location of the 1999 Harrat Rahat earthquake swarm discussed in the text.

Regional Geology and Tectonics

Harrat Rahat is located on the Arabian Shield, an approximately 725,000-square-kilometer (km^2) surface exposure of Precambrian rocks that form the crystalline basement of the Arabia Plate (fig. 1) (Johnson and Kattan, 2012). Since its separation from Africa, caused by rifting in the Red Sea and the Gulf of Aden that began about 25 million years ago, the Arabia Plate has rotated counterclockwise and moved north at a rate of approximately 2–3 centimeters per year (cm/yr) (Bird, 2002; Stern and Johnson, 2010).

In 1978, the USGS recorded a 1,000-km-long refraction profile extending from Riyadh in the northeast to the Red Sea coast at Jāzān in the southwest to determine the P-wave seismic velocity structure of the crust of the Arabian Shield (fig.1) (Mooney and others, 1985). Using two-dimensional (2D) ray-tracing techniques, Mooney and others (1985) found that the crust of the shield is primarily composed of two layers, each approximately 20 km thick, with average P-wave velocities of 6.3 and 7.0 kilometers per second (km/s) in the upper and lower halves, respectively. Mooney and others (1985) observed velocities ranging from 7.3 to 7.8 km/s at the base of the lower crust and 6.6 to 6.9 km/s in the top segment of the lower crust, which they interpret to reflect compositional differences in the lower crust: a plagioclase-rich upper portion and a pyroxene-rich lower part. The bottom part of the lower crust will not be addressed in this chapter because of insufficient depth resolution owing to the wide seismometer spacing.

The Arabian Shield comprises 445,000 km^2 (about 60 percent of its total area) of exposed Precambrian rock (Johnson and Kattan, 2012). Interior parts of the shield are locally covered by Mesozoic and Cenozoic sedimentary rocks; Cenozoic alluvium, aeolian sand, and evaporites (sabkha); and Cenozoic basaltic lava fields. The Arabic word for "volcanic lava field," such as those that are formed by Cenozoic basaltic lava, is "harrat." Harrat Rahat is a Cenozoic alkaline volcanic field that extends over an area of approximately 20,000 km^2 and is bordered by the cities of Jiddah and Makkah in the south and Al Madīnah to the north (Coleman and others, 1983; Camp and Roobol, 1989, 1991; Moufti and others, 2011, 2012a, b; Moufti and Nèmeth, 2016). The field consists dominantly of alkalic basalt and hawaiite (about 90 percent) accompanied by mugearite, benmoreite, and trachyte in sub-equal amounts (Camp and Roobol, 1989, 1991; Downs and others, 2019). Cenozoic volcanic rocks of Harrat Rahat average about 100 m thick (Blank and Sadek, 1983; Camp and Roobol, 1989, 1991) but are locally as thick as 600 m where they conceal an apparent depression in the Precambrian basement surface, possibly a graben (Langenheim and others, 2019, 2023).

Summarizing after Camp and Roobol (1989, 1991), Harrat Rahat consists of four regions of focused volcanism, or sub-harrats, aligned south-southeast to north-northwest that coalesced as they grew into a single, 300-km-long volcanic field. Each of the sub-harrats, including northern Harrat Rahat, contains a narrow but elongate belt of abundant volcanic vents consisting of scoria cones, lava domes, craters, and fissures that are also aligned in a generally south-southeast to north-northwest direction. Frequent eruptions along these alignments of abundant vents built up ridges of constructional volcanic relief which form the crests of the sub-harrats, with lava flows mainly extending west or east from the vent axes. These belts of closely spaced vents of the sub-harrats range from about 40 to 60 km in length, becoming indistinct and lower elevation at their north and south ends, and in their highest portions standing about 250 to 450 m above valleys that flank the harrat to the east and west where Precambrian basement is exposed. The subordinate evolved magmas, consisting of mugearites, benmoreites, and trachytes, mainly erupted from these raised vent axes that were the sites of most abundant and protracted volcanism. The most recent volcanic eruption in this area was the 1256 C.E. eruption (654 A.H.; black box on fig. 2), a 2.25-km-long fissure eruption that produced a 23-km-long lava flow that stopped 8 km east of Al Madīnah's center (Camp and others, 1987; Dietterich and others, 2019, 2023). The hypocenters for the 1999 Harrat Rahat earthquake swarm were recently relocated and found to be south-southeast of the 1256 C.E. eruption site at depths between 20 to 40 kilometers (fig. 2) (Mokhtar and others, 2013).

There are several hypotheses for the origin of recent Arabian Shield volcanism. Camp and Roobol (1992) suggested that volcanism was due to a local mantle plume beneath the Arabian Shield. However, the absence of unidirectional volcanic migration and the north-northwest-trending distribution of volcanic vents parallel to the Red Sea suggests alternatively that volcanism in this region is related to crustal extension along the reactivated Red Sea Fault System (Moufti and others, 2012a). Chang and others (2011) suggested that the volcanism may instead be due to lateral flow from the Afar or Jordan plumes. Tang and others (2016), using teleseismic P-wave receiver functions and fundamental Rayleigh-wave group velocities, inferred high mantle lid temperatures and slow velocities on the north and south tips of the Arabian Shield. They attributed these features to thermal conduction from the Afar and Jordan plumes and hypothesized that the volcanism in the Arabian Shield is caused by small-scale adiabatic ascent of magma diapirs. This hypothesis was supported by observation of a low-velocity zone in the upper mantle beneath western Saudi Arabia determined using teleseismic Rayleigh-wave phase velocities (Yao and others, 2017). A study by Tang and others (2018) found local zones of low shear-wave velocity at depths of 15–35 km underneath the harrats using Rayleigh-wave group velocities from regional earthquakes, which indicate the presence of partial melt.

On the basis of geochemistry (Sisson and others, 2023) and radiogenic isotopes (Salters and others, 2023), the mantle source for northern Harrat Rahat's magmas appears similar in most respects to the long-term geochemically depleted asthenospheric sources of midocean ridge basalts, but with possibly about 30 percent addition of material like that postulated for the Afar mantle plume, with the alkalic character of the harrat basalts resulting from low degrees of partial melting at depths straddling the garnet- and spinel-peridotite stability fields. Late Cenozoic harrats to the south into Yemen seem to derive from sources with greater proportions of Afar plume material (Salters and others, 2023), consistent with greater proximity to the plume's center beneath

the southernmost Red Sea and Afar depression. If correct, a simple and exclusive plume source for harrat volcanism is ruled out, although a nearby major plume might promote circulation in the ambient asthenosphere, leading it to partially melt, as well as mixing with it.

Prior Geophysical Studies

Several geophysical analyses have been done in Harrat Rahat, which include P-wave arrival time tomography (Abdelwahed and others, 2016), receiver function studies (Tang and others, 2016, 2018), a gravity survey (Langenheim and others, 2019, 2023), and a resistivity survey (Bedrosian and others, 2019; Peacock and others, 2023). The subsurface was imaged at Harrat Rahat by Abdelwahed and others (2016) using local and teleseismic earthquakes recorded at a borehole array near seismic stations RHT14 and RHT01 (fig. 2). They found several high and low P-wave velocity anomalies (±5–8 percent) below Harrat Rahat, which were interpreted to be the result of basaltic and trachytic intrusions (Abdelwahed and others, 2016). A joint inversion of P-wave receiver functions and Rayleigh-wave group-velocity data by Tang and others (2016) resolved a shear-wave velocity structure for Harrat Rahat to depths of 60 km. They estimated a crustal thickness of approximately 36 km and inferred a 10 km low-velocity layer (approximately −13 percent) to be overlaying a high-velocity layer (6 precent) in the upper crust at the southwest edge of the Harrat Rahat seismic network.

The USGS and SGS collected 299 gravity measurements at Harrat Rahat in November 2014 (Langenheim and others, 2019, 2023). Figure 2 displays the Bouguer gravity anomalies overlain on the general surface geology of Harrat Rahat. The anomalies form a high-low-high pattern from west to east, and the lowest values occur southeast of the vent for the historical 1256 C.E. eruption (fig. 2). The gravity low is interpreted to be caused by the combined effects of a depression of the basement surface and by less-dense basement rocks beneath the vent axis that continue beyond the northern limit of volcanic cover (Langenheim and others, 2019, 2023).

In early 2016, a magnetotelluric survey was conducted in Harrat Rahat by the USGS and SGS to determine the resistivity structure of the lithosphere, which included possible evidence for melt zones (Bedrosian and others, 2019; Peacock and others, 2023). A total of 119 sites were deployed across a grid with a 2 km cell size, and data from these sites were analyzed to resolve resistivity from depths of 200 meters to 70 km. Conventional three-dimensional (3D) processing of the resistivity survey yielded several apparent regional conductivity anomalies in the middle and lower crust. Because of their large sizes, strengths, and orientation unlike Precambrian structures, as well as their extension far beyond the limits of the volcanic field, these anomalies were suggested to be processing artifacts resulting from strong electrical anisotropy owing to interconnected grain-boundary graphite in the Precambrian crust (Bedrosian and others, 2019; Peacock and others, 2023). The resistivity anomalies were absent on 2D cross sections that are less susceptible to anisotropy artifacts, and Bedrosian and others (2019) and Peacock and others (2023) found no evidence supporting the presence of crustal magma reservoirs detectable at the resolution of the survey.

Methods

The Harrat Rahat Seismic Array is a subset of the 200-station (as of 2019) Saudi Arabia National Broadband Seismic Network. It contains 14 Nanometrics Trillium T120 instruments (Townsend, 2014) with an array aperture of approximately 130 kilometers (fig. 2). The T120 instruments are broadband seismometers with a frequency response range of approximately 0.01–20 hertz (Hz) (Townsend, 2014). We used ambient noise recordings to compute one dimensional (1D) shear-wave velocities and interpolated the results to produce a pseudo 3D velocity model of the region. The maximum resolution depth of the model is approximately 30 km and includes all of the upper crust and part of the lower crust. The data used for this experiment were recorded between January and December 2014 (seismic data used may be requested from the Saudi Geological Survey, Jeddah, Saudi Arabia).

We processed the data using the following steps: (1) calculation of cross-correlations; (2) determination of dispersion curves through Frequency-Time Analysis (FTAN) (Levshin and others, 1972, 1989); (3) computation of surface-wave dispersion maps (Barmin and others, 2001); and (4) computation of surface-waves to shear-wave velocity using the neighborhood algorithm (Sambridge, 1999). Appendix 1 of this report and Civilini (2018) provide a full description of the processing parameters.

Cross Correlations

We computed daily cross correlations for each station pair in the Harrat Rahat seismic network using the software MSNoise (Lecocq and others, 2014) and the workflow suggested by Bensen and others (2007). All the available data were used, because increasing the number of stacked cross-correlated segments improves the signal-to-noise ratio of the result (Bensen and others, 2007). Each trace was filtered to 0.005–1.1 Hz, spectrally whitened (amplitude of the frequency spectrum is the same across all frequencies), and one-bit normalized prior to computing cross correlations. We computed cross correlations for the diagonal components of the Green's function matrix: radial-radial (RR), transverse-transverse (TT), and vertical-vertical (ZZ). In this terminology, the hyphen isolates the component assessed at each station. For example, radial-radial means that the radial component at station 1 was cross correlated with the radial component at station 2.

Dispersive surface waves were not observed in any of the cross-component correlations (for example, radial-transverse) and were excluded from our analysis (Civilini, 2018) because the cross-components of the Green's function tensor represent a combination of Rayleigh and Love waves that cannot be used to extract a consistent dispersion curve. We differentiated the seismogram into signal and noise parts corresponding to positive and negative lag times (temporal output of the cross-correlation function) faster and slower than 2 km/s, respectively. The

signal-to-noise ratio was calculated by dividing the peak value in the signal portion of the seismogram by the root-mean-squared error of the noise. We discarded any cross-correlation stack that had a signal-to-noise ratio less than 10. Some redundancy is present in the inclusion of results for radial-radial (RR) and vertical-vertical (ZZ) since both record Rayleigh waves.

Computing Dispersion Curves

Dispersion of surface waves is commonly characterized as a function of velocity or slowness in the frequency domain. FTAN (Levshin and others, 1972, 1989) is a method for extracting dispersion curves from time-series data. The FTAN methodology computes group-velocity dispersion curves via a sliding Gaussian filter throughout the frequency domain of the cross correlation. In this study, the positive and negative sides of the cross correlation were stacked to increase the signal-to-noise ratio prior to FTAN computation. Phase velocity was calculated by using the envelope function of the group velocity and the phase of the analytical signal (Snieder, 2004; Bensen and others, 2007).

Automatic frequency-time analysis (AFTAN) is a set of Fortran subroutines and C functions implementing an automatic FTAN for the inversion of dispersion curves (Ritzwoller, 2013). Figure 2.1 of appendix 2 shows the group and phase velocities obtained using the AFTAN procedure for station pair RHT03 and RHT06.

Sensitivity Kernels

We used the Senskernel software package of Levshin (2013), which is based on the work of Levshin and others (1989), to determine group and phase velocity sensitivity kernels. The velocities from the northeast segment of shot point 4 of the Mooney and others (1985) seismic refraction line, located at lat 20.09° N., long 42.65° E., were used as input models for the sensitivity kernel calculation (fig. 3). This particular shot point was chosen because it lies near Harrat al

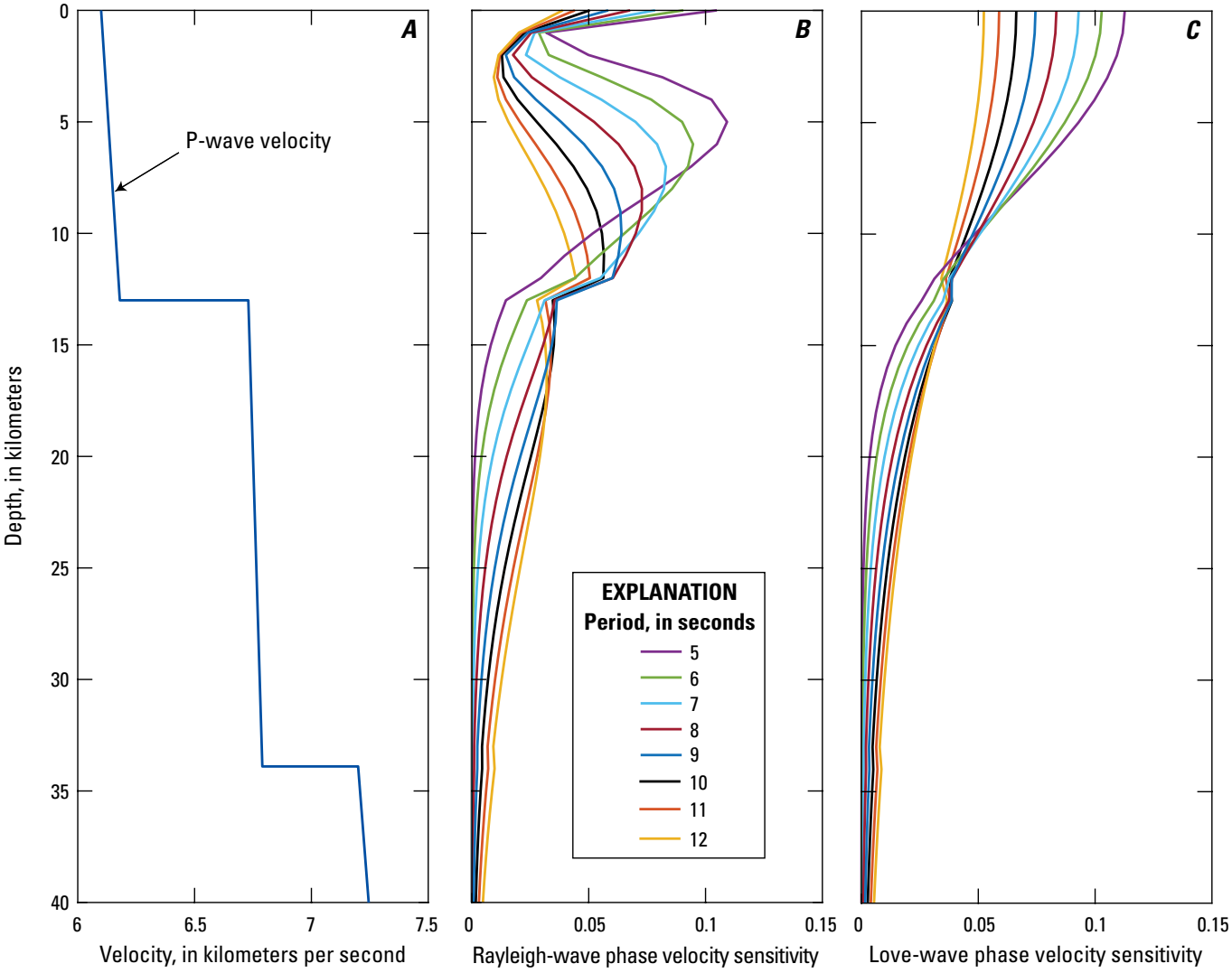

Figure 3. Graphs showing the P-wave velocity model of the northeast segment of shot point 4 modified from Mooney and others (1985, their fig. 4a) (*A*), Rayleigh-wave phase velocity (*B*), and Love-wave phase velocity, (*C*) sensitivity kernels.

Buqūm, which is a location expected to have similar crustal velocities to our study area.

The Senskernel codes also require input S-wave velocity and density models. We calculated S-wave velocities from the P-wave to S-wave velocity (V_P/V_S) ratios determined by Christensen (1996) and density from the empirical relationships of Christensen and Mooney (1995). Figure 3 shows the phase-velocity sensitivity kernels alongside the Mooney and others (1985, their fig. 4a) input model. The sensitivity kernels for group velocities are displayed in figure 2.2 of appendix 2.

The maximum depth resolution of all kernels is approximately 30 km, and the greatest resolution typically occurs within the top 20 km for periods of 5–12 seconds (fig. 3). Assuming that this velocity model is representative of the velocities beneath Harrat Rahat, surface waves (Rayleigh and Love) can image the top two crustal layers but will not resolve structures in the upper mantle (fig. 3).

Surface-Wave Inversion

We used the nearly linear tomographic codes of Barmin and others (2001) to estimate 2D surface-wave velocity maps from the dispersion curves. The dispersion curves are inverted using spherical geometry, local basis functions (nodes), and data-density-dependent regularization (Barmin and others, 2001).

The main user-chosen inputs to the tomographic inversion are the width of the Gaussian smoothing filter (σ in km) and the degree of amplitude smoothing (α), which are primarily dependent on the node spacing and interstation distance. The approximation outlined by Barmin and others (2001) was used, whereby $\sigma = 2l$, in which l is the separation distance between the nodes within the analysis grid, and $\alpha = 4\sigma$. Although the Harrat Rahat inversion was done with a node spacing of 0.1° (about 11 km at the Equator), we increased the smoothing to values of $\sigma = 60$ km and $\alpha = 240$ to prevent the low number of paths from causing errors in the inversion.

Surface-wave tomography that uses ambient noise requires that the seismic station spacing be large enough to allow the full wavelength of the measured signal to be coherent from one station to the next. Although some argue that the separation distance needs to be at least three times the wavelength of the signal (Bensen and others, 2007; Tsai, 2010), other studies have concluded that 1–2 wavelengths are sufficient (Shapiro and others, 2005; Brenguier and others, 2007). A minimum interstation distance of one wavelength was chosen to ensure that the surface waves completed a full cycle while also maximizing the number of interstation paths.

In addition to producing dispersion maps, the Barmin and others (2001) code automatically conducts a cone-resolution analysis, which determines the minimum distance at which velocity anomalies can be resolved. Areas that have a resolution cone-radius greater than 50 km were removed from our tomographic results. The number of paths used for each tomographic map was kept constant throughout each period. For example, if a path was unused for the 12-second period map owing to the one-wavelength condition criteria, that path was also removed for 1–11-second periods. The number of paths was kept constant to limit the variation caused at nodes of different paths, which was significant owing to the small period range sampled by this study.

Shear-Wave Velocity Inversion

Dispersion maps show velocity as a function of period and can be thought of as a depth-averaged horizontal cross section. Owing to this averaging, features with low velocity differences compared to the surrounding rocks and smaller dimensions than the wavelength may be obscured. Shear-wave velocity inversions are made using dispersion curves at each node of the dispersion maps. We used the Dinver software package (Wathelet and others, 2004; Wathelet, 2008) to invert the RR and TT dispersion curves at each latitude and longitude node into 1D S-wave velocity models. These new dispersion curves are hereafter called node dispersion curves for clarity. The ZZ nodal dispersion curves were not inverted to S-wave velocity owing to the fewer number of paths compared to the RR and TT components, as discussed in the "Dispersion Maps" section. The cross-correlated components of the empirical Green's function tensor (that is, radial-transverse, radial-vertical) did not display surface-wave moveouts and were not included in the inversion (Civilini, 2018).

Dinver incorporates the neighborhood algorithm of Sambridge (1999), which preferentially samples areas near values of good time (t) instead of using the random distribution of Monte Carlo methods. Each inversion yields models that are based on minimizing the misfit value for each model, which is defined as the percentage difference from the measured node dispersion curve. The number of layers in the parametrization should be as few as possible to prevent overfitting (Wathelet, 2005). Using a minimum number of layers is especially important for this study, which only uses dispersion curves from 5- to 12-second period (only 8 points). Owing to this limited sampling resolution, 2-layer to 5-layer inversion models were computed (table 1.3 of appendix 1). The 4-layer and 5-layer velocity models allow for velocity reversals.

The densities of the upper and lower crust in the region were obtained from the literature (Al-Saad and others, 1992; Brew and others, 2001; Stern and Johnson, 2010), and a half space for each model was imposed to be the inferred plagioclase-rich upper portion of the lower crust (Stern and Johnson, 2010). This constraint was due to the limited resolution of the surface waves at depths greater than 30 km (fig. 3). We computed a weighted mean of the inversion models using a misfit threshold of 10 percent deviation from the measured node dispersion curve. This enabled us to quantify the likelihood of a solution representing the true velocity structure. The weighted mean from each node was interpolated into a pseudo 3D model, which was used to derive cross sections through Harrat Rahat.

Results

Cross-Correlation Moveouts

Cross-correlation moveouts of northern Harrat Rahat station pairs were computed and stacked across the entire time period (1 year) using the algorithm described in the "Cross Correlations" section (fig. 4). A first-order approximation of the group velocity was determined by measuring the lag time across cross correlations arranged by distance between seismic station pairs. We found that RR, TT, and ZZ cross-correlated components have group velocities of 3.0, 3.4, and 3.1 km/s respectively (fig. 4). The higher velocity (fig. 4*B*) confirms that the TT component corresponds to a Love wave, whereas the RR and ZZ components reflect the horizontal and vertical components of a Rayleigh wave. Asymmetry can be observed in some of the cross-correlation pairs owing to azimuthal heterogeneity in the strength of the ambient seismic noise signal (fig. 4). For example, the top three cross correlations with greatest station-interstation distance in the TT component (fig. 4*B*) all have higher amplitudes in the acausal portion of the cross correlation (negative lag times). This asymmetry is due to less energy from the north and northeast (landlocked directions) than from other azimuths.

Ambient noise Rayleigh-wave cross-correlation results are sometimes affected by zero-point noise or near zero-time signal (Landés and others, 2010), which is typically caused by teleseismic body waves generated by distant storms in deep oceans (Gerstoft and others, 2008; Landés and others, 2010; Nishida and Takagi, 2016) or Mohorovičić discontinuity reflections (Zhan and others, 2010; Poli and others, 2012). These natural phenomena produce large amplitudes near the zero lag time in the cross correlation, which sometime result in anomalously fast velocities in parts of dispersion curves. After computing daily cross correlations for the seismic station pairs, we observed that some cross correlations of the ZZ component were affected by zero-point noise. We observed zero-point noise with varying amplitudes in most Rayleigh-wave cross correlations of the ZZ component. Typically, cross correlations with large zero-point noise had low signal-to-noise ratios and were removed by the minimum signal-to-noise ratio threshold of 10. The AFTAN procedure for the remaining traces did not seem to be affected by zero-point noise within the frequency bounds of interest. The total numbers of paths used were 55 (RR), 44 (TT), and 40 (ZZ) for group velocities, and 60 (RR), 56 (TT), and 38 (ZZ) for phase velocities.

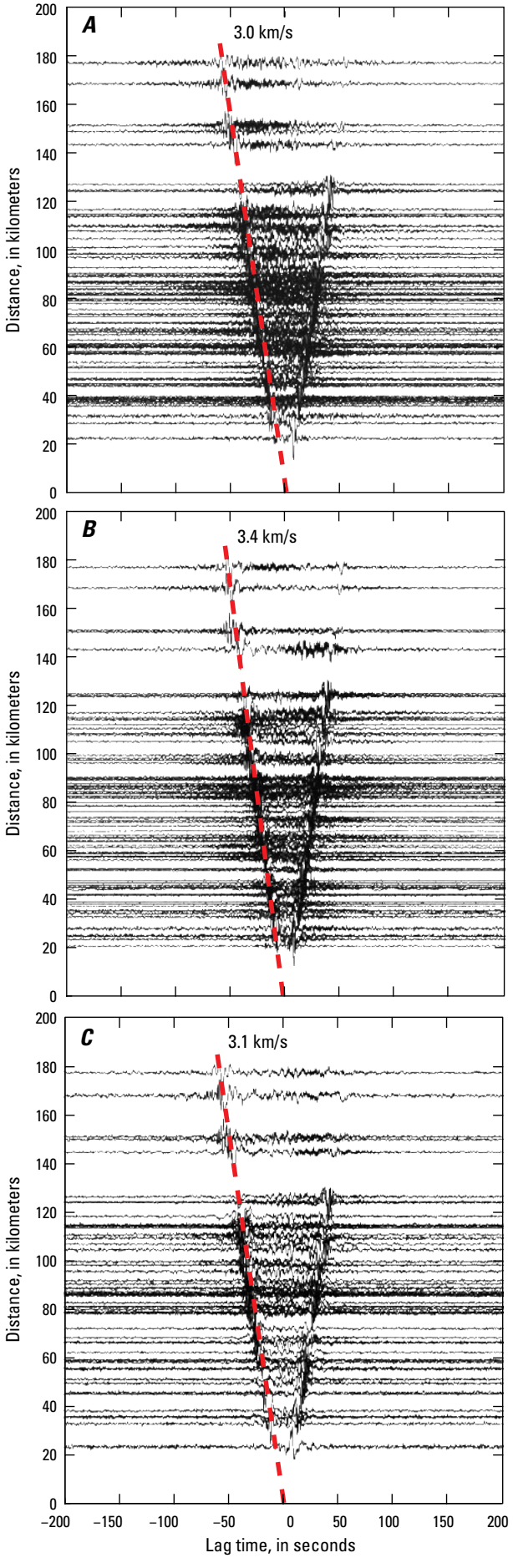

Figure 4. Cross-correlation moveouts for Harrat Rahat seismic station pairs for radial-radial (RR) (*A*), transverse-transverse (TT) (*B*), and vertical-vertical (ZZ) (*C*) components. The red dashed line represents a moveout of the labeled velocity (in kilometers per second [km/s]) for phase velocities. Lag-time corresponds to the temporal output (in seconds) of the cross-correlation function, and distance refers to the interstation distance between cross-correlation station pairs.

Checkerboard Tests

Standard checkerboard tests (fig. 5*A*) were done to assess the resolution of the tomographic inversion. Interstation velocities were calculated through a synthetic model composed of a checkerboard of low and high velocities. The velocity values for these station pairs were inverted using the method described in the "Surface-Wave Inversion" section. The resulting dispersion map was then compared to the original synthetic model. We used checkerboards that consisted of 0.5° alternating blocks of 3.5 and 4.0 km/s (fig. 5*A*). Synthetic velocities for phase-velocity paths through the checkerboard were computed using the computer program Fatiando, which is an open-source Python library for geophysical inversions (Uieda and others, 2013). The synthetic velocities were inverted using the Barmin and others (2001) code rather than Fatiando to maintain consistency with our other results. Although each checkerboard test suffers from smearing at the edges of the array, the boundaries and velocities are well resolved in the center of the field (fig. 5*B–D*). We found that the predicted surface-wave velocity is typically slower than in the input model. These slower velocities are due to the Fatiando software calculations instead of the Barmin and others (2001) inversion as observed in station pairs that were exclusively within high-velocity segments, such as those between stations RHT08, RHT09, and RHT11. A checkerboard model using the paths of the group velocities is displayed in figure 2.3 of appendix 2 and shows approximately the same features as figure 5.

Dispersion Maps

Using the AFTAN procedure and the inversion methods of Barmin and others (2001) discussed in the "Computing Dispersion Curves" and "Surface-Wave Inversion" sections, respectively, we obtained dispersion maps of Harrat Rahat for phase and group velocities (figs. 6, 7, and figs. 2.4–2.7 of appendix 2). Velocity changes of as much as ±3 percent from the mean are observed in the phase-velocity surface-wave maps.

The ZZ cross-correlated component had fewer paths than the other two components (38 paths compared to 60 and 56 paths) (fig. 2.4 of appendix 2). The mean phase velocities were 3.21–3.38 km/s for Rayleigh waves and 3.54–3.74 km/s for Love waves, which indicates the measured 3 percent change is approximately ±0.1 km/s. We observed low velocities at all periods for which the paths were not confined to northern Harrat Rahat. However, the lowest calculated velocities (approximately −3 percent) were near the 1256 C.E. eruption location at 5- and 7-second periods for Rayleigh waves (figs. 6*A, B*) and at a 5-second period for Love waves (fig. 7A). The group velocities show primarily the same features as the phase velocities but vary as much as ±4 percent of the mean velocity values (figs. 2.5–2.7 of appendix 2).

We observed differences between the Rayleigh- and Love-wave phase-velocity dispersion maps. A north-south trending low-velocity feature, visible in Love waves (fig. 7 and fig. 2.6 of appendix 2) but not in Rayleigh waves (fig. 6 and figs. 2.4, 2.5, 2.7 of appendix 2), extends from station RHT11 to RHT15 (fig. 2). The velocities are slowest through the feature in the 5 second period band but are observed at all periods (fig. 7). The feature that is responsible for the low velocities may be located within the shallowest 5 km indicated by the difference in depth sensitivity between the Rayleigh- and Love-wave phase velocities (fig. 3). This low-velocity feature coincides with the low-gravity anomaly of figure 2 that is interpreted to be the combined product of a basement low beneath that part of the volcanic cover rocks and to low-density sedimentary rocks of the Proterozoic Furayh Group that crop out at the north edge of the volcanic cover as well as in patches farther north (Pellaton, 1981; Langenheim and others, 2019, 2023).

One Dimensional Shear-Velocity Inversions

1D S-wave velocity inversions were computed from node dispersion curves for RR and TT cross-correlation components using the Dinver software package (Sambridge, 1999; Wathelet, 2005, 2008). The ZZ node dispersion curves were not inverted owing to inaccuracies caused by a paucity of usable paths. The dispersion curves at each node for the group velocities oscillate between values of low and high velocity, which is a behavior that is thought to be due to a strong anisotropic source off the interstation path (Tsai, 2009; Behr, 2010). The oscillations of the group velocity make it impossible to obtain reliable velocity models through inversion. Because of this, only phase velocities were used for our velocity inversions.

Two- to five-layer velocity inversions (L2, L3, L4, and L5 inversion models shown in table 1.3 of appendix 1) were computed for the RR and TT phase velocities. Figure 8 shows the RR node dispersion curve and weighted mean models for lat 24.4° N., long 39.4° E., located approximately in the center of the array in a zone of maximum station-path azimuthal coverage.

Each inversion for this node produced an increase in velocity between 15 and 25 km depth, which corresponds to the transition between the upper and lower crust (table 1.3 of appendix 1). Although 15–25 km was set as the depth of the lower-crustal half space, this velocity increase at 15–25 km depth is not likely to be an artifact of the inversion owing to the wide velocity bounds of the parameter space (2–5 km/s). Two- and three-layer inversion models (L2 and L3, respectively) delineate sharp boundaries (despite being S-wave-weighted averages produced from surface waves) and are much slower than average crustal models (Mokhtar and others, 2001; Park and others, 2008; Tang and others, 2016), which indicates that these models lack a sufficient number of

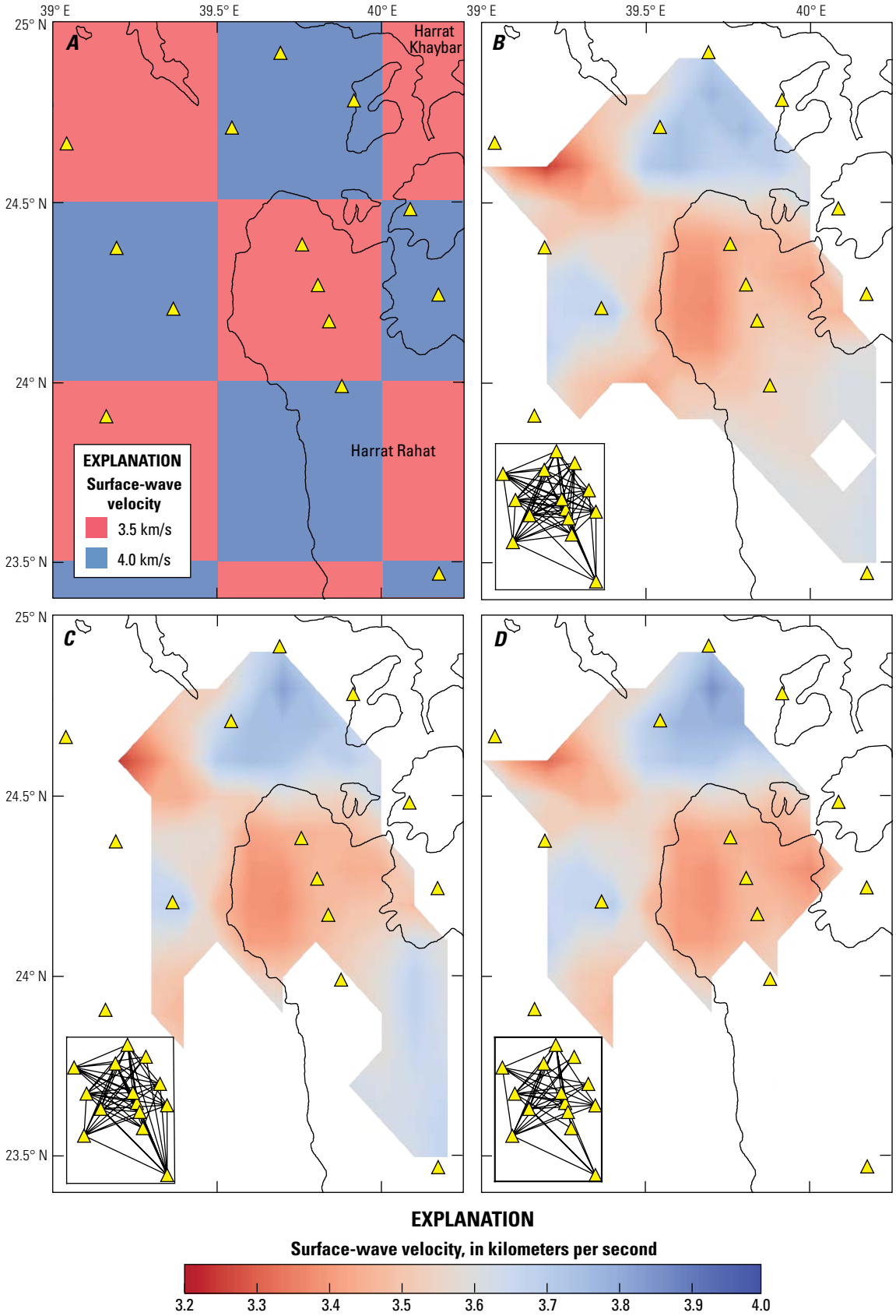

Figure 5. Maps of northern Harrat Rahat area showing the checkerboard model (*A*) and surface-wave velocities, in kilometers per second (km/s), for 0.5° cells for radial-radial (60 paths) (*B*), transverse-transverse (56 paths) (*C*), and vertical-vertical (38 paths) (*D*) phase velocity paths. Seismic stations are marked as yellow triangles, and the outline of the harrats are displayed as black lines. Station paths for parts *B*, *C*, and *D* are displayed in insets on each respective panel.

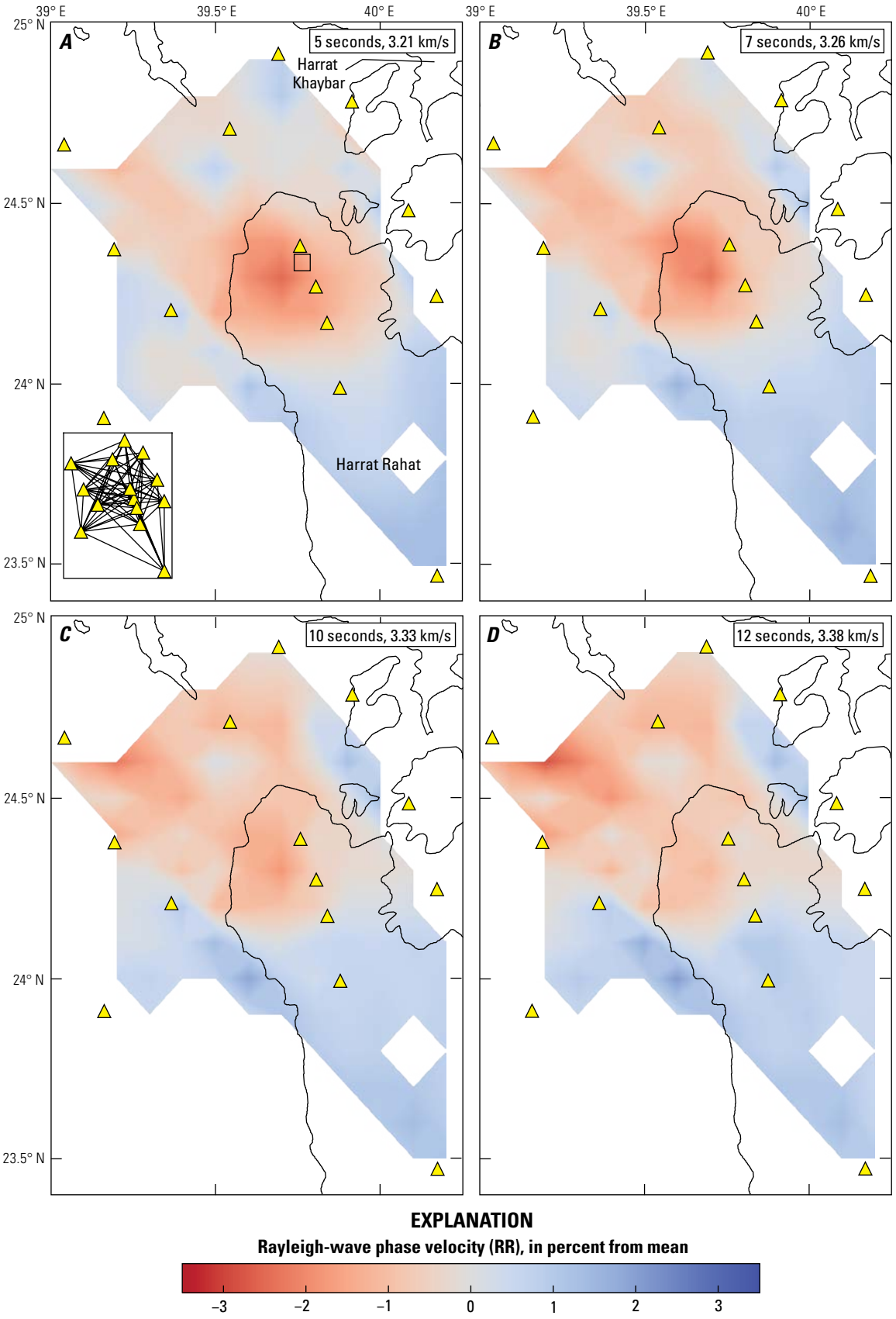

Figure 6. Maps of the northern Harrat Rahat area showing the Rayleigh-wave phase velocity as a percentage difference from the mean velocity using radial-radial (RR) cross correlations (60 paths) for 5-second (*A*), 7-second (*B*), 10-second (*C*), and 12-second (*D*) periods. Seismic stations are marked as yellow triangles, and the outlines of the harrats are displayed as black lines. The location of the 1256 C.E. eruption is displayed as a black box in part *A*. The length of and mean velocity, in kilometers per second (km/s), for each period are displayed in an inset for each panel, and the station paths are displayed in an inset on the lower left corner of part *A*.

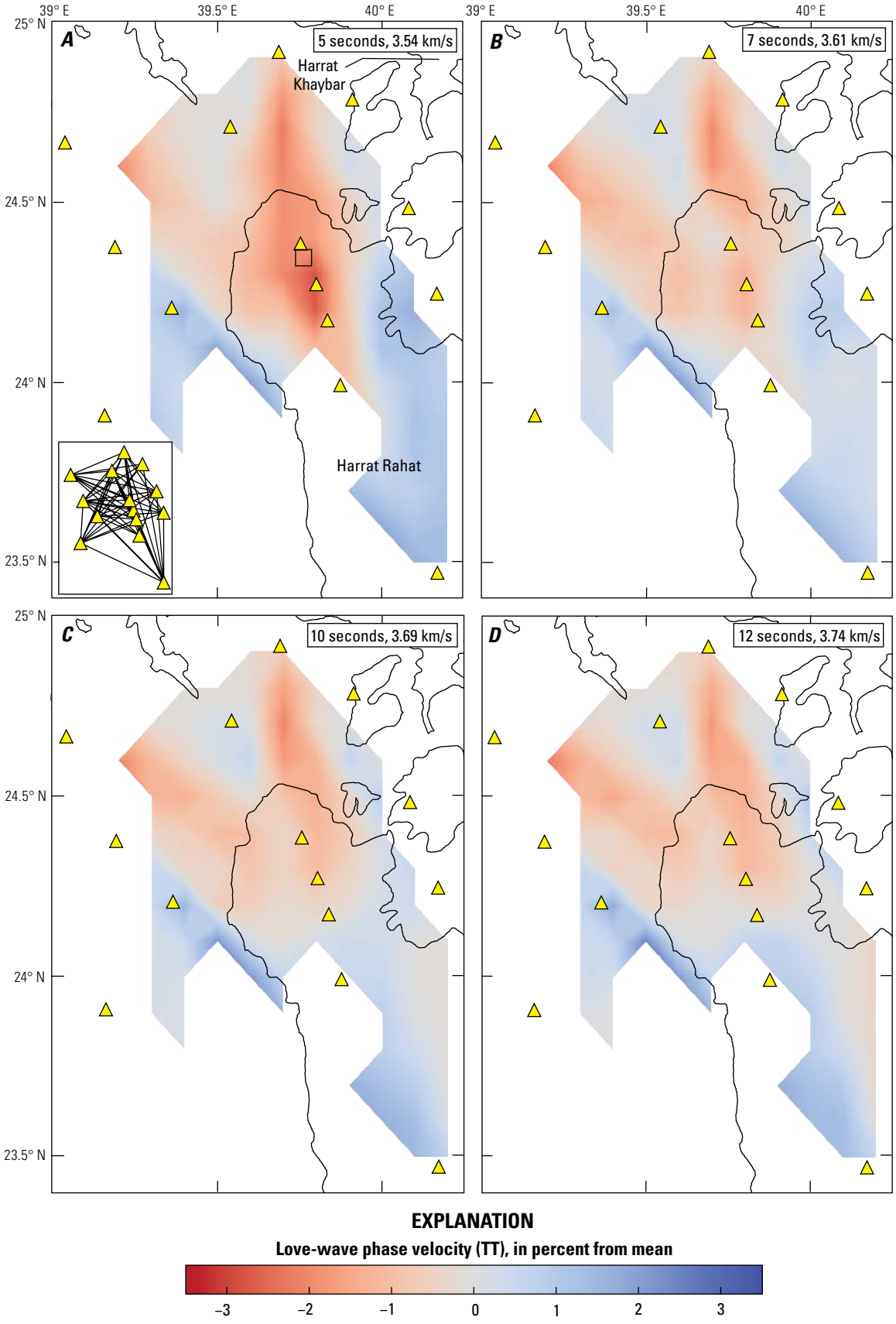

Figure 7. Maps of the northern Harrat Rahat area showing Love-wave phase velocity as a percentage difference from the mean using transverse-transverse (TT) cross correlations (56 paths) for 5-second (*A*), 7-second (*B*), 10-second (*C*), and 12-second (*D*) periods. The duration of one cycle and mean velocity, in kilometers per second (km/s), for each period are displayed in an inset for each panel, and the station paths are displayed in an inset on the lower left corner of part *A*.

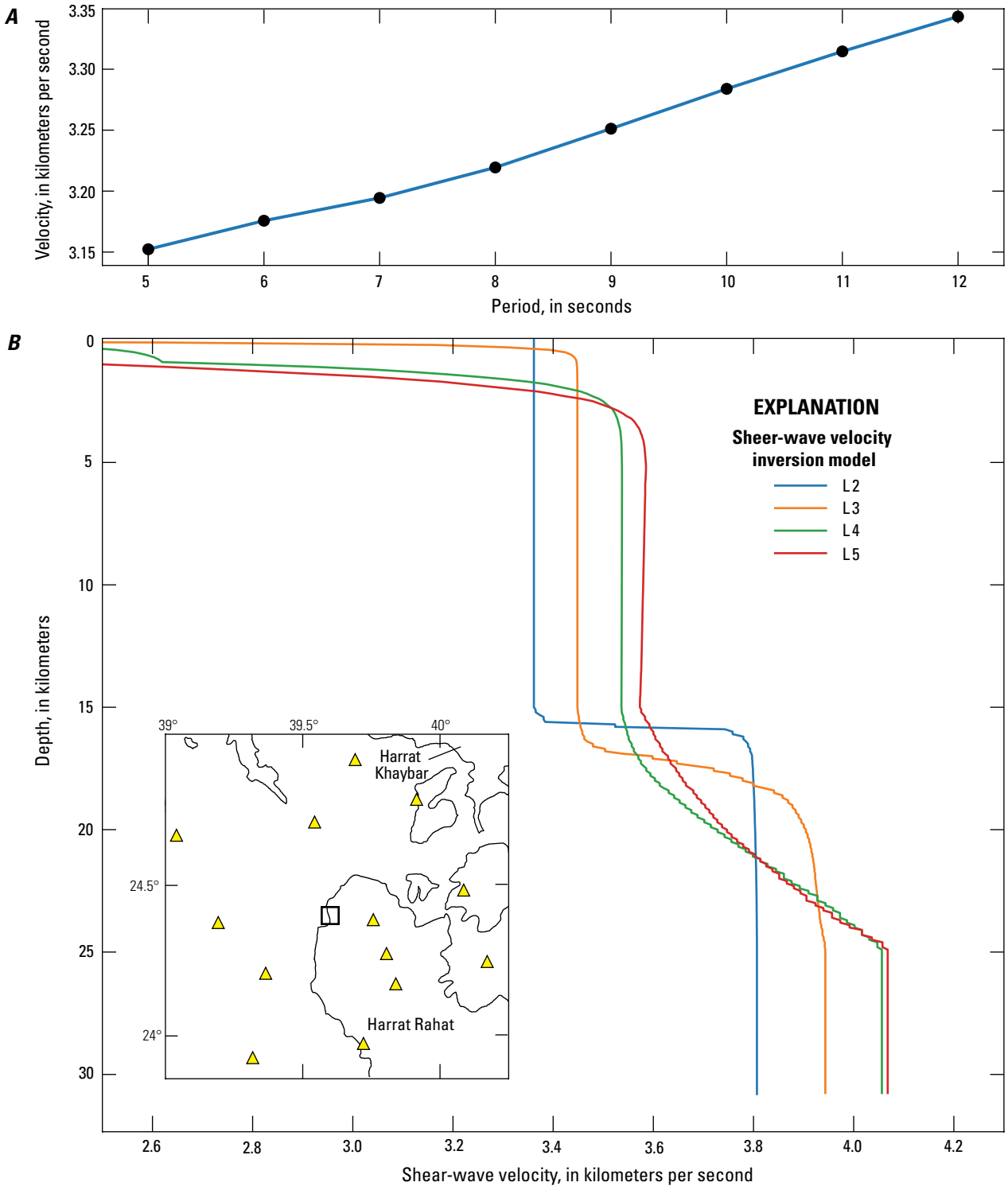

Figure 8. Line graphs showing the surface-wave dispersion curve for the radial-radial component node at lat 24.4° N., long 39.4° E. (*A*), and the 2-layer (L2), 3-layer (L3), 4-layer (L4), and 5-layer (L5) weighted mean shear-wave velocity inversion models for the dispersion curve in part *A (B)*. The inset map displays the location of the node (black square) within the Harrat Rahat seismometer network (seismic stations indicated by yellow triangles).

layers for a stable inversion. Four- and five-layer inversion models (L4 and L5, respectively) produced similar results, but the L4 inversion was chosen to minimize the number of free parameters (Wathelet and others, 2004). The L4 inversion model revealed two main crustal layers that had shear-wave velocities of 3.55 and 4.06 km/s, which are similar to the 3.69 and 4.1 km/s values obtained by Mokhtar and others (2001) through inversion of group velocities. A plot showing the ensemble of models which produced the L4 weighted mean for this point is displayed in figure 2.8 of appendix 2.

Similar to the phase-velocity used to produce the dispersion maps in figure 6, the weighted means obtained by the 1D inversions can be analyzed as a function of depth through interpolation of the 1D models. The resolution of the cells is 0.1° × 0.1°, the same as in the dispersion maps. Figures 9 and 10 display the S-wave velocity inversions for 5, 15, 20, and 25 km using Rayleigh (RR) and Love (TT) waves. We found that the weighted mean at depths from 5 to 15 km was consistent and rarely changed (fig. 8 and fig. 2.8 of appendix 2). The mean, minimum, and maximum S-wave velocities are summarized in table 1.

The RR-produced S-wave velocities (fig. 9) show similar features to the RR phase velocities (fig. 6) to depths of 20 km: low velocities of approximately −3 to −4 percent extend north and west from the 1256 C.E. eruption area (fig. 9). This pattern changes for 25 km depth, where low velocities are primarily distributed to the southeast and northwest edges of the field.

The inversion of the TT seismic components (fig. 10) resolves different structures from the RR seismic components, which is most likely due to the sampling difference between the Rayleigh and Loves waves (fig. 3). Because the two wave types sample different depths for each period, a joint inversion of Rayleigh and Love waves is not advisable. A high-velocity zone (1–3 percent) is observed near the 1256 C.E. eruption location at depths shallower than 15 km (fig. 10*A, B*). Although the velocities at 5–15 km depth vary within ±3 percent of the mean, greater depths have S-wave velocity deviations of approximately 8 percent at field edges (fig. 10). The velocity variations may be caused by a lack of depth resolution for the Love waves at longer periods (fig. 3*C*). The low-velocity feature extending northward from the 1256 C.E. eruption area observed only in the TT dispersion maps (fig. 7) is not observed distinctly in the inversion at shallow depths (fig. 10*A*). This feature may not be an artifact, because the dispersion maps are the closest results to the data and the feature is observed at most periods (fig. 7). The Love waves sample large volumes of the crust (fig. 3*C*), so what we observe for a single period in the surface-wave maps may be an effect of multiple features. Additionally, there may not be enough layers in the neighborhood algorithm inversion to resolve the feature at all nodes. Locations that do not show the low-velocity feature (for example, lat 24.5° N., long 39.6° E.) may have had dispersion curves whose fit was better reduced by placing layers at other depths or features.

Table 1. Four-layer inversion model (L4) shear-wave mean, minimum, and maximum velocity for the radial-radial and transverse-transverse components at 5-, 15-, 20-, and 25-kilometer depths.

[The percentage difference from the mean velocity is listed in parentheses. km, kilometer; km/s, kilometer per second; %, percent]

Depth (km)	Mean velocity (km/s)	Minimum velocity (km/s)	Maximum velocity (km/s)
Radial-radial			
5	3.64	3.52 (−3.3%)	3.74 (2.7%)
15	3.64	3.52 (−3.3%)	3.74 (2.7%)
20	3.75	3.58 (−4.6%)	3.88 (3.4%)
25	3.95	3.73 (−5.7%)	4.22 (6.6%)
Transverse-transverse			
5	3.53	3.44 (−2.6%)	3.65 (3.3%)
15	3.51	3.38 (−3.5%)	3.64 (3.7%)
20	3.80	3.51 (−7.6%)	4.11 (8.0%)
25	4.16	3.93 (−5.6%)	4.50 (8.1%)

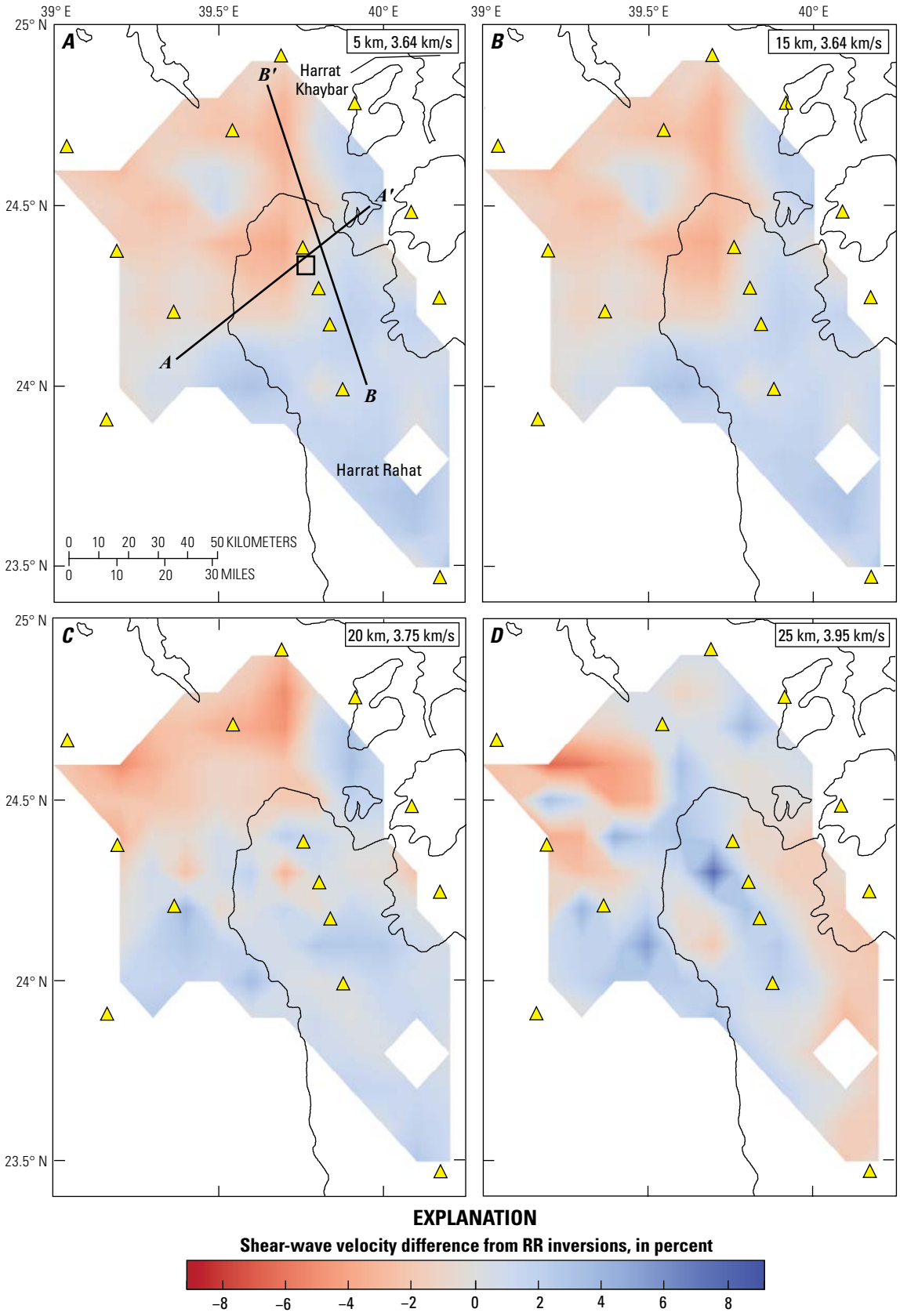

Figure 9. Maps of the northern Harrat Rahat area showing shear-wave velocity as a percentage difference from the mean using the radial-radial (RR) inversions (Rayleigh waves) for depths of 5 (*A*), 15 (*B*), 20 (*C*), and 25 kilometers (km) (*D*). Seismic stations are marked as yellow triangles, and the traces of the harrats are displayed as black lines. The location of the 1256 C.E. eruption vents is displayed as a black box in part *A*. The depth and mean shear-wave velocity for each panel, in kilometers per second (km/s), are displayed in an inset. Cross sections used in figures 11 and 12 are shown in part *A*.

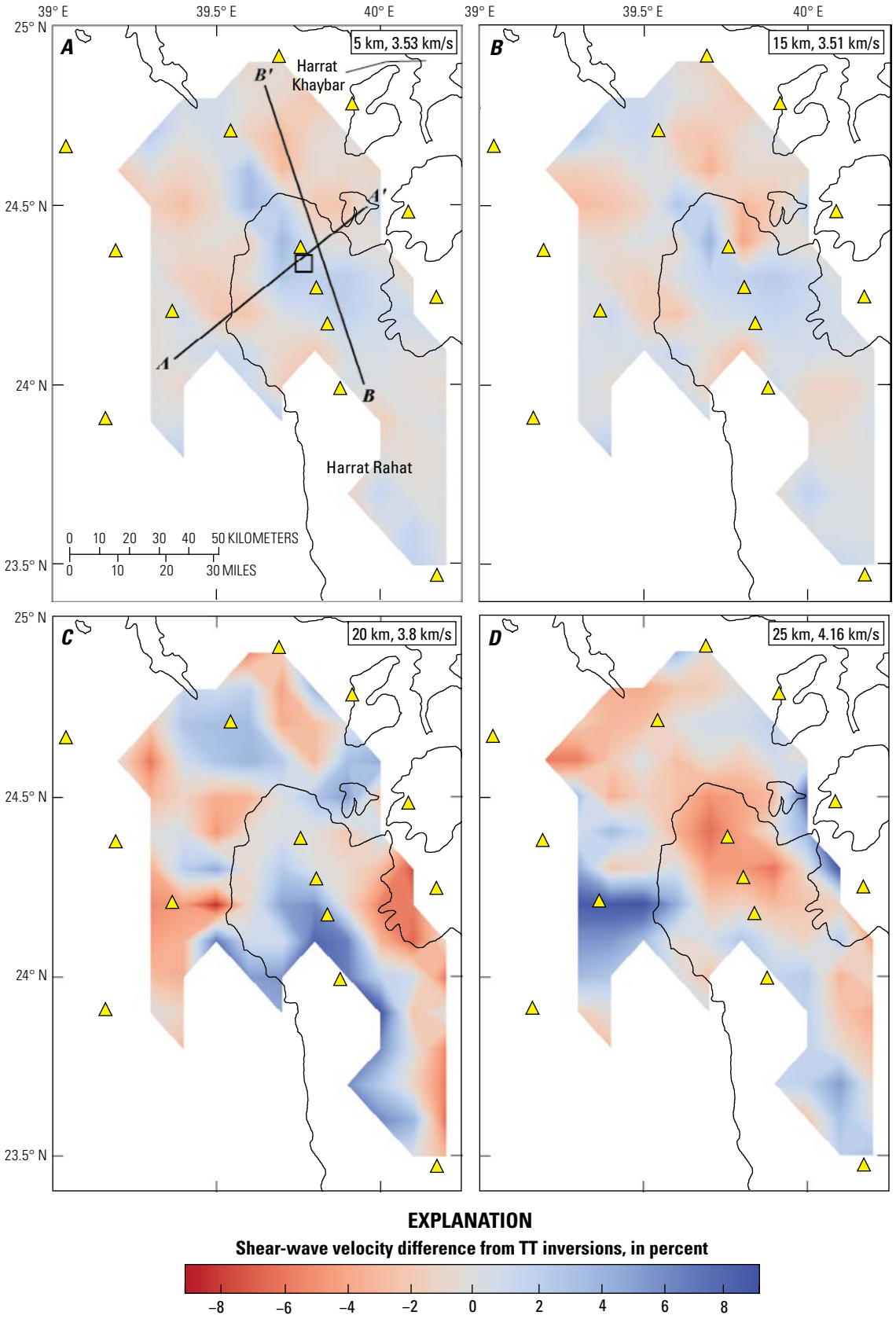

Figure 10. Maps of the northern Harrat Rahat area showing shear-wave velocity as a percentage difference from the mean using the transverse-transverse (TT) inversions (Love waves) for depths of 5 (*A*), 15 (*B*), 20 (*C*), and 25 kilometers (km) (*D*). Seismic stations are marked as yellow triangles, and the traces of the harrats are displayed as black lines. The location of the 1256 C.E. eruption vents is displayed as a black box in part *A*. The depth and mean shear-wave velocity for each panel, in kilometers per second (km/s), are displayed in an inset. Cross sections used in figures 11 and 12 are shown in part *A*.

Cross Sections

The S-wave velocity maps were interpolated with depth to produce a pseudo 3D model of the S-wave velocity distribution. Figures 2, 11, and 12 illustrate cross sections across Harrat Rahat through the 1256 C.E. eruption (*A*–*A*′) and alongside the low-velocity feature (*B*–*B*′).

The cross sections obtained from the Rayleigh waves indicate two relatively homogeneous crustal layers: an upper crust with shear-wave velocities of 3.5–3.6 km/s and a lower crust with velocities of 3.9–4.1 km/s (fig. 11) that are separated by a transitional interval at depths between 15 and 25 km. The cross sections show velocities of less than 3.6 km/s at distances 30–50 km along profile *A*–*A*′ and

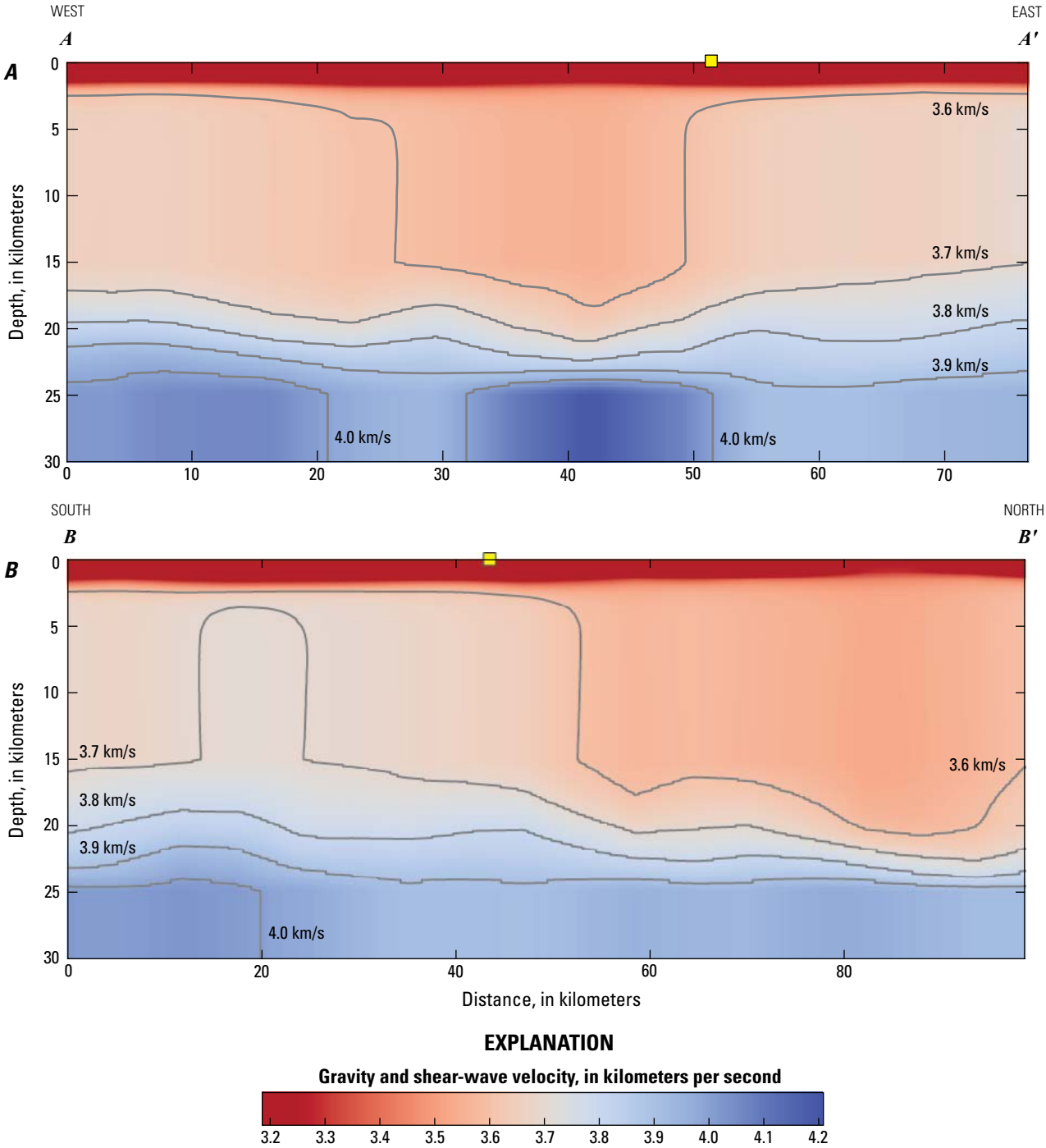

Figure 11. Cross sections *A*–*A*′ (*A*) and *B*–*B*′ (*B*) showing gravity and shear-wave velocity from absolute Rayleigh-wave phase velocities and inversion model L4. The location of the 1256 C.E. eruption is indicated by a yellow square. Cross section locations are marked in figures 2, 9*A*, and 10*A*. Shear-wave velocity contours for 3.6–4.0 kilometers per second (km/s) are displayed as gray lines.

beyond 50 km along profile *B*–*B*′ (fig. 11). Because of the lack of resolution of the Rayleigh waves at depths shallower than 5 km (fig. 3*B*), the thin low-velocity layer shown at the top of figure 11*A* and 11*B* should not be over interpreted.

Gravity and S-wave velocity cross sections constructed from Love-wave phase velocities (fig. 12) show similar shear velocities to those constructed from Rayleigh-wave phase velocities (fig. 11) but contain high-velocity (3.6–3.8 km/s) zones within the upper 7 km. These zones include the area beneath the locus of the 1256 C.E. eruption: 0–30 km and 40–65 km along *A*–*A*′ and 0–60 km along *B*–*B*′, respectively. Cross section *A*–*A*′ of figure 12, constructed from Love-wave phase velocities, shows faster velocities in portions of the lower crust (4.3–4.4 km/s) than cross sections constructed from Rayleigh-wave measurements (fig. 11). This velocity discrepancy could be due to a lack of depth resolution for

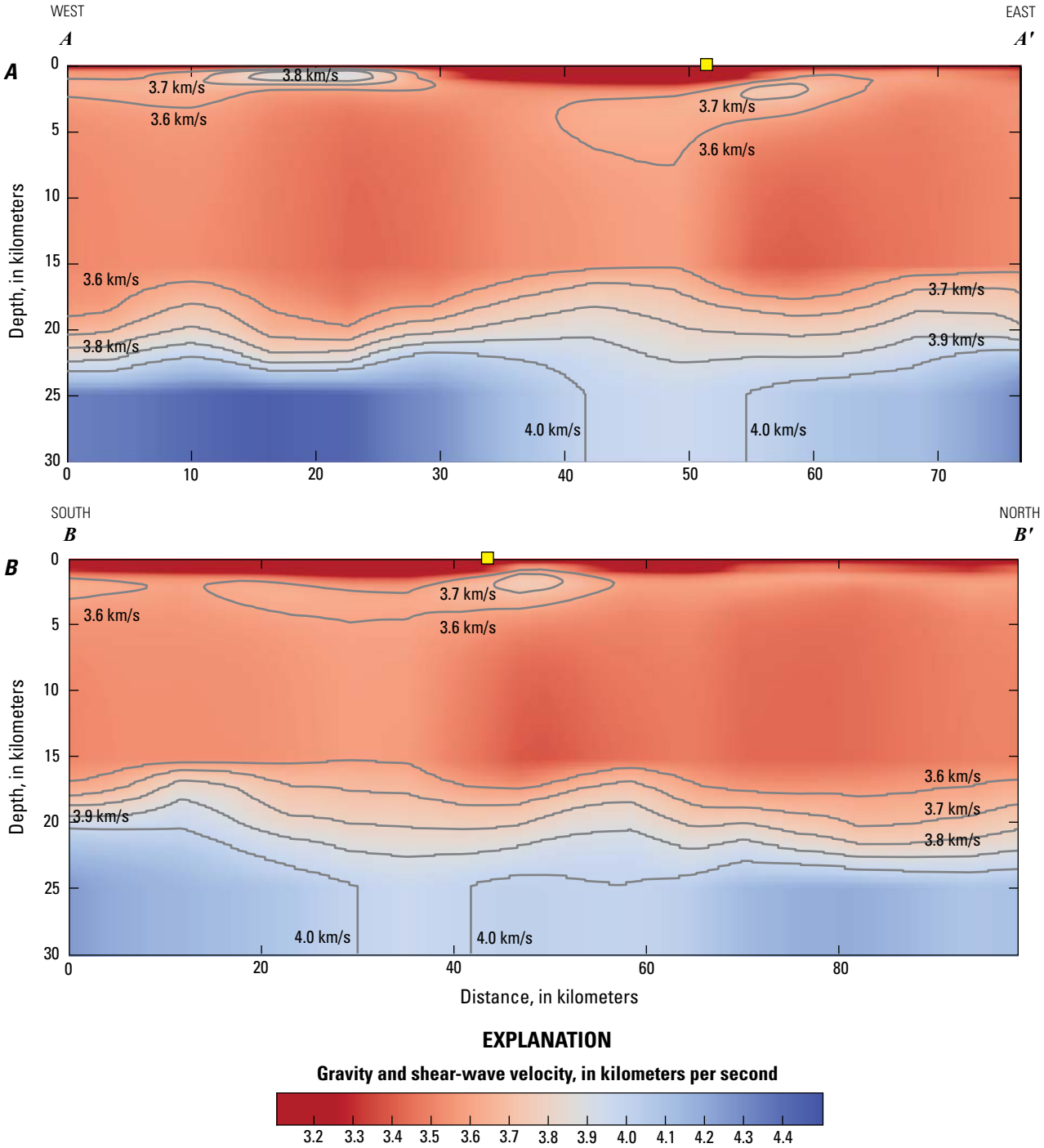

Figure 12. Cross sections *A*–*A*′ (*A*) and *B*–*B*′ (*B*) showing gravity and shear-wave velocity from absolute Love-wave phase velocities and inversion model L4. The location of the 1256 C.E. eruption is indicated by a yellow square. Cross section locations are marked in figures 2, 9*A*, and 10*A*. Shear-wave velocity contours for 3.6–4.0 kilometers per second (km/s) are displayed as gray lines.

Love waves compared to Rayleigh waves. Similar to what was observed using Rayleigh waves, the Love-wave cross section shows layer transitions at depths of 15 to 25 km (fig. 12). Faster velocities were observed on the edges of the field in the S-wave velocity maps (fig. 10*C, D*).

Discussion

Assessment of a Crustal Magma Chamber

The surface-wave and S-wave velocity results can be used to assess the presence of a crustal magma chamber in northern Harrat Rahat. The presence of a magma chamber in the top 30 km is unlikely owing to the observed modest magnitude of the shear-wave velocity variations, the extent of low- or high-velocity zones away from Harrat Rahat, and the lack of velocity reversals in the L4 and L5 inversion models. However, the methodology of ambient noise imaging and the frequency of the ambient noise source used in our analysis produce fundamental accuracy limitations at shallow depths (< 5 km) and may average out structures with dimensions smaller than 15 km.

The Rayleigh and Love surface-wave maps resolved perturbations of about ±3 percent from the mean for 5- to 12-second periods (figs. 6, 7). The computed S-wave velocity measurements were between ±3 and ±5 percent for Rayleigh waves and between ±3 and ±8 percent for Love waves. However, the ±8 percent deviations occurred at depths greater than 20 km at the edges of the field and may reflect a lack of depth resolution for the Love waves.

Surface and S-wave velocity studies of known magma chambers typically exhibit a larger decrease in S-wave velocity than we have determined at northern Harrat Rahat. An ambient noise study of the Toba Caldera in Indonesia recorded a maximum Rayleigh velocity deviation of about –24 percent (using 2.5- to 12-second periods) correlated with the location of a known magma chamber at 10–20 km depth (Stankiewicz and others, 2010). Behr and others (2011) used ambient seismic noise and the neighborhood algorithm of Wathelet and others (2004) to compute a pseudo 3D tomographic map of the central North Island of New Zealand. They found an area of low S-wave velocity at shallow depths within the Taupo Volcanic Zone, a volcanic area with active rifting (Wilson and others, 1995). Behr and others (2011) observed S-wave velocities between 2.6 and 3.1 km/s in the top 15 km below the Taupo Volcanic Zone, which is an 11–26 percent decrease compared to the surrounding S-wave velocities of 3.5 km/s. Similar results were found at depths shallower than 15 km below the Yellowstone Caldera by Stachnik and others (2008): a 2.8 km/s low-velocity zone among approximately 3.4 km/s crust (18 percent decrease). A recent full-waveform tomographic study using regional earthquakes in the Long Valley Caldera in the U.S. State of California revealed a S-wave velocity decrease of more than 20 percent at depths of 5–20 km, which enables the percentage of melt within the magma reservoir to be estimated (Flinders and others, 2018).

The 3–8 percent velocity changes we observed at northern Harrat Rahat in the top 30 km are substantially smaller than velocity changes observed in other tomographic studies of magmatic systems (18–26 percent), but shallow structures with a small velocity deviation are difficult for our methodology to resolve. Solidified magma can produce high-velocity zones in crustal tomography. For example, an active source study revealed a high-velocity zone at 5 km depth below the Asama volcano in Japan that was approximately 20 percent faster than the surrounding crust and was attributed to cooled magma from repeated intrusions (Aoki and others, 2009). Brenguier and others (2007) imaged to a depth of 4 km beneath the Piton de la Fournaise volcano of Réunion Island (Indian Ocean) at periods less than 5 seconds and found a 5 percent S-wave velocity increase that they attributed to the presence of a solidified magma intrusion. The minimum source frequency in our study was 5 seconds, which samples (and averages) approximately the top 10 km of the subsurface (fig. 3*B, C*). If a crustal magma chamber was present, as in what was observed at the Asama volcano (Aoki and others, 2009), we would expect decreases in velocities much greater than the 3–8 percent velocity variations we observe in our study.

Low surface-wave phase velocities and shear waves are not exclusively located below Harrat Rahat (figs. 6–7, 9–10). The checkerboard tests demonstrate that the extension of the features away from the harrat is real and is not caused by smearing owing to the station-path distribution (fig. 5). Moderate low crustal velocities (3–8 percent reduction) that extend away from Harrat Rahat argue strongly against the presence of a localized crustal magma chamber. The presence of liquids decreases shear-velocities by increasing the effective density while keeping the effective shear modulus constant (Jones, 1980), and would also produce measurements of high conductivity. Our finding that modestly sub-average velocities are neither restricted to, nor are concentrated beneath, the harrat agrees with the resistivity survey of Bedrosian and others (2019) and Peacock and others (2023), which found apparent electrical conductors in the upper and lower crust extending well beyond the Harrat Rahat area. Bedrosian and others (2019) and Peacock and others (2023) showed that those large, strong apparent electrical conductors were artifacts of the 3D inversion method brought about by anisotropic conductivity in the Precambrian crust. Those authors confirmed this interpretation with 2D inversions that are less sensitive to anisotropy and that showed no such strong conductive anomalies beneath or beyond the harrat. Importantly, the conductive anomalies in the 3D inversion were not real, and the 2D inversions show that the crust beneath the volcanic field is indistinguishable in its conductivity structure from the crust beyond the field. Both regions lack strong anomalies that could signal the presence of a sizeable magma reservoir. The absence of sizeable magma reservoirs also agrees with the gravity results of Langenheim and others (2019, 2023), which indicate that the gravity low is not restricted to Harrat Rahat but instead extends north into the Precambrian basement.

The low-velocity feature observed in the Love-wave phase velocity maps (fig. 7) could be due to the presence of seismic anisotropy. Northern Harrat Rahat is undergoing northeast extension owing to slab-pull motion at the Zagros collision zone approximately 1,000 km away (Stern and Johnson, 2010; Reilinger and others, 2015), so cracks could form perpendicular to this extension direction (that is, the northwest fast direction). However, the Love-wave phase velocities (fig. 7) show low velocities oriented north to south, which indicate that this anisotropy is not likely due to crustal extension. Another explanation for the observed anisotropy between Rayleigh and Love maps could be vertically aligned magmatic dikes that would, in principle, reduce the wave speed of Love waves substantially more than the wave speed of the Rayleigh waves (Jaxybulatov and others, 2014; Hammond and Kendall, 2016). If vertically aligned magmatic dikes were causing anisotropy, then they would need to form a widespread system at least as broad as the 15 km minimum wavelength of the surface waves that we are considering. However, the feature may be produced by the different sampling depth between the Rayleigh and Love waves (fig. 3). If the feature is close to the surface, it will be observed with the Love waves but not the Rayleigh waves. This could be investigated in a future study by using shallow tomography techniques and higher frequency signals.

The nodal dispersion curves were inverted using 2- to 5-layer models (L2–L5). L4 and L5 models allowed for low-velocity zones within the parameter space (table 1.3 of appendix 1), which are typical in active magmatic areas (Guidarelli and others, 2011), but no low-velocity zones were required by the data. The period range of the dispersion curves is only 5–12 seconds, so models using additional layers may overfit the data. Instead of low-velocity zones, the Love-wave L4 inversion modeled several high-velocity zones within the top 5 km (fig. 12).

Although we are careful to quantify the systematic error within our results, the methodology itself contains limitations on imaging resolution. The four main sources of error in the ambient noise methodology that could directly affect our conclusions are (1) the limited seismic wavelengths of the ambient noise source, (2) the sampling depth of the surface waves, (3) the station distribution of the seismic network and the interstation path lengths, and (4) tomography model spatial sampling (discretization). The effect of the surface-wave wavelength and sampling depth averaging on our final result is difficult to quantify directly. Ambient noise peaks at periods of 7 and 14 seconds (Bonnefoy-Claudet and others, 2006), which correspond to wavelengths of 21 and 42 km assuming a wave speed of 3 km/s, but its overall distribution varies from station to station. We were able to obtain ambient noise signal at a minimum of a 5-second period (fig. 2.1 of appendix 2), or a 15 km wavelength. Similarly, the depth sensitivity of the surface waves can only be estimated using sensitivity kernels, which are calculated from empirical relations and an input velocity model (fig. 3).

The effect of path lengths and the discretization of the tomography model can be further assessed by quantifying the minimum size of volcanic structure that can be observed with our network configuration (0.1 decimal degree discretization) and model smoothing parameters. We constructed an additional checkerboard model with a single 0.2° × 0.2° (22 × 22 km) low-velocity feature in the center of the field (fig. 2.9 of appendix 2). The low-velocity feature is 2.8 km/s, or a 20 percent decrease from the 3.5 km/s velocity of the surrounding rocks. Despite the large amount of smoothing, the feature can still be clearly observed in the surface-wave velocity maps albeit with a degree of northwest smearing (fig. 2.9 of appendix 2). The discretization of the velocities and smoothing parameters only diminished the feature from a 20 percent decrease to a 15 percent decrease. A 0.1° × 0.1° (11 × 11 km) low-velocity feature produced even larger degrees of smearing and could not be properly constrained but still imaged a 10 percent decrease in the low-velocity feature, which is more than three times the maximum negative velocity change observed in the dispersion maps (figs. 6–7, 9–10). These results indicate that our method has a spatial resolution of about 15 km.

Comparison with Other Studies

The dispersion and shear-wave velocity maps of northern Harrat Rahat were compared to results from prior geophysical studies to assess potentially conflicting mechanisms. Cross sections (figs. 11, 12) revealed a S-wave velocity increase from 3.5–3.6 to 4.0–4.1 km/s, representative of a change in density in crustal layers at depths of 15–25 km. This interface depth matches the boundary between a heterogeneous and broadly andesitic upper crust with the mafic lower crust in the Arabian Shield. This boundary has been inferred outside Harrat Rahat from refraction surveys (Mooney and others, 1985) and is consistent with xenolith data (Stern and Johnson, 2010).

We compared S-wave velocities obtained by other studies with the average velocities at upper crustal (5 km) and lower crustal (25 km) depths: 3.64 and 3.95 km/s (Rayleigh, RR cross-correlation component) and 3.53 and 4.16 km/s (Love, TT cross-correlation component) (table 1). These results are similar to the average crustal values obtained from country-wide surface-wave studies using regional earthquakes (3.69 and 4.1 km/s) (Mokhtar and others, 2001) and inverted surface-wave phase velocities from teleseisms (3.75 and 4.07 km/s) (Park and others, 2008).

Abdelwahed and others (2016) obtained seismic P-wave velocity deviations using travel-time residuals from local and teleseismic earthquakes recorded using a borehole array at Harrat Rahat and found several zones of low and high velocities. They found two main low-velocity anomalies with a reduction of 5 to 8 percent from the mean: (1) one low-velocity was underneath the 1256 C.E. eruption location at 2–10 km depth and (2) one was to the southeast from 22 to 46 km depth coinciding with the 1999 earthquake swarm

location (black square and red outline of fig. 2, respectively). Abdelwahed and others (2016) hypothesized that the low-velocity zone in the lower crust is a magma reservoir fed by a deeper source (at 60–100 km depth) and is connected with another shallower reservoir located right underneath the 1256 C.E. eruption location. In addition to the two low-velocity zones, Abdelwahed and others (2016) found several high-velocity zones: (1) widespread in the surface layer (0–2 km); (2) southeast of the 1256 C.E. eruption at 4 km depth; (3) south of the 1999 swarm at 16 km; and (4) north of the 1256 C.E. eruption at 22–38 km depth. The size and depth of both of the seismic low-velocity features (aforementioned low-velocity features 1 and 2) and most of the high-velocity features (high-velocity features 2 through 4) observed by Abdelwahed and others (2016) should be within our imaging resolution.

Areas of low velocity extend from the 1256 C.E. eruption location to the west and northwest for Rayleigh waves at 5–15 km depth (about −3 percent) (fig. 9*A, B*) but not for the Love waves (fig. 10*A, B*), which may be due to the increased sensitivity of the Love waves to the high-velocity anomalies in surface layers. Neither the 25 km S-wave velocity maps (figs. 6*D*, 7*D*) nor the *B*–*B*′ cross section revealed a low-velocity zone at depths greater than 22 km below the 1999 swarm location. High-velocity features observed by Abdelwahed and others (2016) (features 2 and 3 as listed above) are observed in both Rayleigh and Love waves (figs. 9*A, B* and 10*A, B*) but the high-velocity feature north of the 1256 C.E. eruption at depths 22–38 km is only observed in Rayleigh waves (fig. 9*D*). Although we observe similar features to Abdelwahed and others (2016), we disagree with their conclusion regarding the existence of a magma chamber. Their imaged area is centered on the 1256 C.E. eruption location and is less than half the size of our study area for most depths. Hence, our coverage is more complete and robust.

Tang and others (2016) used seismic receiver functions and surface-wave data to derive average thicknesses of 12 km and 23.6 km for the upper and lower crust with average S-wave velocities of 3.63 km/s and 3.92 km/s, respectively. These S-wave velocities are in good agreement with our Rayleigh-wave shear-velocity results (3.5–3.6 km/s and 4.0–4.1 km/s). However, several details of the Tang and others (2016) analysis differ from our tomographic images. The first is a 10-km-thick low-velocity layer overlaying a 10-km-thick high-velocity layer observed between depths of 5 and 25 km depth at seismic station RHT05 (Tang and others, 2016) (fig. 2) that is not discernible in our *A*–*A*′ cross sections (figs. 11*A*, 12*A*). Additionally, the velocities calculated by Tang and others (2016) at 5 km depth at RHT02 and RHT05 (about 4 km/s) (fig. 2) are much faster than in our models (figs. 9*A*, 10*A*) and are instead values that would be expected for the lower crust instead of near-surface layers. We hypothesize that these differences may be due to three factors: (1) the 2.5 km step of the inversion algorithm; (2) the difficulty of the receiver function method used by Tang and others (2016) to obtain absolute velocities, and (3) insufficient short-period seismic energy (< 12 seconds) in the group velocity dispersion curves obtained from regional and teleseismic earthquakes.

Tang and others (2018) used Rayleigh-wave group velocities to determine S-wave velocities across the Arabian Shield. They found a 2–5 percent S-wave velocity decrease underneath Harrat Rahat at depths shallower than 25 km. This result was recently verified using S-wave velocities obtained from a joint inversion of Rayleigh-wave group velocity dispersion curves and P- and S-wave receiver functions (Tang and others, 2019). We see similar decreases in S-wave velocity in the upper crust for Rayleigh waves (−3 to −4 percent) (table 1, fig. 9), but the low velocities for the inversion using Love waves are primarily off of the harrat for the upper crust (fig. 10).

Seismic Structure of the Arabian Shield

Seismic Network and Instrument Information

In this section, ambient seismic noise tomography is applied to determine the S-wave crustal structure of the Arabian Shield, and data from the same period as the Harrat Rahat subset are used (January through December 2014). Some stations were installed late in the year or had frequent outages, and only stations that had at least 6 months of data were considered. We used a total of 73 broadband seismometers for this analysis (fig. 13). Unlike the northern Harrat Rahat network, which was of a single instrument type, this new dataset contains T120, T40, and STS2 seismic instruments. The frequency response range is approximately 0.01–20 Hz for the instruments with the broadest bandwidth (Streckeisen, 1995; Townsend, 2014; Passcal, 2016) and 0.1–10 Hz for the standard seismometers (Nanometrics, 2009). The differences in bandpass do not require changes to the methodology because values produced are unaffected by missing energy in certain parts of the frequency spectrum. Instead, the signal simply would not coherently stack for those frequencies in the cross-correlation function. The labels of different station types in figure 13 were used to assess possible instances of asymmetry owing to missing low-frequency energy. Additional stations from the Saudi Arabia Seismic Network were not included in this analysis, because the interstation path between stations was too large, which would cause smearing and loss of resolution in the tomographic maps. As expected from the northern Harrat Rahat results, both the primary (12- to 18-second periods) and secondary (6- to 9-second periods) microseism bands (Friedrich and others, 1998) were recorded at all stations and directional components. Figure 4.1 of appendix 4 displays the probability density functions, weighted mean, and the new high- and low-noise models of Peterson (1993) for the vertical component of one of the broadband stations (station AFFS) (McNamara and Boaz, 2011).

Methodology for Large Array

The methodology for this country-wide dataset was the same as that discussed in the "Methods" section with slight modifications to account for the increased number of paths and interstation distance. About half of possible station-pair combinations (fig. 13) passed our stipulated threshold requirement of a signal-to-noise ratio of 10:2,390 (RR component), 2,353 (TT component), and 2,607 (ZZ component). The positive and negative sides of the cross-correlation function were stacked together to increase signal-to-noise ratio, and AFTAN was used to calculate group and phase-velocity surface-wave dispersion curves for 5- to 25-second periods.

Errors in the tomography owing to inaccurate estimates of surface-wave velocities are propagated through to S-wave velocity inversions; therefore, careful selection criteria for the dispersion curves are necessary to minimize error. Dispersion curves may have some incorrect estimates of velocity for a part of the analyzed periods. Unlike our result presented in the "Cross-Correlation Moveouts" section of the results for northern Harrat Rahat, the dispersion curves could not be individually checked owing to the large number of interstation paths. Three dispersion curve exclusion steps were done: (1) partial exclusion of the AFTAN result, (2) an all-paths velocity threshold exclusion, and (3) exclusion of individual station paths. The purpose of these methods was to remove incorrect estimates of velocity that could cause smearing in the tomographic image.

A dispersion curve produced by the AFTAN of a cross correlation may be entirely spurious or can be partly usable. For example, certain dispersion curves with short interstation distances may have unusable velocities at long periods but correct velocities in the short period (and vice versa for large interstation distances). The AFTAN result partial exclusion is twofold: (1) if the value of the group velocity is greater than the phase velocity or (2) if two times the wavelength is greater than the interstation distance, then the velocity values for that period are removed. The second part of the condition, commonly called the two-wavelength criteria in ambient noise literature, is to ensure that surface waves complete a full cycle (Shapiro and others, 2005; Brenguier and others, 2007). The dispersion curves are entirely removed if their minimum period is 10 seconds or higher after the two exclusions.

We use another exclusion principle, referred to as the all-paths velocity threshold exclusion, to sort the remaining dispersion curves. Unlike the previous exclusion, which assesses each dispersion curve individually, the all-paths velocity exclusion assesses the dispersion curves from each cross-correlation component as an aggregate. This step was done to remove the dispersion curves whose velocities were much faster or slower than what was expected for Rayleigh or Love waves. Minimum and maximum velocity thresholds were selected for each wave type (for example, Rayleigh-wave group velocities and Love-wave phase velocities) on the basis of the distribution of all of the dispersion curves (table 3.1 of appendix 3). If a dispersion curve crossed or was outside these thresholds, then it was removed. Figure 14 shows the result of this exclusion method for ZZ component phase velocities. The number of cut dispersion curves for each wave type is listed in table 3.1 of appendix 3.

Anomalously high or low dispersion curves can still be present despite the first two dispersion curve exclusion steps. A station-path exclusion criteria was established to find anomalous dispersion curves within the all-paths velocity thresholds. The standard deviation of station pairs using a fixed single station was computed. If a dispersion curve was greater than 1.5 standard deviations from the median at any period, it was removed (fig. 15). The median was used to minimize the contribution of large outliers (fig. 15*A*). The threshold of 1.5 standard deviations was chosen on the basis of trial and error. Larger standard deviations did not exclude anomalous dispersion curves, which resulted in high or low velocity streaks in the tomographic results, whereas smaller standard deviations reduced the number of paths with no apparent improvement.

The velocities at each period for the wave types were inverted into tomographic maps using the same nodal tomography algorithm used in the Harrat Rahat study (Barmin and others, 2001). We discretized the grid using 0.2° nodes (approximately 22 km at the equator). Barmin and others (2001) recommend $\sigma = 2l$, in which l is the separation between the nodes. However, a σ value of 50 km produced anomalously high or low values in certain regions, so we used a wider value (σ =200 km) as justified by the seismographic spacing. The amplitude of the smoothing was set to 800, following the $\alpha=4\sigma$ recommendation of Barmin and others (2001).

A checkerboard test was done using the paths available for ZZ phase velocities at a 6-second period (1,722 total paths) (fig. 16). We used 2° (222 km at the Equator) checkerboards of alternating 3.0 and 3.5 km/s velocities and calculated the expected velocity across each cross-correlation path using Fatiando software (Uieda and others, 2013). To better understand the accuracy, we excluded any nodes from the color bar whose velocity was 0.1 km/s faster or slower than the input velocities (that is, any velocities > 3.6 km/s or < 2.9 km/s that correspond to poorly constrained portions of the model). The tomography underpredicted the input model in a region near Harrat Khaybar. This error is most likely due to a lack of stations and paths north of the harrat and should produce similar underpredictions in the inversions of all wave types.

Sensitivity kernels were computed using the Senskernel software package (Levshin and others, 1989; Levshin, 2013) (fig. 17, fig. 2.2 of appendix 2). We used a simple three-layer model as input, which consisted of P-wave velocity from Mooney and others (1985); S-wave velocity from Park and others (2008); and layer densities from Al-Saad and others (1992), Brew and others (2001), and Stern and Johnson (2010). The computed Rayleigh-wave kernels are more sensitive to deeper structure compared to Love-wave phase velocities, but each wave type should have at least partial resolution down to at least 40 km depth (fig. 17, fig. 4.2 of appendix 4). Despite this 40-km maximum resolution, sharp seismic boundaries such as the Mohorovičić discontinuity are difficult to interpret in these results owing to the large wavelength of the ambient noise signal and poor resolution for depths greater than 30 km.

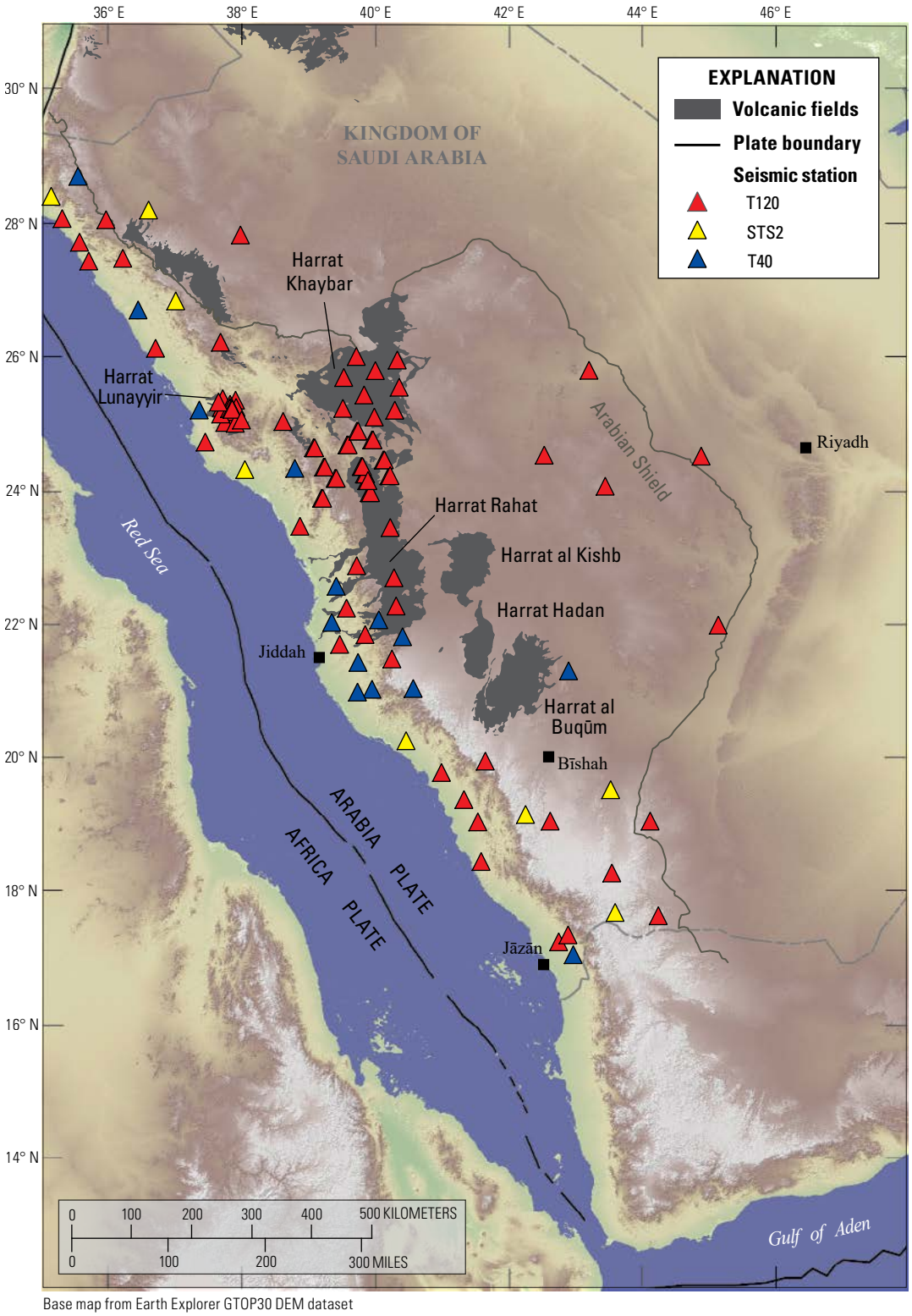

Figure 13. Map of the western part of the Saudi Arabia Seismic Network showing the distribution of seismic stations by type. Broadband instruments T120, STS2, and T40, are displayed as red, yellow, and blue, triangles, respectively.

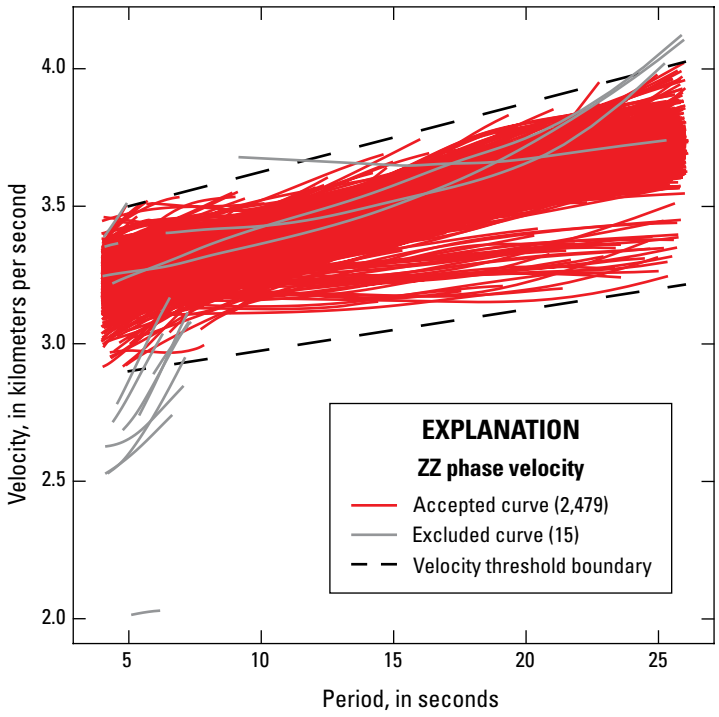

Figure 14. Graph of velocity threshold dispersion curve selection for the vertical-vertical (ZZ) component. Lines of minimum and maximum thresholds are displayed as dashed black lines. Accepted and excluded dispersion curves are displayed as red and gray lines, respectively.

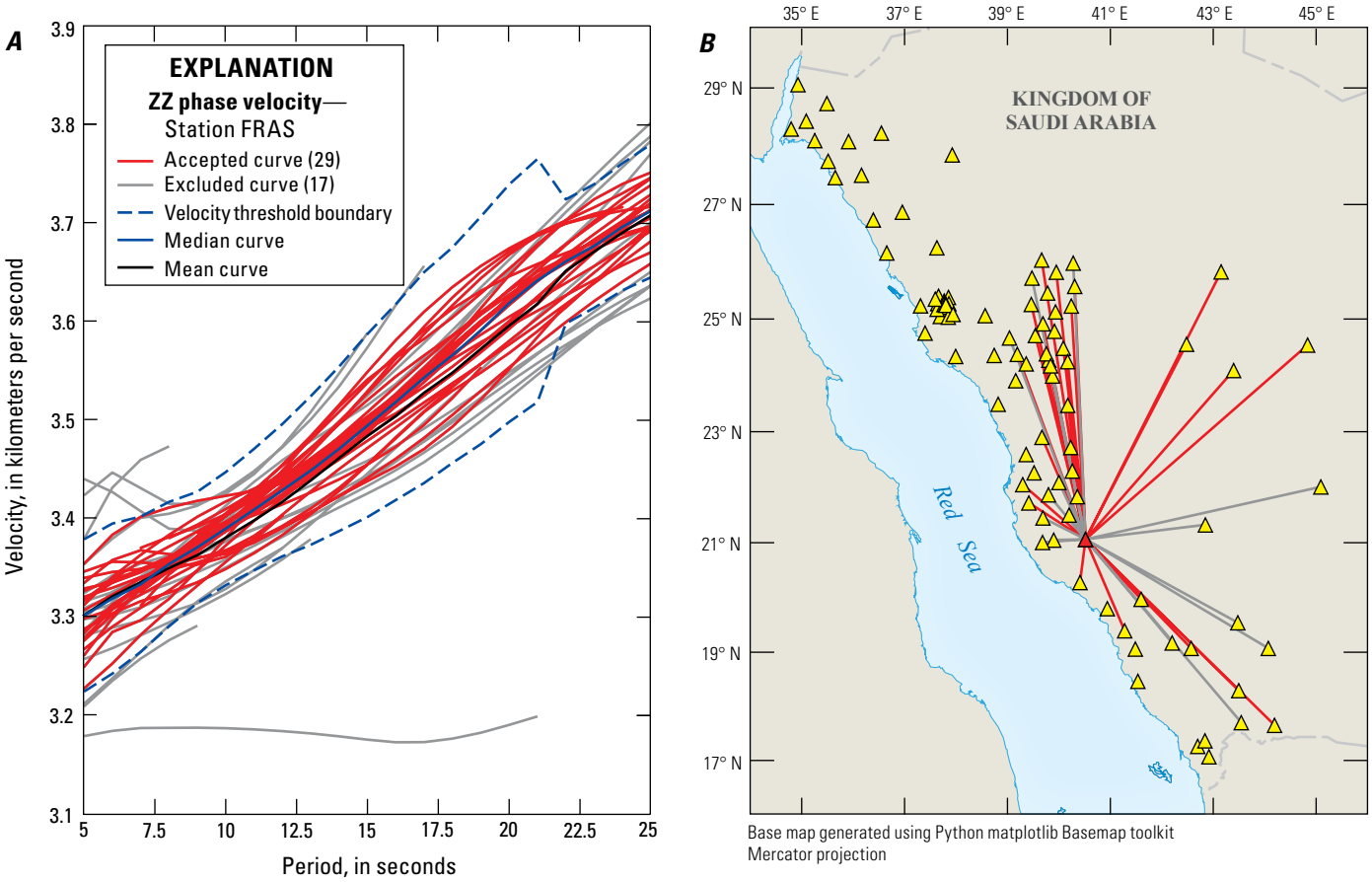

Figure 15. Graph and map showing station-based dispersion curve selection of seismic stations (yellow triangles) in Saudi Arabia. *A*, Graph showing the accepted and excluded dispersion curves for station paths of station FRAS vertical component (ZZ) phase velocities. Dispersion curves more than 1.5 standard deviations (dashed blue line) from the median are removed. *B*, Map of the Red Sea and Arabian Peninsula region showing the azimuthal coverage of the station paths corresponding to the dispersion curves displayed in part *A*. Red triangle in part *B* represents station FRAS.

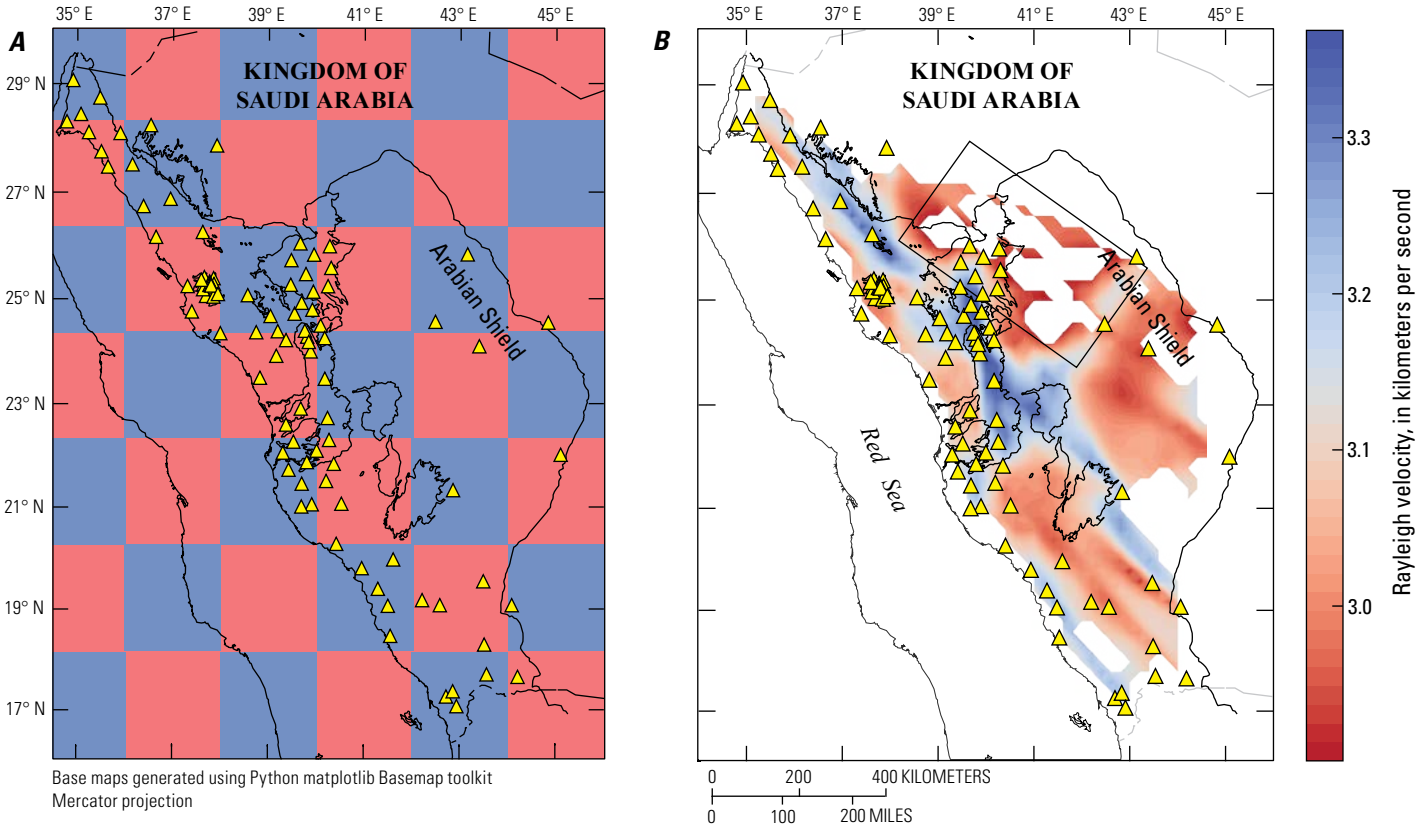

Figure 16. Maps of the Red Sea and Arabian Peninsula region showing the input checkerboard model with 2° spacing of 3.0 (red) and 3.5 kilometers per second (blue) tiles (*A*) and the output tomography from the checkerboard model (*B*). A zone in which the tomography underpredicts the input model is encased by a black outline shown in part *B*. Seismic stations are labelled as yellow triangles. The location of the harrats (volcanic fields) was obtained from Camp and Roobol (1992) and Pollastro and others (1999).

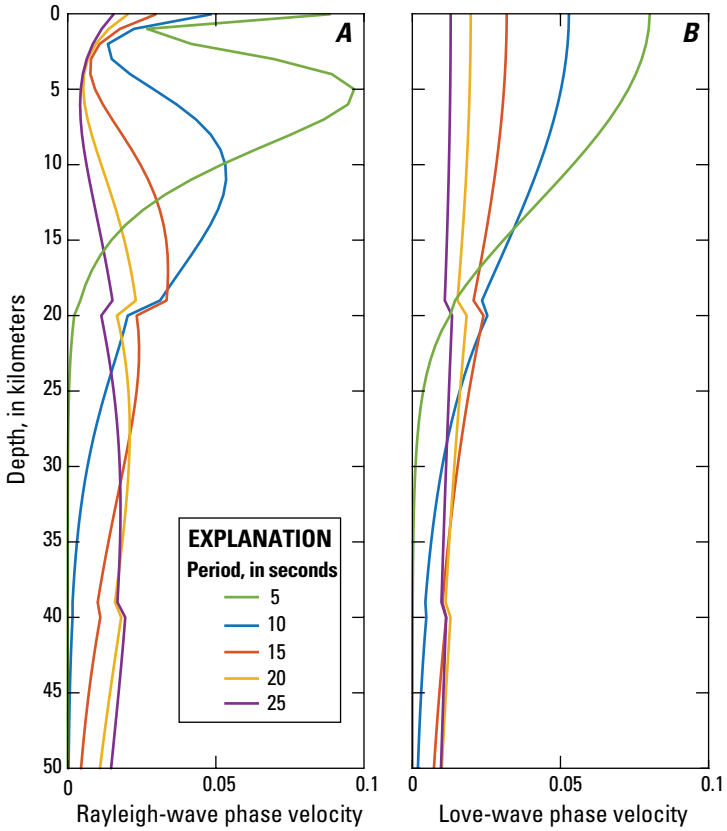

Figure 17. Graphs of phase velocity sensitivity kernels calculated using the Senskernel computer program (Levshin, 2013) for Rayleigh (*A*) and Love waves (*B*).

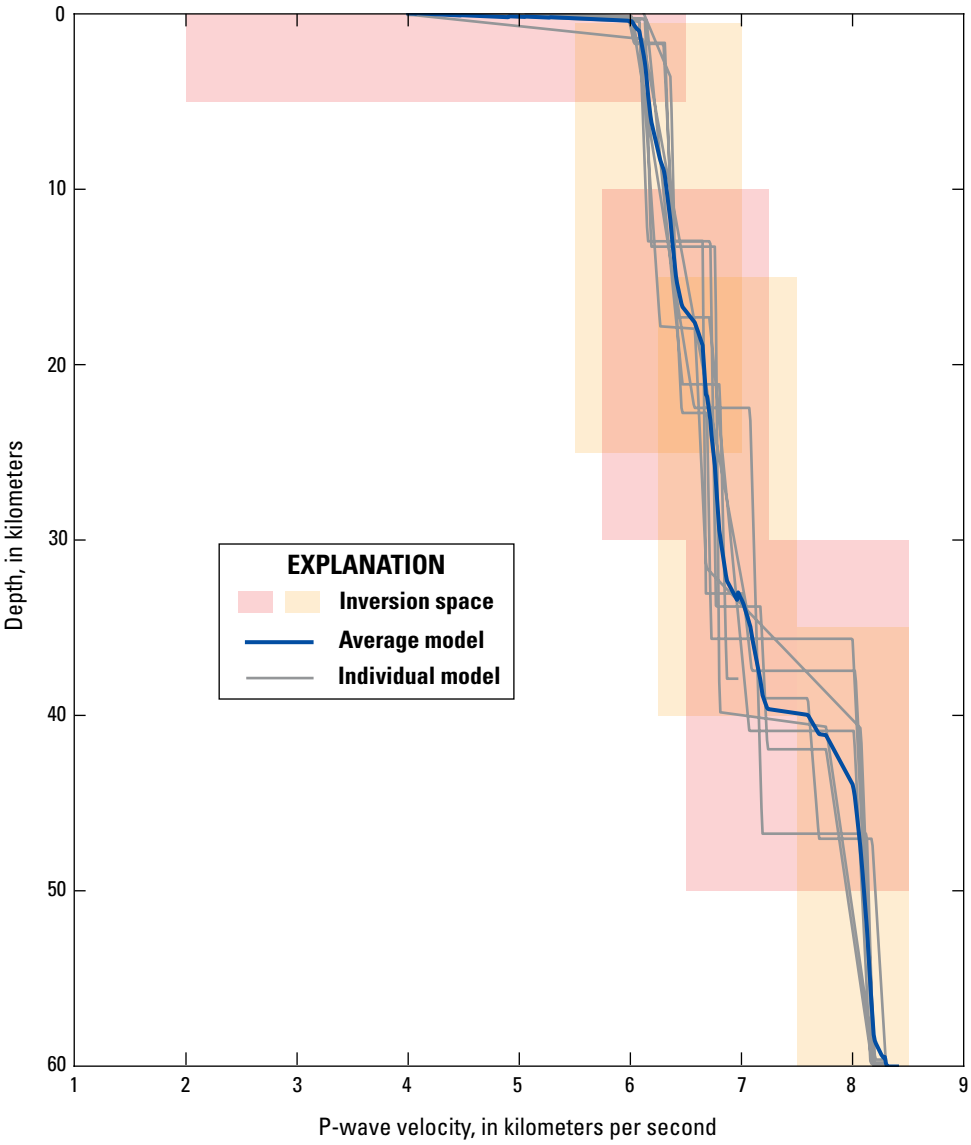

Figure 18. Graph of seismic shear-wave inversion model parametrization that is based on the compressional wave (P-wave) velocity results of Mooney and others (1985). Models of the refraction survey are displayed as gray lines and their average is in blue. Shaded areas of red and orange correspond to the shear-wave velocity inversion parameter space used in the Dinver software (table 3.2 of appendix 3).

Seismic Shear- Wave Velocity Inversion

Rayleigh-wave and Love-wave velocities are extracted at each node for 5- to 25-second periods. The dispersion curves at each node are then inverted using the Dinver software package (Wathelet, 2005, 2008). As previously discussed in the "Shear-wave Velocity Inversion" section for the northern Harrat Rahat dataset, geological or mechanical features with dimensions smaller than the wavelength used to image may be obscured. We chose a five-layer input velocity model with half space on the basis of the results of a seismic refraction survey (Mooney and others, 1985) (fig. 18, table 3.2 of appendix 3). The Mooney and others (1985) model needed to be implemented in the Dinver computer code as S-wave velocity to obtain accurate 1D S-wave velocity inversions. The P-wave velocity boundaries were converted to equivalent S-wave measurements using V_P/V_S ratios from other crustal studies: 1.73 for the upper crust, 1.77 for the lower crust, and 1.78 for the mantle (Mooney and others, 1992; Chulick and others, 2013). Low-velocity layers were allowed for each inversion.

We computed two inversions at each node on the basis of the type of surface wave being considered: a joint inversion of the RR and ZZ components (both Rayleigh wave) and an inversion of the TT component (Love wave). An example of the output of the Dinver inversion for the point at lat 23.0° N., long 41.0° E. is displayed in figure 4.3 of appendix 4. Each 1D S-wave velocity inversion was then interpolated to produce a pseudo-3D model.

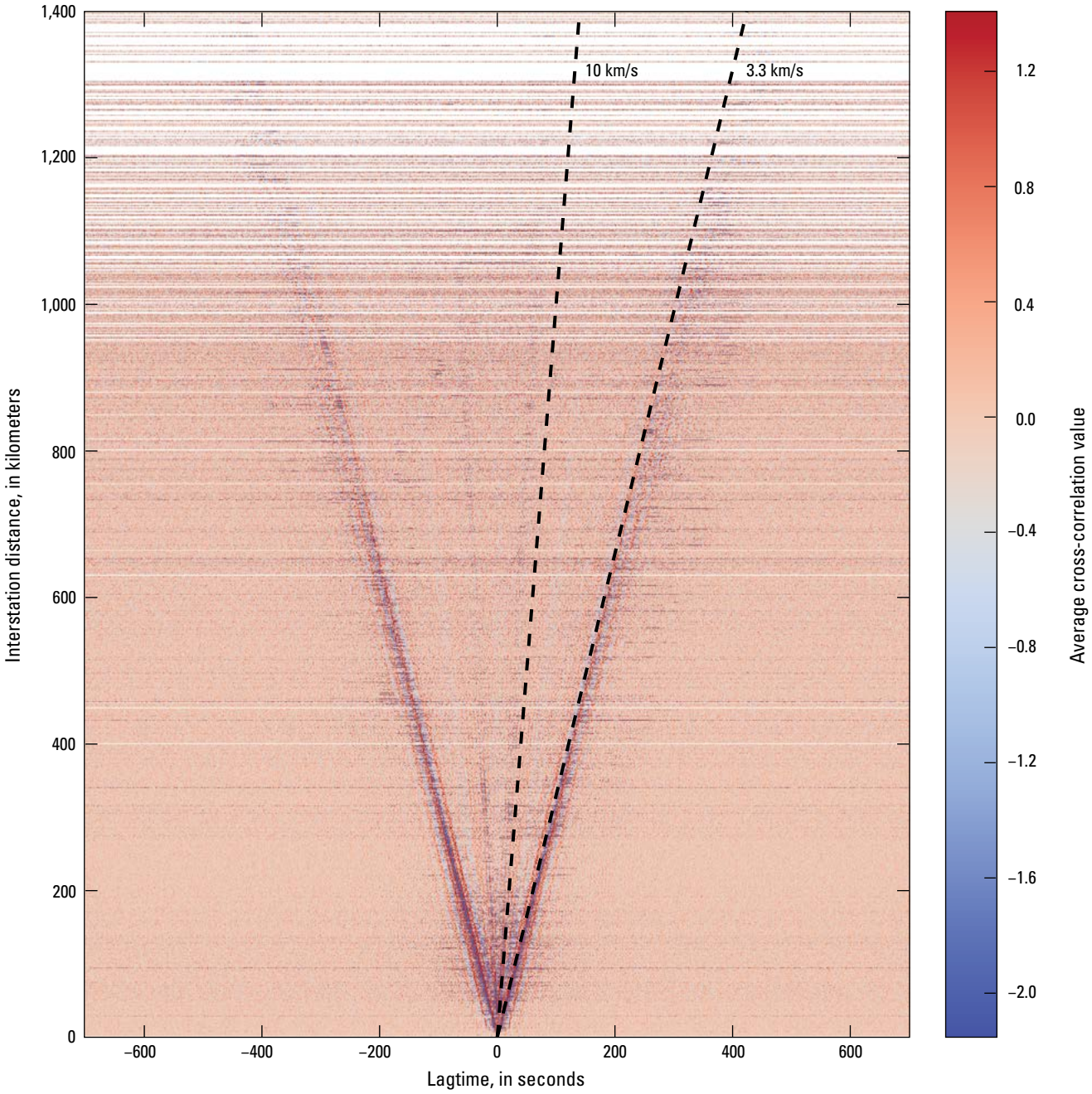

Figure 19. Cross-correlation moveouts with a signal-to-noise ratio greater than 5 for Arabian Shield seismic station pairs for the radial-radial component (5,814 station paths). Surface-wave moveouts can be observed at approximately 3.3 kilometers per second (km/s).

Arabian Shield Results

Cross correlations were computed for each of the principal components of the Green's function tensors. Figures 19–21 display the cross-correlation moveouts for traces with a signal-to-noise ratio greater than 5: RR components, 5,814 pairs; TT components, 6,017 pairs; and ZZ components, 7,252 pairs. Two signals (approximately 3.3 km/s and 10 km/s) are observed within the cross-correlation moveouts of the RR and ZZ components. The lower seismic velocity signal is observed in all three components but has a higher seismic velocity in the TT cross-correlation moveouts. The higher velocity signal is also present in the RR cross-correlation moveouts at interstation distances of less than 400 km (fig. 19) but is not observed in the TT mveouts (fig. 20).

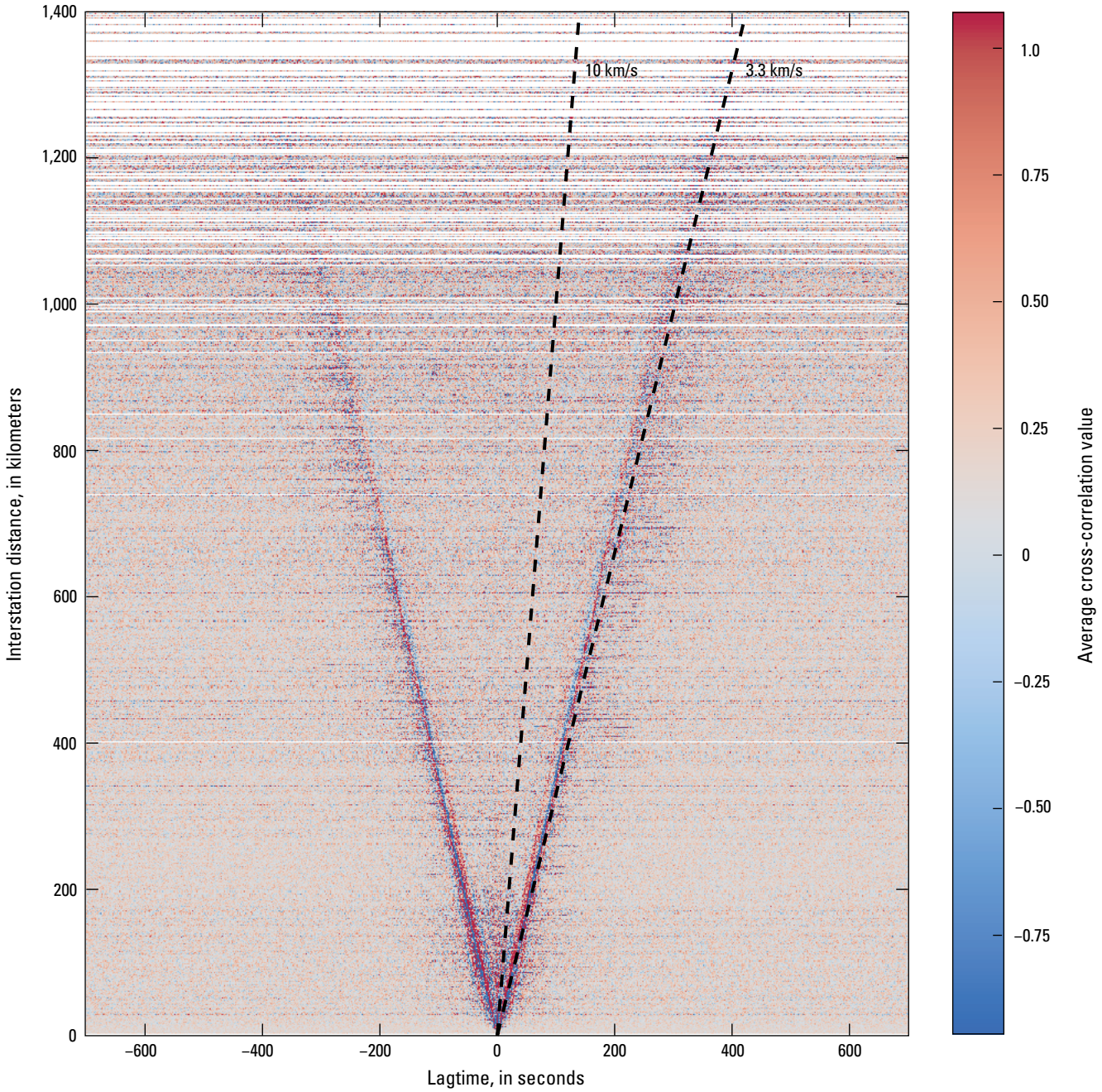

Figure 20. Cross-correlation moveouts with a signal-to-noise ratio greater than 5 for Arabian Shield seismic station pairs for the transverse-transverse component (6,017 station paths). In addition to surface-wave moveouts, we also observe body-wave moveouts propagating at 10 kilometers per second (km/s).

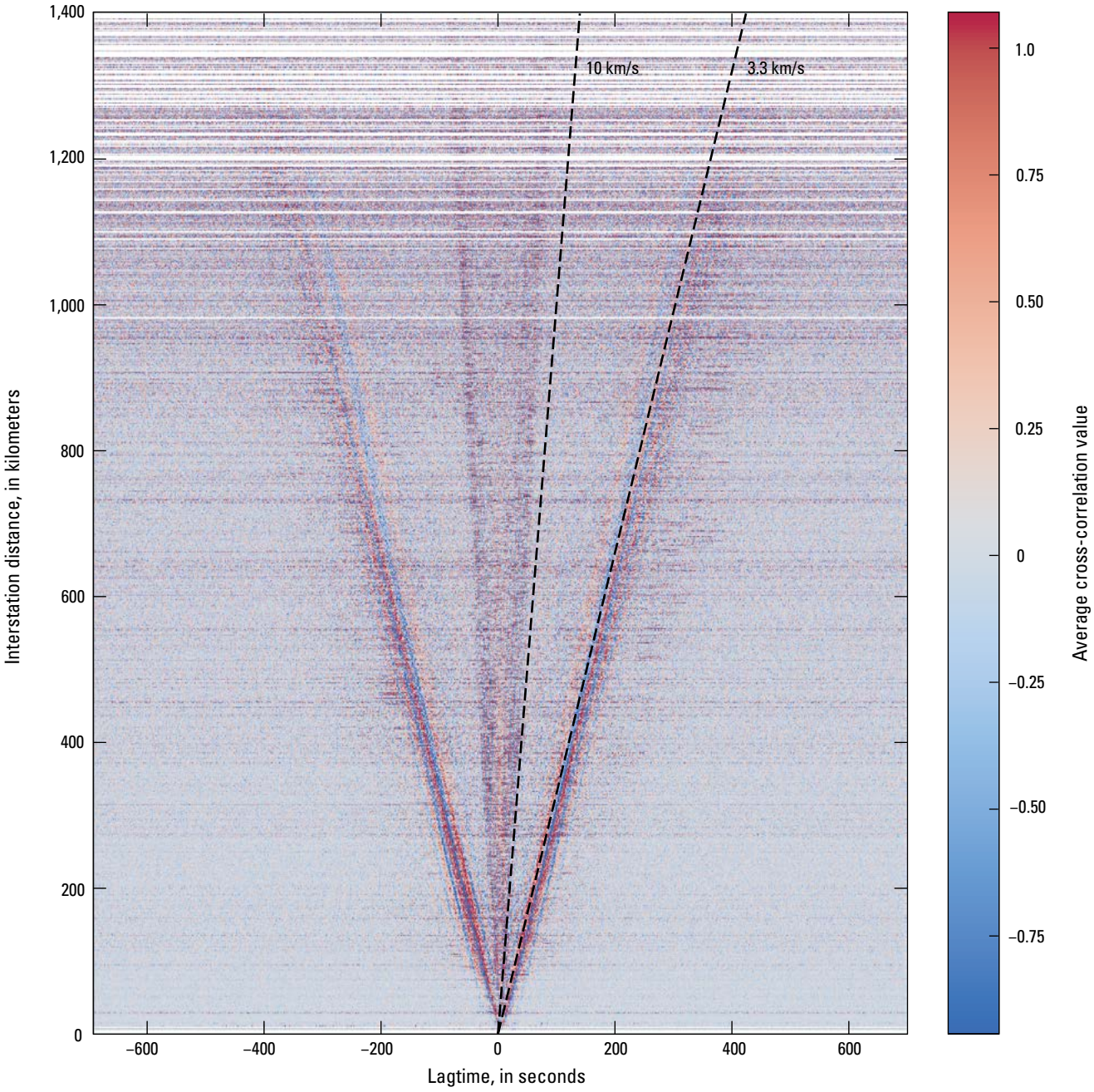

Figure 21. Cross-correlation moveouts with a signal-to-noise ratio greater than 5 for Arabian Shield seismic station pairs for the vertical-vertical component (7,252 station paths). Surface-wave and body-wave moveouts can be observed at approximately 3.3 and 10 kilometers per second (km/s).

Several similarities in the RR, TT, and ZZ phase-velocity dispersion maps can be observed (fig. 22, figs. 4.4, 4.5 of appendix 4). All three components vary between ±3 percent. The northern harrats (Harrats Khaybar, Lunayyir, and northern Rahat) contain low velocities throughout all periods. The southern harrats (Harrats al Kishb, Hadan, al Buqūm, and middle and southern Rahat) are instead characterized by high velocities at short periods (fig. 22, figs. 4.4, 4.5*A*, *B* of appendix 4) and lower velocities at long periods (fig. 22, figs. 4.4, and 4.5*C–E* of appendix 4). Low velocities are observed east of 40° E. and north of 24°N., which are co-located with the anomalous low-velocity zone in the checkerboard test (fig. 16). Similar features are observed in the S-wave velocity inversions of the Rayleigh- and Love-wave data (figs. 23, 24): S-wave velocities are low for the northern harrats throughout all depths and southern harrats contain low velocities in the lower crust (figs. 23, 24*A, B*).

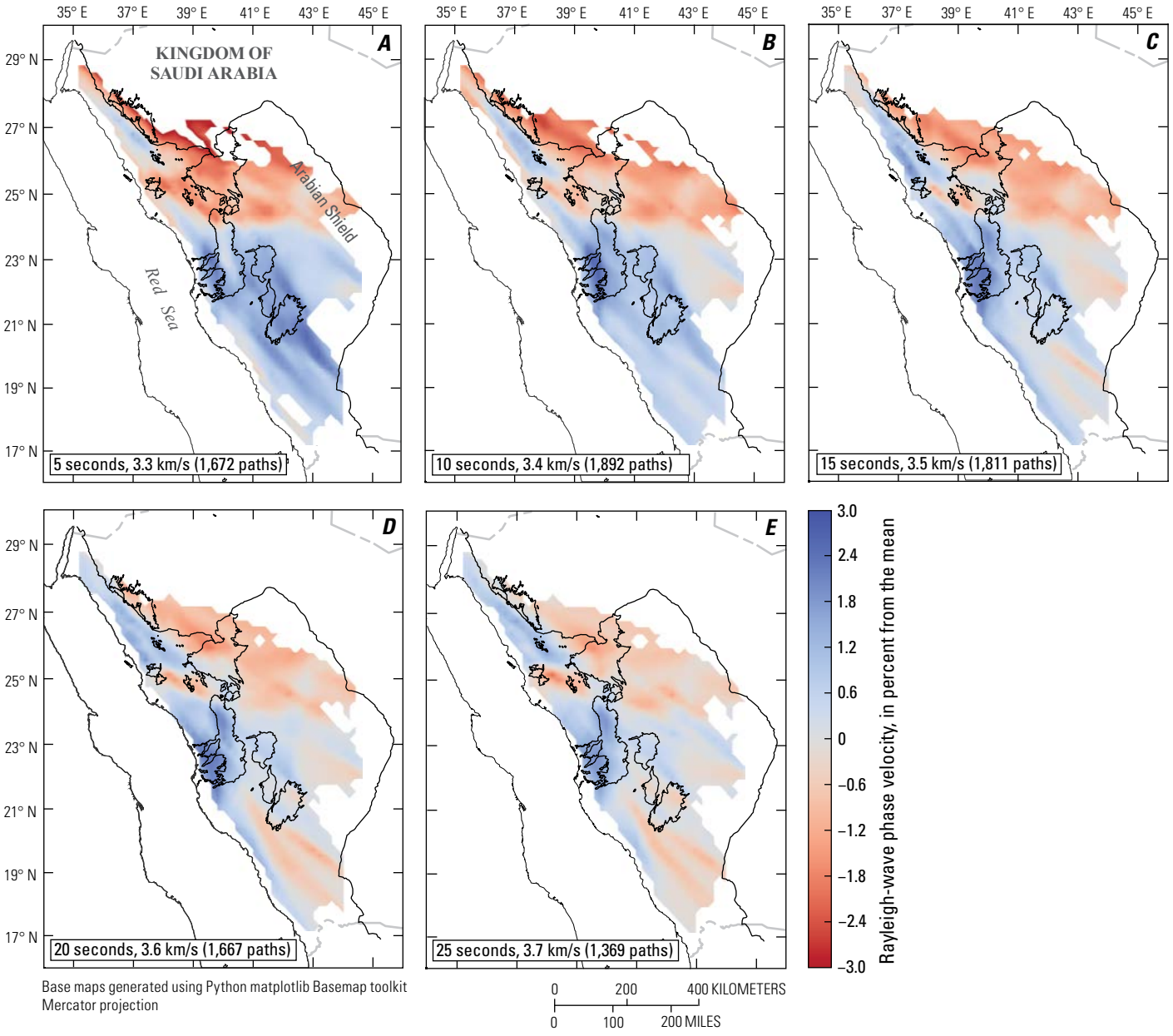

Figure 22. Maps of the Red Sea and Arabian Peninsula region showing the Rayleigh-wave phase velocity as a percentage difference from the mean, from the vertical-vertical cross-correlated component, for 5- (*A*), 10- (*B*), 15- (*C*), 20- (*D*), and 25- (*E*) second periods. The length of period, mean velocity in kilometer per second (km/s), and number of paths for each period are displayed in an inset. Figures 1 and 13 show the name and positions of the harrats (outlined in black) on the Arabian Shield.

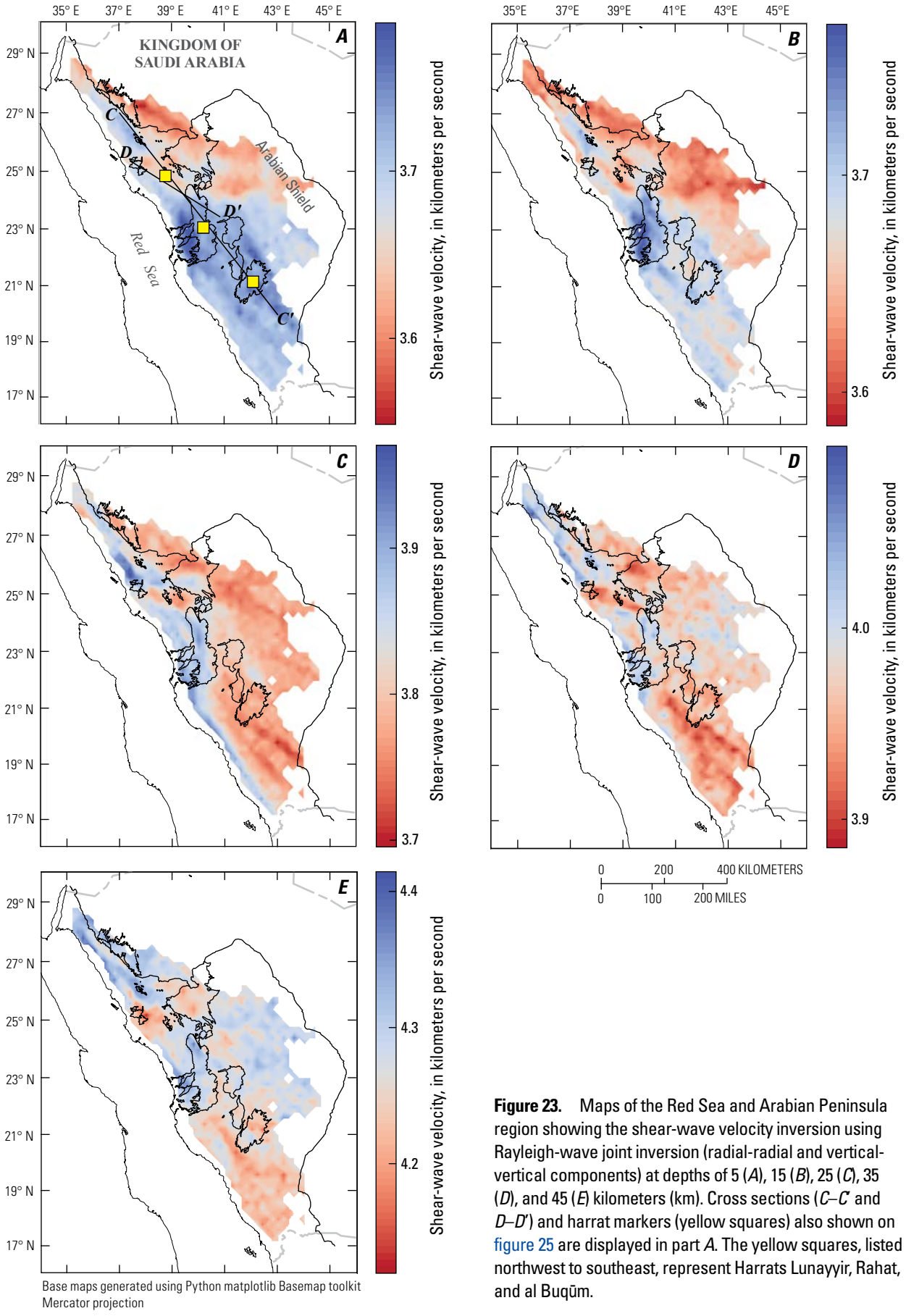

Figure 23. Maps of the Red Sea and Arabian Peninsula region showing the shear-wave velocity inversion using Rayleigh-wave joint inversion (radial-radial and vertical-vertical components) at depths of 5 (*A*), 15 (*B*), 25 (*C*), 35 (*D*), and 45 (*E*) kilometers (km). Cross sections (*C*–*C*′ and *D*–*D*′) and harrat markers (yellow squares) also shown on figure 25 are displayed in part *A*. The yellow squares, listed northwest to southeast, represent Harrats Lunayyir, Rahat, and al Buqūm.

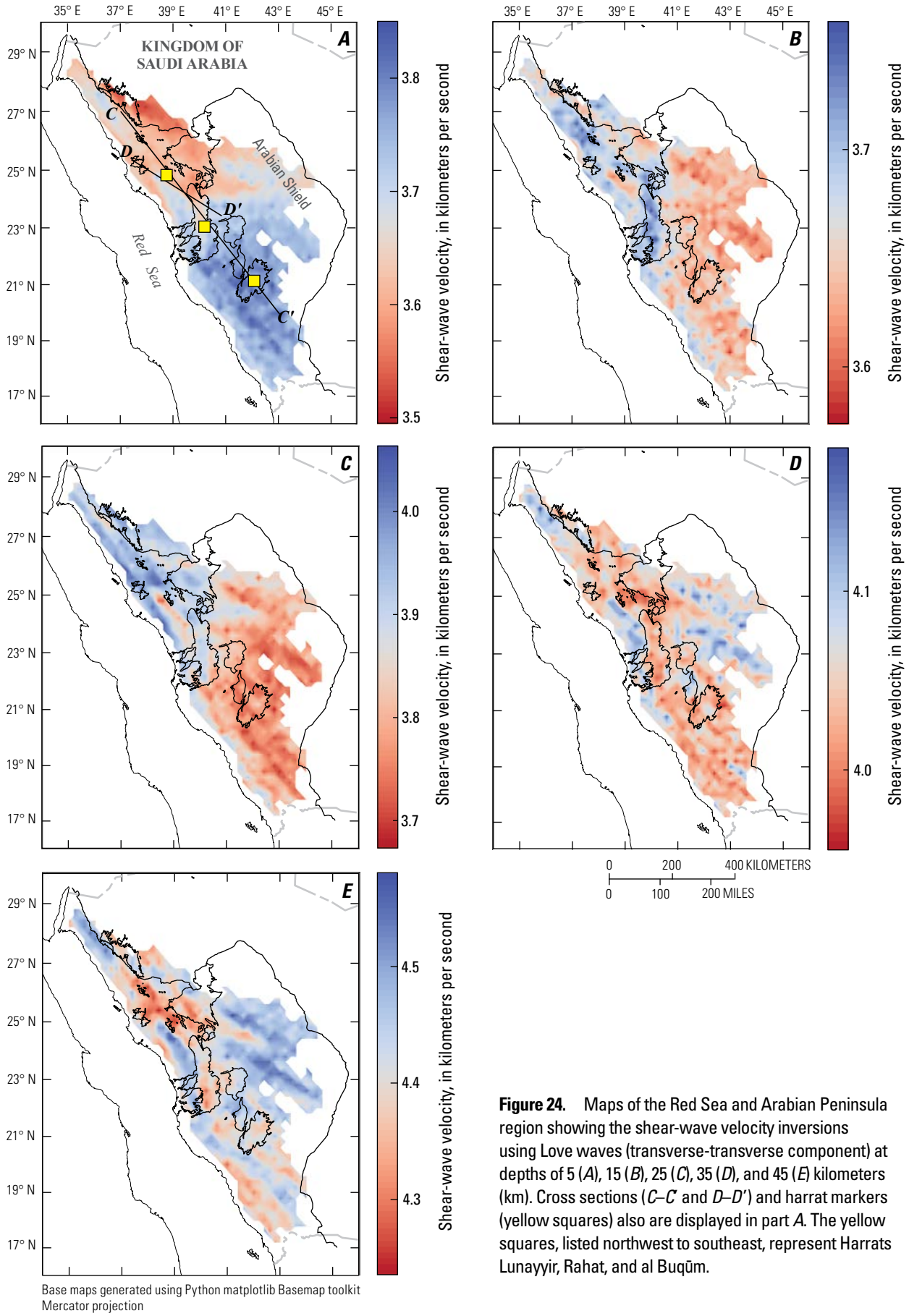

Figure 24. Maps of the Red Sea and Arabian Peninsula region showing the shear-wave velocity inversions using Love waves (transverse-transverse component) at depths of 5 (*A*), 15 (*B*), 25 (*C*), 35 (*D*), and 45 (*E*) kilometers (km). Cross sections (*C*–*C*′ and *D*–*D*′) and harrat markers (yellow squares) also are displayed in part *A*. The yellow squares, listed northwest to southeast, represent Harrats Lunayyir, Rahat, and al Buqūm.

Two cross sections of the Arabian Shield were made using the S-wave velocities inverted from Rayleigh and Love waves (fig. 25, fig. 4.6 of appendix 4). Cross section *C*–*C*′ trends approximately north to south, is parallel to the coast, and crosses between Harrats Lunayyir and Khaybar through to Harrat al Buqūm, and *D*–*D*′ trends northwest to southeast from Harrat Lunayyir through northern Harrat Rahat (fig. 23*A*). To facilitate interpretation, three markers (yellow squares) are shown across the cross sections: one between Harrats Lunayyir and Khaybar (labeled as Harrat Lunayyir on fig. 25), one in middle of Harrat Rahat, and the last at Harrat al Buqūm.

The top 20 km of the Rayleigh S-wave inversion primarily contain velocities of 3.6–3.8 km/s and increases to 4.3 km/s at 20–40 km depth (fig. 25). Our results do not resolve any low-velocity zones associated with the harrats for either the *C*–*C*′ or the *D*–*D*′ shear-wave velocity cross sections from Rayleigh waves. The shear-wave velocities from the Love-wave inversion are similar to the Rayleigh-wave inversion: both inversions show S-wave velocities of 3.6–3.8 km/s for the top 20 km and 3.9–4.5 km/s at greater depths (fig. 25, fig. 4.6 of appendix 4). However, low velocities are observed in cross section *D*–*D*′ in the area between Harrats Lunayyir and Khaybar (left yellow marker on fig. 4.6*B* of appendix 4).

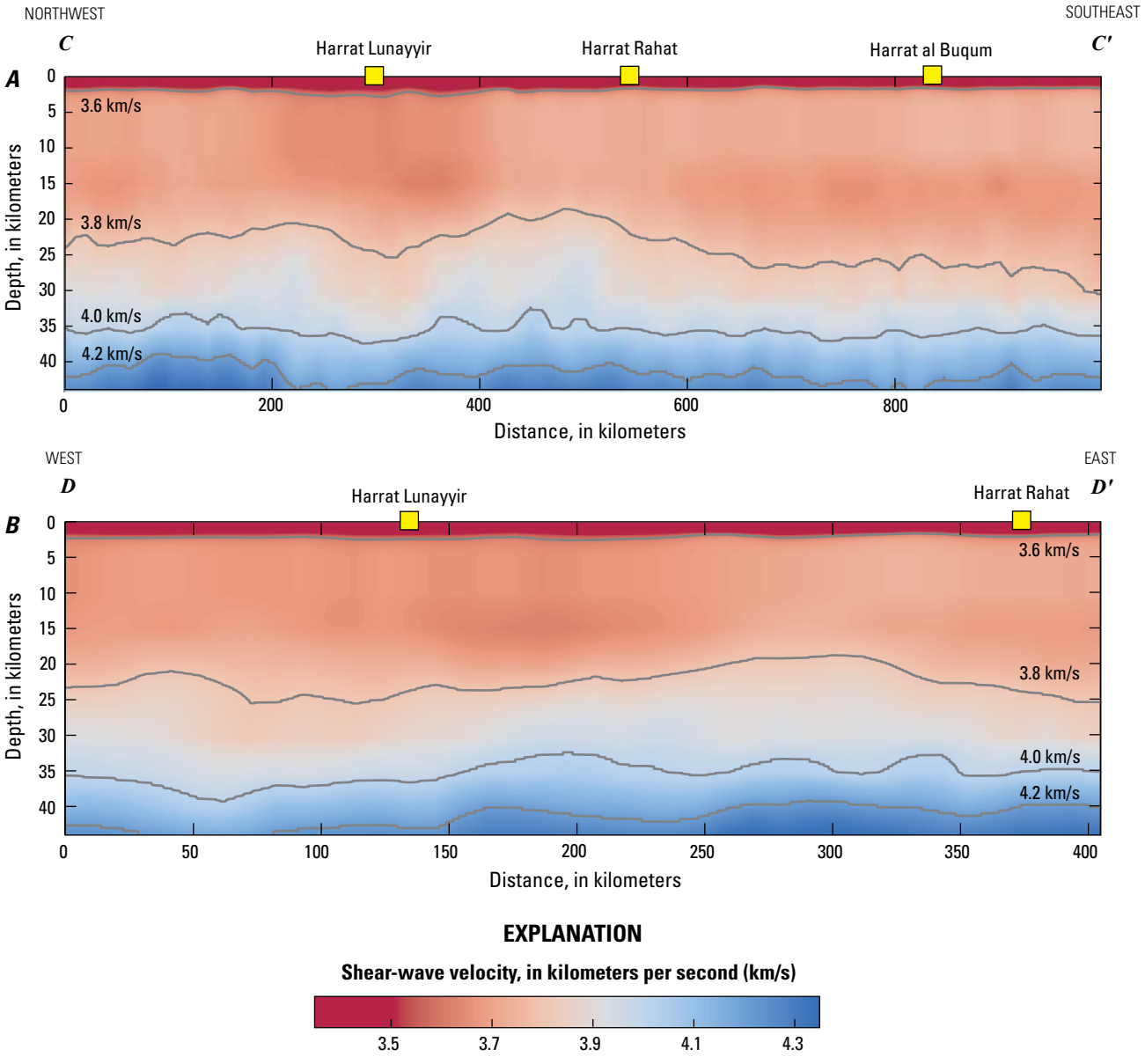

Figure 25. Cross sections *C*–*C*′ (*A*) and *D*–*D*′ (*B*) showing shear-wave velocity from a joint inversion of Rayleigh waves. Yellow squares indicate harrat markers shown on figure 23*A*, and cross section locations are shown on figures 23*A* and 24*A*.

Shear-wave velocities can be compared at different depths with global average measurements for shields and platforms (Christensen and Mooney, 1995). The velocity changes observed in the Arabian Shield are within the typical range of crustal models (table 2) when a V_P/V_S ratio of 1.73 for the upper crust and 1.77 for the lower crust (Chulick and others, 2013) is used. This agreement of data indicates that the observed velocity changes could reflect lithological variation within the shield.

Table 2. Mean shear-wave velocity and deviation from mean velocities for figure 25.

[Shear-wave velocities (V_S) were converted to compressional-wave velocity (V_P) using V_P/V_S ratios of 1.73 and 1.77 for the upper and lower crust, respectively (Chulick and others, 2013), and compared to mean crustal V_P velocities for shields and platforms (Christensen and Mooney, 1995). km, kilometer; km/s, kilometer per second]

Depth (km)	V_S (km/s)[1]	V_P (km/s)[1]	V_P (km/s)[2]
5	3.68±0.12	6.37±0.21	5.68±0.81
15	3.67±0.11	6.35±0.19	6.32±0.26
25	3.80±0.15	6.70±0.27	6.65±0.27
35	3.97±0.11	7.03±0.19	6.95±0.30

[1]Values are from this study using V_P/V_S ratios of 1.73 and 1.77.

[2]Values are from Christensen and Mooney (1995).

Summary and Future Work

Northern Harrat Rahat Conclusions

We used ambient seismic noise tomography to obtain S-wave velocity measurements for the top 30 km of the crust beneath northern Harrat Rahat, the largest Cenozoic volcanic field in Saudi Arabia. The primary geologic features in the study area are the basaltic volcanic rocks of the harrat that are underlain and surrounded by Precambrian rocks of the Arabian Shield (fig. 2).

Rayleigh-wave and Love-wave dispersion maps were computed for periods of 5–12 seconds and were used to show high- and low-velocity perturbations of ±3–8 percent throughout the study area. A low-velocity feature coincides with low-gravity measurements (Langenheim and others, 2019, 2023) (fig. 2) and was observed in the Love-wave dispersion maps extending northward from the 1256 C.E. eruption area to beyond the region covered by Cenozoic volcanic rocks (fig. 7*A*). This feature was most apparent at the 5-second period (fig. 7*A*) but was not observed in the Rayleigh-wave dispersion maps (fig. 6*A*), which indicates a shallow origin where the Rayleigh waves do not have good depth resolution (fig. 3).

Two- to five-layer 1D inversions (table 1.3 of appendix 1) were done for Rayleigh- and Love-wave phase velocities at each node of the dispersion maps using a neighborhood algorithm code (Wathelet and others, 2004). The L4 inversion yielded the best fit with fewest parameters. The 1D velocity models were interpolated into a pseudo-3D volume, and cross sections were taken east to west across the 1256 C.E. eruption (*A*–*A*′) and north to south along the low-velocity anisotropic feature (*B*–*B*′). The feature could not be modeled using the neighborhood algorithm inversion, most likely owing to its proximity to the surface.

A shear-wave velocity increase (3.5–3.6 km/s to 4.0–4.1 km/s) was observed across the depth interval of approximately 15 to 25 km using both Rayleigh and Love waves (figs. 8, 11, 12). This velocity increase corresponds to the transition between the felsic upper crust and the mafic lower crust (Mooney and others, 1985; Stern and Johnson, 2010). The average velocities at 5 and 25 km depth, 3.64 and 3.95 km/s for the Rayleigh-wave inversion and 3.53 and 4.16 km/s for the Love-wave inversion (table 1), are consistent with findings from other tomographic studies (Mokhtar and others, 2001; Park and others, 2008; Tang and others, 2016). We do not find a significant reduction or increase in the S-wave velocity within the crust and conclude that a magma chamber is not likely to be present unless it is deeper than 30 km, has a spatial extent shorter than 15 km, or is shallower than 5 km depth with a small velocity contrast. The third possibility is discounted by the absence of surface geothermal features, hydrothermally altered rocks, and a lack of abundant seismicity that characteristically surrounds and overlies known shallow magma reservoirs.

Saudi Arabian Shield Conclusions

Seismic ambient noise tomography was applied to the entire Arabian Shield to determine its S-wave crustal structure. As previously noted, the maximum surface- and S-wave velocity deviations from the mean were approximately ±3 percent, which are similar to the measured S-wave velocity deviations for the Harrat Rahat subset (see the "1D Shear-Velocity Inversions" section).

Several mechanisms could induce the observed ±3 percent velocity deviation. Shear-wave velocity changes that are due to subsurface magma are typically on the order of 10 percent or greater (Stachnik and others, 2008; Flinders and others, 2018), which indicates that no magma reservoirs of appreciable size are present in the crust. The wavelength of seismic data increases with period, meaning that widely separated seismograph pairs, which are sensitive to long periods, will produce wavelengths on the order of tens of kilometers (for example, a 20-second period at 3 km/s produces wavelengths of approximately 60 km). Owing to this fact, a subsurface magma chamber could be present with a smaller dimension than our shortest seismic wavelength (about 15 km) but would go undetected.

We observed a 10 km/s signal in the RR and ZZ moveouts that likely corresponds to the arrival of teleseismic P-waves generated by distant storms in deep oceans (Gerstoft and others, 2008; Landés and others, 2010) or Mohorovičić discontinuity reflections (Zhan and others, 2010; Poli and others, 2012). We hypothesize that the prevalence of this signal in the Rayleigh-wave cross correlations is due to the

low seismic attenuation of the crystalline Precambrian rocks of the Arabian Shield. A subsequent study may be able to use this signal to supplement traditional surface-wave tomography for this region.

Acknowledgments

We thank the Saudi Geological Survey for providing the data used in this analysis and the funding to work on this project (Grant G17AC00083). We are grateful to Victoria University of Wellington and the U.S. Geological Survey for establishing a cooperative agreement that made this research possible. Comments from Vicki Langenheim, Zheng Tang, Michael Ritzwoller, Misha Barmin, Alex Blanchette, James Hammond, Rufus Catchings, Gary Chulick and an anonymous reviewer greatly improved this manuscript. We gratefully acknowledge the use of computer software from the University of Colorado downloaded from http://ciei.colorado.edu/Products/.

References Cited

Abdelwahed, M.F., El-Masry, N., Moufti, M.R., Kenedi, C.L., Zhao, D., Zahran, H., and Shawali, J., 2016, Imaging of magma intrusions beneath Harrat Al-Madinah in Saudi Arabia. Journal of Asian Earth Sciences, v. 120, p. 17–28, https://doi.org/10.1016/j.jseaes.2016.01.023.

Al-Saad, D., Sawaf, T., Gebran, A., Barazangi, M., Best, J., and Chaimov, T., 1992, Crustal structure of central Syria; The intracontinental Palmyride Moutain belt: Tectonophysics, v. 207, p. 345–358.

Aoki, Y., Takeo, M., Aoyama, H., Fujimatsu, J., Matsumoto, S., Miyamachi, H., Nakamichi, H., Ohkura, T., Ohminato, T., Oikawa, J., Tanada, R., Tsutsui, T., Yamamoto, K., Yamamoto, M., Yamasato, H., and Yamawaki, T., 2009, P-wave velocity structure beneath Asama Volcano, Japan, inferred from active source seismic experiment: Journal of Volcanology and Geothermal Research, v. 187, p. 272–277, https://doi.org/10.1016/j.jvolgeores.2009.09.004.

Baer, G., and Hamiel, Y., 2010, Form and growth of an embryonic continental rift—InSAR observations and modelling of the 2009 western Arabia rifting episode: Geophysical Journal International, v. 182, p. 155–167, https://doi.org/10.1111/j.1365-246X.2010.04627.x.

Barmin, M.P., Ritzwoller, M.H., and Levshin, A.L., 2001, A fast and reliable method for surface wave tomography: Pure and Applied Geophysics, v. 158, p. 1351–1375, https://doi.org/10.1007/PL00001225.

Bedrosian, P., Peacock, J., Dhary, M., Shareef, A., Feucht, D., and Zahran, H., 2019, Crustal magmatism and anisotropy beneath the Arabian Shield—A cautionary tale: Journal of Geophysical Research, v. 124, p. 10153–10179, https://doi.org/10.1029/2019JB017903.

Behr, Y., 2010, Imaging New Zealand's crustal structure using ambient seismic noise recordings from permanent and temporary instruments: Wellington, New Zealand, Victoria University of Wellington, Ph.D. dissertation, 196 p.

Behr, Y., Townend, J., Bannister, S., and Savage, M.K., 2011, Crustal shear wave tomography of the Taupo Volcanic Zone, New Zealand, via ambient noise correlation between multiple three-component networks: Geochemistry, Geophysics, Geosystems, v.12, no. 3, 18 p., https://doi.org/10.1029/2010GC003385.

Bensen, G.D., Ritzwoller, M.H., Barmin, M.P, Levshin, A.L., Lin, F., Moschetti, M.P., Shapiro, N.M., and Yang, Y., 2007, Processing seismic ambient noise data to obtain reliable broad-band surface wave dispersion measurements: Geophysics Journal International, v. 169, p. 1239–1260, https://doi.org/10.1111/j.1365-246X.2007.03374.x.

Bird, P., 2002, An updated digital model of plate boundaries: Geochemistry, Geophysics, Geosystems, v. 4, no. 3, 52 p., https://doi.org/10.1029/2001GC000252.

Blank, H.R., and Sadek, H.S., 1983, Spectral analysis of the 1976 aeromagnetic survey of Harrat Rahat, Kingdom of Saudi Arabia: U.S. Geological Survey Open-File Report 83–640, 32 p., 2 plates, scales 1:500,000 and 1:250,000.

Bonnefoy-Claudet, S., Cotton, F., and Bard, P., 2006, The nature of noise wave field and its application for site effects studies—A literature review: Earth-Science Reviews, v. 79, p. 205–227, https://doi.org/10.1016/j.earscirev.2006.07.004.

Brenguier, F., Shapiro, N.M., Campillo, M., and Nercessian, A., 2007, 3-D surface wave tomography of the Piton de la Fournaise volcano using seismic noise correlations: Geophysical Research Letters, v. 34, no. 2., 5 p., https://doi.org/10.1029/2006GL028586.

Brew, G., Barazangi, M., Al-Maleh, A., and Sawaf, T., 2001, Tectonic and geologic evolution of Syria: GeoArabia, v. 6, no. 4, p. 573–616.

Camp, V.E., Hooper, P.R., Roobol, M.J., and White, D.L., 1987, The Madinah eruption, Saudi Arabia—Magma mixing and simultaneous extrusion of three basaltic chemical types: Bulletin of Volcanology, v. 49, p. 489–508.

Camp, V.E., and Roobol, M.J., 1989, The Arabian continental alkali basalt province—Part I, evolution of Harrat Rahat, Kingdom of Saudi Arabia: Geological Society of America Bulletin, v. 101, p. 71–95.

Camp, V.E., and Roobol, M.J., 1991, Geologic map of the Cenozoic lava field of Harrat Rahat, Kingdom of Saudi Arabia: Saudia Arabian Deputy Ministry for Mineral Resources, Geosciences Map GM-123, scale 1:125,000, 37 p.

Camp, V.E., and Roobol, M.J., 1992, Upwelling asthenosphere beneath western Arabia and its regional implications: Journal of Geophysical Research Solid Earth, v. 97, no. B11, p. 15255–15271, https://doi.org/10.1029/92JB00943.

Chang, S.J., Merino, M., der Lee, S.V., Stein, S., and Stein, C.A., 2011, Mantle flow beneath Arabia offset from the opening of the Red Sea: Geophysical Research Letters, v. 38, no. 4, p. 448–454, https://doi.org/10.1029/2010GL045852.

Christensen, N.I., 1996, Poisson's ratio and crustal seismology: Journal of Geophysical Research, v. 101, no. B2, p. 3139–3156, https://doi.org/10.1029/95JB03446.

Christensen, N.I., and Mooney, W.D., 1995, Seismic velocity structure and composition of the continental crust—A global view: Journal of Geophysical Research, v. 100, no. B6, p. 9761–9788, https://doi.org/10.1029/95JB00259.

Chulick, G., Detweiler, S., and Mooney, W.D., 2013, Seismic structure of the uppermost mantle of South America and surrounding oceanic basins: Journal of South American Earth Sciences, v. 42, p. 260–276, https://doi.org/10.1016/j.jsames.2012.06.002.

Civilini, F., 2018, Determining seismic shear-velocity from ambient noise sources at regional and local scales: Wellington, New Zealand, Victoria University of Wellington, Ph.D. dissertation, 313 p.

Coleman, R., Gregory, R., and Brown, G., 1983, Cenozoic volcanic rocks of Saudi Arabia: U.S. Geological Survey Open-File Report 83-788, 86 p.

Dietterich, H.R., Downs, D.T., and Stelten, M.E., 2023, Lava flow emplacement in Harrat Rahat with implications for eruptions in mafic volcanic fields, chap. E *of* Sisson, T.W., Calvert, A.T., and Mooney, W.D., eds., Active volcanism on the Arabian Shield—Geology, volcanology, and geophysics of northern Harrat Rahat and vicinity, Kingdom of Saudi Arabia: U.S. Geological Survey Professional Paper 1862 [also released as Saudi Geological Survey Special Report SGS–SP–2021–1], 49 p., https://doi.org/10.3133/pp1862E.

Dietterich, H.R., Downs, D.T., Stelten, M.E., and Zahran, H., 2018, Reconstructing lava flow emplacement histories with rheological and morphological analysis—The Harrat Rahat volcanic field, Kingdom of Saudi Arabia: Bulletin of Volcanology, v. 80, https://doi.org/10.1007/s00445-018-1259-4.

Downs, D.T., Robinson, J.E., Stelten, M.E., Champion, D.E., Dietterich, H.R., Sisson, T.W., Zahran, H., Hassan, K., and Shawali, J., 2019, Geologic map of the northern Harrat Rahat volcanic field, Kingdom of Saudi Arabia: U.S. Geological Survey Scientific Investigations Map 3428 [also released as Saudi Geological Survey Special Report SGS–SP–2019–2], 65 p., 4 sheets, scales 1:75,000, 1:25,000, https://doi.org/10.3133/sim3428.

Flinders, A.F., Shelly, D.R., Dawson, P.B., Hill, D.P., Tripoli, B., and Shen, Y., 2018, Seismic evidence for significant melt beneath the Long Valley Caldera, California, USA: Geology, v. 46, no. 9, p. 799–802, https://doi.org/10.1130/G45094.1.

Friedrich, A., Krüger, F., and Klinge, K., 1998, Ocean-generated microseismic noise located with the Gräfenberg array: Journal of Seismology, v. 2, p. 47–64.

Gerstoft, P., Shearer, P.M., Harmon, N., and Zhang, J., 2008, Global P, PP, and PKP wave microseisms observed from distant storms: Geophysical Research Letters, v. 35, no. 23, 6. p., https://doi.org/10.1029/2008GL036111.

Guidarelli, M., Stuart, G., Hammond, J., Kendall, J., Ayele, A., and Belachew, M., 2011, Surface wave tomography across Afar, Ethiopia—Crustal structure at a rift triple-junction: Geophysical Research Letters, v. 38, no. 24, 6 p., https://doi.org/10.1029/2011GL046840.

Hammond, J., and Kendall, J.M., 2016, Constraints on melt distribution from seismology; a case study in Ethiopia, *in* Writ, T.J., Ayele, A., Ferguson, D.J., Kidane, T., and Vye-Brown, C., eds., Magmatic rifting and active volcanism: The Geological Society of London Special Publications, v. 420, p. 127–147, https://doi.org/10.1144/SP420.14.

Jaxybulatov, K., Shapiro, N., Koulakov, I., Mordret, A., Landès, M., and Sens-Schönfelder, C., 2014, A large magmatic sill complex beneath the Toba caldera: Science, v. 346, no. 6209, p. 617–619, https://doi.org/10.1126/science.1258582.

Johnson, P.R., and Kattan, F.H., 2012, The Geology of the Saudi Arabian Shield: Saudi Geological Survey, 479 p.

Jones, T., 1980, Effects of temperature and saturation on the velocity and attenuation of seismic waves in rocks—Applications to geothermal reservoir evaluation, *in* Ramey, H.J., Jr., and Kruger, P., eds., Sixth workshop on geothermal reservoir engineering, December 16–18: Stanford University, Palo Alto, Calif., p. 328–337.

Landés, M., Hubans, F., Shapiro, N.M., and Paul, A., 2010, Origin of deep ocean microseisms by using teleseismic body waves: Journal of Geophysical Research, v. 115, 14 p., https://doi.org/10.1029/2009JB006918.

Langenheim, V., Ritzinger, B., Zahran, H., Sharif, A., and Al-dahri, M., 2019, Crustal structure of the northern Harrat Rahat volcanic field (Saudi Arabia) from gravity and aeromagnetic data: Tectonophysics, v. 750, p. 9–21.

Langenheim, V.E., Ritzinger, B.T., Zahran, H.M., Shareef, A., and Al-Dhahry, M.K., 2023, Depth to basement and crustal structure of the northern Harrat Rahat volcanic field, Kingdom of Saudi Arabia, from gravity and aeromagnetic data, chap. K *of* Sisson, T.W., Calvert, A.T., and Mooney, W.D., eds., Active volcanism on the Arabian Shield—Geology, volcanology, and geophysics of northern Harrat Rahat and vicinity, Kingdom of Saudi Arabia: U.S. Geological Survey Professional Paper 1862 [also released as Saudi Geological Survey Special Report SGS–SP–2021–1], 18 p., https://doi.org/10.3133/pp1862K.

Lecocq, T., Caudron, C., and Brenguier, F., 2014, MSNoise, a Python package for monitoring seismic velocity changes using ambient seismic noise: Electronic Seismologist, v. 85, no. 3, p. 715–726, https://doi.org/10.1785/0220130073.

Levshin, A.L., 2013, Phase/group velocities sensitivity kernels: University of Colorado Boulder software, http://ciei.colorado.edu/Products/, accessed August 1, 2016.

Levshin, A.L., Pisarenko, V.F., and Pogrebinsky, G.A., 1972, On a frequency-time analysis of oscillations: Annuals of Geophysics, v. 28, p. 211–218.

Levshin, A.L., Yanovskaya, T.B., Lander, A.V., Bukchin, B.G., Barmin, M.P., Ratnikova, L.I., and Its, E.N., 1989, Seismic surface waves in a laterally inhomogeneous Earth: Kluwer Academic Publishers, 304 p.

McNamara, D.E., and Boaz, R.I., 2011, PQLX—A seismic data quality control system description, applications, and users manual: U.S. Geological Survey Open-File Report 2010-1292, 41 p.

Mokhtar, T.A., Shawali, J., Abdelwahed, M., Runge, M., and Kenedi, C., 2013, The 1999 microearthquake swarms of northern Harrat Rahat, *in* Volcanic Risks in Saudi Arabia (VORISA) Scientific Meeting, Jiddah, Kingdom of Saudia Arabia, November 17–18, 2013: Geological Hazards Research Center, King Abdulaziz University, p. 69–72.

Mokhtar, T.A., Ammon, C.J., Herrmann, R.B., and Ghalib, H.A.A., 2001, Surface wave velocities across Arabia: Pure and Applied Geophysics, v. 158, no. 8, p. 1425–1444, https://doi.org/10.1007/PL00001228.

Mooney, W.D., Holbrook, S., and Christensen, N., 1992, The seismic velocity structure of the deep continental crust: Developments of Geotectonics, v. 23, p. 1–43.

Mooney, W.D., Gettings, M.E., Blank, H.R., and Healy, J.H., 1985, Saudi Arabian seismic refraction profile—A traveltime interpretation of crustal and upper mantle structure: Tectonophysics, v. 111, p. 173–246.

Moufti, M.R., Matsah, M.I., Soliman, M.A., and Moghazi, A.M., 2011, Arabian plume dynamics beneath Al-Madinah Al-Munawwarah region and its related geohazards: Final project report (ARP-26-79) submitted to King Abdulaziz City for Science and Technology, Riyadh, Saudi Arabia. 382 p.

Moufti, M.R., Moghazi, A.M., and Ali, K.A., 2012a, $^{40}Ar/^{39}Ar$ geochronology of the Neogene-Quaternary Harrat Al-Madinah intercontinental volcanic field, Saudi Arabia—Implications for duration and migration of volcanic activity: Journal of Asian Earth Sciences, v. 62, p. 253–268, https://doi.org/10.1016/j.jseaes.2012.09.027.

Moufti, M.R., Moghazi, A.M., and Ali, K.A., 2012b, Geochemistry and Sr-Nd-Pb isotropic composition of the Harrat Al-Madinah volcanic field, Saudi Arabia: Gondwana Research, v. 21, no. 2–3, p. 670–689, https://doi.org/10.1016/j.gr.2011.06.003.

Moufti, M.R., and Nèmeth, K., 2016, Geologic setting, chap. 2 *of* Eder, W., Bobrowsky, P., and Martinez-Frías, J., eds., Geoheritage of volcanic Harrats in Saudi Arabia, Geoheritage, Geoparks, and Geotourism: Switzerland, Springer International Publishing, p.23–32, https://doi.org/10.1007/978-3-319-33015-0.

Nanometrics, 2009, Trillium 40 seismometer user guide: Ontario, Canada, Nanometrics Inc., 65 p.

Nishida, K., and Takagi, R., 2016, Teleseismic S-wave microseisms: Science, v. 353, no. 6302, p. 919–921, https://doi.org/10.1126/science.aaf7573.

Overduin, P.P., Haberland, C., Ryberg, T., Kneier, F., Jacobi, T., Grigoriev, M.N., and Ohrnberger, M., 2015, Submarine permafrost depth from ambient seismic noise: Geophysical Research Letters, v. 42, no. 18, p. 7581–7588, https://doi.org/10.1002/2015GL065409.

Pallister, J.S., McCausland, W.A., Jónsson, S., Lu, Z., Zahran, H.M., El Hadidy, S., Aburukbah, A., Stewart, I.C.F., Lundgren, P.R., White, R.A., and Moufti, M.R.H., 2010, Broad accommodation of rift-related extension recorded by dyke intrusion in Saudi Arabia: Nature Geoscience, v. 3, p. 705–712, https://doi.org/10.1038/ngeo966.

Park, Y., Nyblade, A.A., Rodgers, A.J., and Al-Amri, A., 2008, S wave velocity structure of the Arabian Shield upper mantle from Rayleigh wave tomography: Geochemistry, Geophysics, Geosystems, v. 9, no. 7, 15 p., https://doi.org/10.1029/2007GC001895.

Passcal, 2016, Nanometrics trillium 120 broadband sensor: A Passcal website, https://www.passcal.nmt.edu/content/instrumentation/sensors/broadband-sensors/t120-bb-sensor, accessed August 1, 2016.

Peacock, J.R., Bedrosian, P.A., Al-Dhahry, M.K., Shareef, A., Feucht, D.W., Taylor, C.D., Bloss, B., and Zahran, H.M., 2023, Magnetotelluric investigation of northern Harrat Rahat, Kingdom of Saudi Arabia, chap. L *of* Sisson, T.W., Calvert, A.T., and Mooney, W.D., eds., Active volcanism on the Arabian Shield—Geology, volcanology, and geophysics of northern Harrat Rahat and vicinity, Kingdom of Saudi Arabia: U.S. Geological Survey Professional Paper 1862 [also released as Saudi Geological Survey Special Report SGS–SP–2021–1], 111 p., https://doi.org/10.3133/pp1862L.

Pellaton, C., 1981, Geologic map of the Al Madinah quadrangle, sheet 24D, Kingdom of Saudi Arabia (with text): Saudi Arabian Deputy Ministry for Mineral Resources Geoscience Map GM-52, scale 1:250,000, 19 p.

Peterson, J., 1993, Observations and modelling of background seismic noise: U.S. Geological Survey Open-File Report 93-322, 94 p.

Poli, P., Pedersen, H.A., and Campillo, M., 2012, Emergence of body waves from cross-correlation of short period seismic noise: Geophysical Journal International, v. 188, no. 2, p. 549–558, https://doi.org/10.1111/j.1365-246X.2011.05271.x.

Pollastro, R., Karshbaum, A., and Viger, R., 1999, Maps showing geology, oil, and gas fields and geologic provinces of the Arabian Peninsula [version 2.0]: U.S. Geological Survey Open-File Report 97-470B, 14 p., https://doi.org/10.3133/ofr97470B.

Relinger, R., McClusky, S., and ArRajehi, A., 2015, Geodetic constraints on the geodynamic evolution of the Red Sea, *in* Rasul, N.M.A. and Stewart, I.C.F., eds., The Red Sea: Springer Earth System Sciences, 638 p.

Ritzwoller, M.H., 2013, AFTAN [automatic frequency-time analysis] of ambient noise cross-correlations: University of Colorado Boulder software release, http://ciei.colorado.edu/Products/.

Salters, V.J.M., Sachi-Kocher, A., Downs, D.T., Stelten, M.E., and Sisson, T.W., 2023, Isotopic and geochemical evidence for the source of volcanism at Harrat Rahat, Kingdom of Saudi Arabia, chap. J *of* Sisson, T.W., Calvert, A.T., and Mooney, W.D., eds., Active volcanism on the Arabian Shield—Geology, volcanology, and geophysics of northern Harrat Rahat and vicinity, Kingdom of Saudi Arabia: U.S. Geological Survey Professional Paper 1862 [also released as Saudi Geological Survey Special Report SGS–SP–2021–1], 30 p., https://doi.org/10.3133/pp1862J.

Sambridge, M., 1999, Geophysical inversion with a neighbourhood algorithm—I, Searching a parameter space: Geophysical Journal International, v. 138, p. 479–494, https://doi.org/10.1046/j.1365-246X.1999.00876.x.

Saygin, E., and Kennet, B.L.N., 2010, Ambient seismic noise tomography of Australian continent: Tectonophysics, v. 481, no. 1–4, p. 116–125, https://doi.org/10.1016/j.tecto.2008.11.013.

Shapiro, N.M., and Campillo, M., 2004, Emergence of broadband Rayleigh wave from correlations of the ambient seismic noise: Geophysical Research Letters, v. 31, no. 7, https://doi.org/10.1029/2004GL019491.

Shapiro, N.M., Campillo, M., Stehly, L., and Ritzwoller, M.H., 2005, High-resolution surface-wave tomography from ambient seismic noise: Science, v. 307, p. 1615–1618, https://doi.org/10.1126/science.1108339.

Sisson, T.W., Downs, D.T., Calvert, A.T., Dietterich, H.R., Mahood, G.A., Salters, V.J.M., Stelten, M.E., and Shawali, J., 2023, Mantle origin and crustal differentiation of basalts and hawaiites of northern Harrat Rahat, Kingdom of Saudi Arabia, chap. I *of* Sisson, T.W., Calvert, A.T., and Mooney, W.A., eds., Active volcanism on the Arabian Shield—Geology, volcanology, and geophysics of northern Harrat Rahat and vicinity, Kingdom of Saudi Arabia: U.S. Geological Survey Professional Paper 1862 [also released as Saudi Geological Survey Special Report SGS–SP–2021–1], 42 p., https://doi.org/10.3133/pp1862I.

Snieder, R., 2004, Extracting the Green's function from the correlation of coda waves—A derivation based on stationary phase: Physical Review E, v. 69, no. 4, article 046610, p. 1–8, https://doi.org/10.1103/PhysRevE.69.046610.

Stachnik, J.C., Dueker, K., Schutt, D.L., and Yuan, H., 2008, Imaging Yellowstone plume-lithosphere interactions from inversion of ballistic and diffusive Rayleigh wave dispersion and crustal thickness data: Geochemistry, Geophysics, Geosystems, v. 9, no. 6, https://doi.org/10.1029/2008GC001992.

Stankiewicz, J., Ryberg, T., Haberland, C., Fauzi, and Natawidjaja, D., 2010, Lake Toba volcano magma chamber imaged by ambient seismic noise tomography: Geophysical Research Letters, v. 37, no. 17, 5 p., https://doi.org/10.1029/2010GL044211.

Stern, R.J., and Johnson, P., 2010, Continental lithosphere of the Arabian Plate—A geologic, petrologic, and geophysical synthesis: Earth-Science Reviews, v. 101, p. 29–67, https://doi.org/10.1016/j.earscirev.2010.01.002.

Streckeisen, G., 1995, Portable very-broad-band tri-axial seismometer—STS-2 Low-Power [User manual; 2d edition]: Messgeraetem CH-8422 Pfungen, Switzerland, 58 p.

Tang, Z., Juli, J., Zahran, H., and Mai, P.M., 2016, The lithospheric shear-wave velocity structure of Saudi Arabia—Young volcanism in an old shield: Tectonophysics, v. 680, p. 8–27, https://doi.org/10.1016/j.tecto.2016.05.004.

Tang, Z., Mai, P.M., Chang, S.-J., and Zahran, H., 2018, Evidence for crustal low shear-wave speed in western Saudi Arabia from multi-scale fundamental-mode Rayleigh-wave group-velocity tomography: Earth and Planetary Science Letters, v. 495, p. 24–37, https://doi.org/10.1016/j.epsl.2018.05.011.

Tang, Z., Mai, P.M., Julià, J., and Zahran, H., 2019, Shear velocity structure beneath Saudi Arabia from the joint inversion of P and S wave receiver functions, and Rayleigh wave group velocity dispersion data: Journal of Geophysical Research; Solid Earth, v. 124, p. 4767–4787, https://doi.org/10.1029/2018JB017131.

Townsend, B., 2014, Symmetric triaxial seismometers, *in* Beer, M., Kougioumtzoglou, I., Patelli, E., and Au, I.K., eds., Encyclopedia of Earthquake Engineering: Berlin, Germany, Springer, p. 1–19, https://doi.org/10.1007/978-3-642-36197-5_194-1.

Tsai, V.C., 2009, On establishing the accuracy of noise tomography travel-time measurements in a realistic medium: Geophysical Journal International, v. 178, no. 3, p. 1555–1564, https://doi.org/10.1111/j.1365-246X.2009.04239.x.

Tsai, V.C., 2010, The relationship between noise correlation and the Green's function in the presence of degeneracy and the absence of equipartition: Geophysical Journal International, v. 182, no. 3, p. 1509–1514, https://doi.org/10.1111/j.1365-246X.2010.04693.x.

Uieda, L., Oliveira, V.C., Jr., and Barbosa, V.C.F., 2013, Modeling the earth with Fatiando a Terra, *in* Proceedings of the 12th Python in Science Conference, Austin, Texas, June 24–29: SciPy, p. 91–98.

Wathelet, M., 2005, Array recordings of ambient vibrations—Surface wave inversion: Liège, Belgium, Université de Liège, Ph.D. dissertation, 169 p., 95 figs., 20 tables.

Wathelet, M., 2008, An improved neighborhood algorithm; Parameter conditions and dynamic scaling: Geophysical Research Letters, v. 35, no. 9, article L09301, 5 p., https://doi.org/10.1029/2008GL033256.

Wathelet, M., Jongmans, D., and Ohrnberger, M., 2004, Surface-wave inversion using a direct search algorithm and its application to ambient vibration measurements: Near Surface Geophysics, v. 2, p. 211–221.

Wilson, C.J.N., Houghton, B.F., McWilliams, M.O, Lanphere, M.A., Weaver, S.D., and Briggs, R.M., 1995, Volcanic and structural evolution of Taupo Volcanic Zone, New Zealand—A review: Journal of Volcanology and Geothermal Research, v. 68, p. 1–28.

Yao, Z., Mooney, W., Zahran, H., and Youssef, S.E.-H, 2017, Upper mantle velocity structure beneath the Arabian shield from Rayleigh surface wave tomography and its implications: Journal of Geophysical Research Solid Earth, v. 122, p. 6552–6568, https://doi.org/10.1002/2016JB013805.

Youssef, S., 2015, Seismicity and seismotectonic setting of the Red Sea and adjacent areas, *in* Rasul, N.M.A, and Stewart, I.C.F., eds., The Red Sea; the formation, morphology, oceanography, and environment of a young ocean basin: Berlin, Germany, Springer, p. 151–159, https://doi.org/10.1007/978-3-662-45201-1_8.

Zhan, Z., Ni, S., Helmberger, D.V., and Clayton, R.W., 2010, Retrieval of Moho-reflected shear-wave arrivals from ambient seismic noise: Geophysical Journal International, v. 102, p. 408–420, https://doi.org/10.1111/j.1365-246X.2010.04625.x

Appendixes

Appendix 1. Harrat Rahat Seismic Ambient Noise Study Additional Tables

Table 1.1. Cross-correlation processing parameters.

[s, second; Hz, hertz]

Duration (s) of time series analyzed	Cross-correlation sample-rate (Hz)	Correlation duration (s)	Maximum lag-time (s)	Filtering (Hz)	Whitening (Hz)	Time normalization type (s)
86,400	20	1,800	700	0.005–1.1	0.006–1.0	One-bit

Table 1.2. Automatic frequency-time analysis processing parameters.

[km/s, kilometer per second; s, second; FTAN, frequency-time analysis; Db, decibel]

Parameter	Description	Value (Units)
piover4	Factor for pi/4 phase shift	−1.0
vmin	Minimum group velocity value	1.5 (km/s)
vmax	Maximum group velocity value	5.0 (km/s)
tmin	Minimum period	4.0 (s)
tmax	Maximum period	30.0 (s)
tresh	Threshold for second derivative of group velocity	10.0
ffact	Factor to width of FTAN filters	1.0
taperl	Factor for the left end seismogram tapering	1.0
snr	Minimum signal-to-noise ratio	0.2 (Db)
fmatch	Factor to compressed signal width	1.0

Table 1.3. Inversion parameter ranges used in the Dinver software (Wathelet and others, 2004; Wathelet, 2008).

[Models L4 and L5 allow for low-velocity zones. km/s, kilometer per second; km, kilometer; g/cm^3, gram per cubic centimeter, —, not applicable]

Layer	Velocity (km/s)	Interface depth (km)	Density (g/cm^3)
Model L2			
Layer 1	0.150–5.0	15.0–25.0	2.67–2.73
Halfspace	2.0–5.0	—	2.86–2.92
Model L3			
Layer 1	0.15–5.0	0.1–5.0	2.67–2.73
Layer 2	1.0–5.0	15.0–25.0	2.67–2.73
Halfspace	2.0–5.0	—	2.86–2.92
Model L4			
Layer 1	0.15–5.0	0.1–5.0	2.67–2.73
Layer 2	1.0–5.0	1.0–20.0	2.67–2.73
Layer 3	1.0–5.0	15.0–25.0	2.67–2.73
Halfspace	2.0–5.0	—	2.86–2.92
Model L5			
Layer 1	0.150–5.0	0.1–5.0	2.67–2.73
Layer 2	1.0–5.0	1.0–20.0	2.67–2.73
Layer 3	1.0–5.0	1.0–20.0	2.67–2.73
Layer 4	1.0–5.0	15.0–25.0	2.67–2.73
Halfspace	2.0–5.0	—	2.86–2.92

Appendix 2. Harrat Rahat Additional Figures

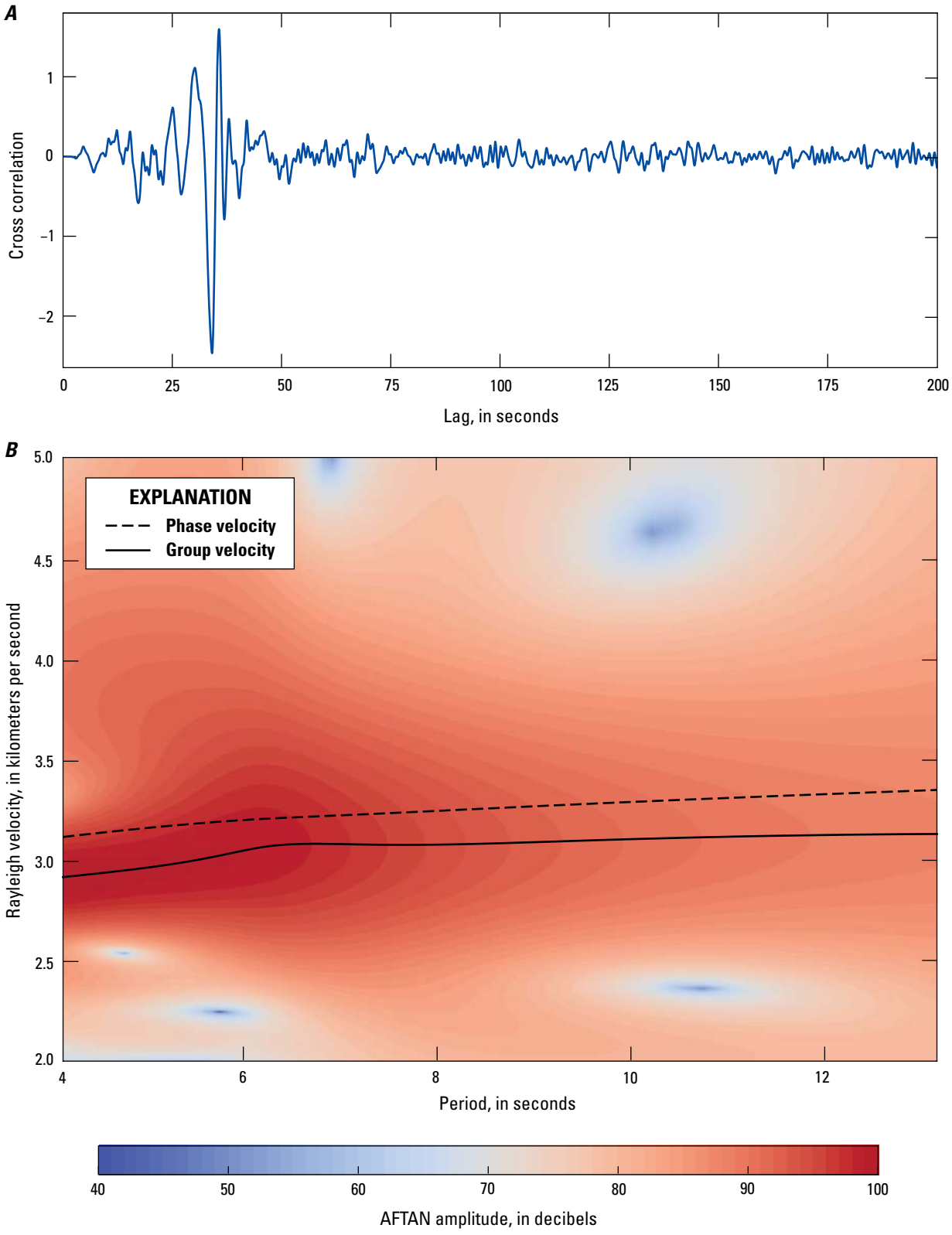

Figure 2.1. Graphs showing cross correlation between stations RHT03 and RHT06 radial-radial (RR) components (*A*) and the group and phase velocities (*B*) obtained by the automatic frequency-time analysis (AFTAN) procedure (Ritzwoller, 2013) for seismic station pair RHT03 and RHT07. The positive and negative sides of the cross correlations were stacked to increase signal-to-noise ratio.

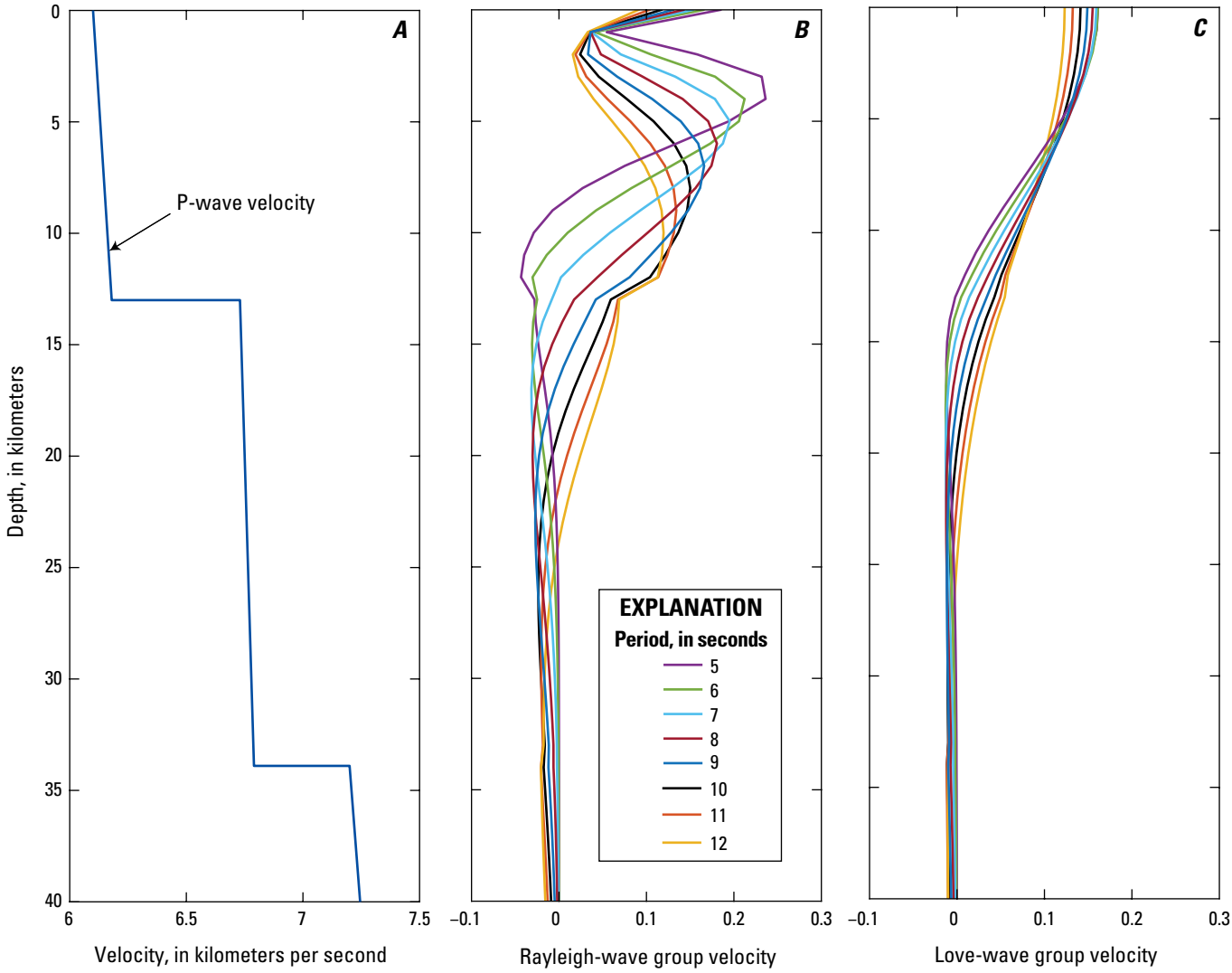

Figure 2.2. Graphs showing the P-wave model (*A*), the Rayleigh-wave (*B*), and Love-wave (*C*) group velocity sensitivity kernels computed for the northeast segment of shot point 4 from Mooney and others (1985).

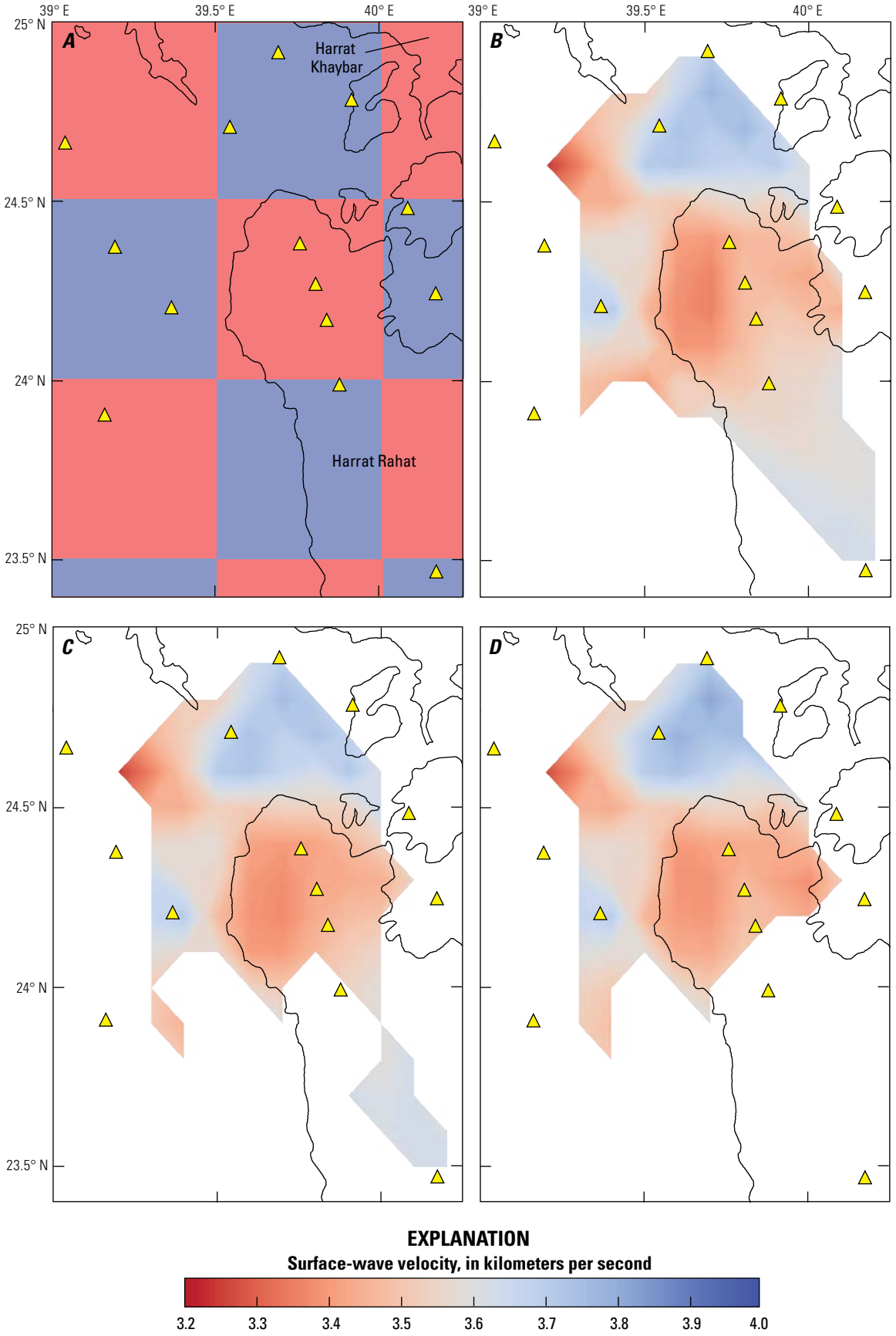

Figure 2.3. Maps of the northern Harrat Rahat area overlayed by a checkerboard model (*A*) and surface-wave velocities, in kilometers per second (km/s), for 0.5° cells (3.0 and 3.5 km/s) for group-velocity paths of radial-radial (RR; 55 station paths) (*B*), transverse-transverse (TT; 44 station paths) (*C*), and vertical-vertical (ZZ; 40 station paths) (*D*) components. Figures 1 and 13 in the main text show the name and positions of harrats (outlined in black) near Harrat Rahat on the Arabian Shield. Seismic stations are marked as yellow triangles and the borders of nearby harrats are displayed as black lines.

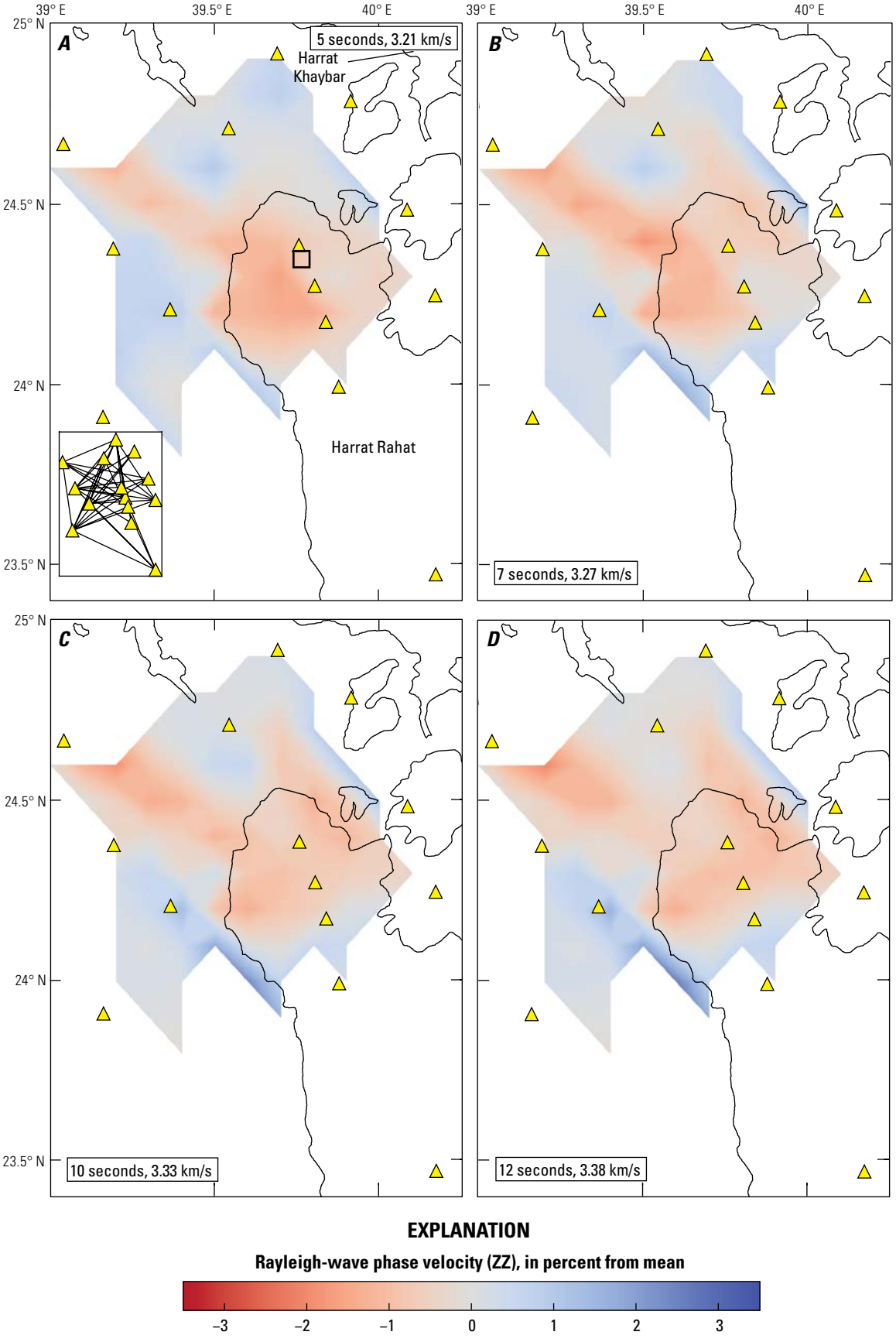

Figure 2.4. Maps of the northern Harrat Rahat area showing Rayleigh-wave phase velocity as a percentage difference from the mean velocity using vertical-vertical (ZZ) cross correlations (38 station paths) for 5-second (*A*), 7-second (*B*), 10-second (*C*), and 12-second (*D*) periods. Harrat Rahat seismic stations are marked as yellow triangles, and the borders of nearby harrats are shown as black lines. The location of the 1256 C.E. Al Madīnah eruption vents is displayed as a black box in part *A*. The length of period and mean velocity, in kilometers per second (km/s), for each subplot are displayed in an inset, and station paths are displayed in an inset in the lower left corner of part *A*. Figures 1 and 13 in the main text show the name and positions of harrats (outlined in black) near Harrat Rahat on the Arabian Shield.

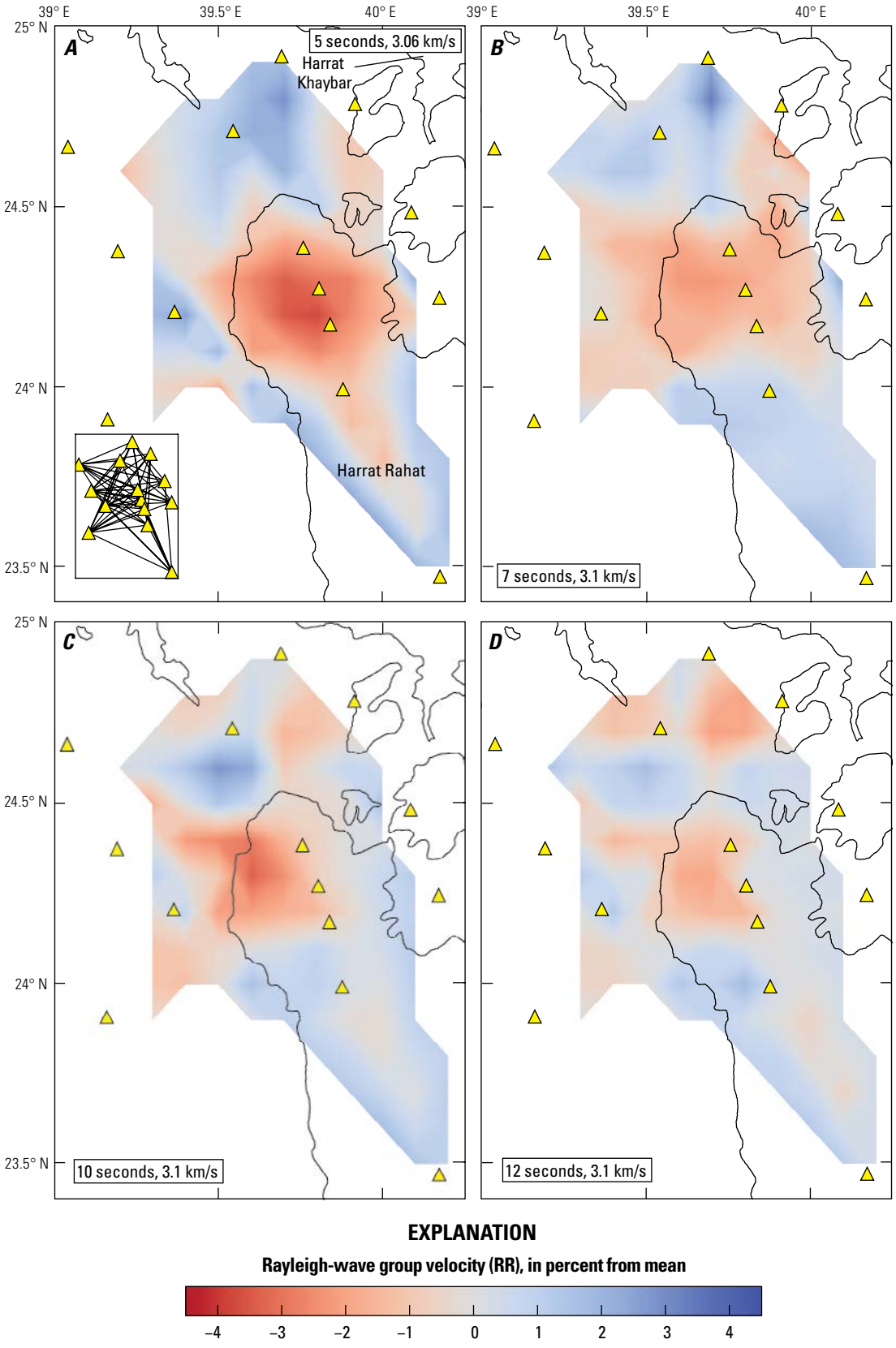

Figure 2.5. Maps of the northern Harrat Rahat area showing Rayleigh-wave group velocity as a percentage difference from the mean velocity using radial-radial (RR) cross correlations (55 station paths) for 5-second (*A*), 7-second (*B*), 10-second (*C*), and 12-second (*D*) periods. Harrat Rahat seismic stations are marked as yellow triangles, and the borders of nearby harrats are shown as black lines. The length of period and mean velocity, in kilometers per second (km/s), for each subplot are displayed in an inset, and station paths are displayed in an inset in the lower left corner of part *A*. Figures 1 and 13 in the main text show the name and positions of harrats (outlined in black) near Harrat Rahat on the Arabian Shield.

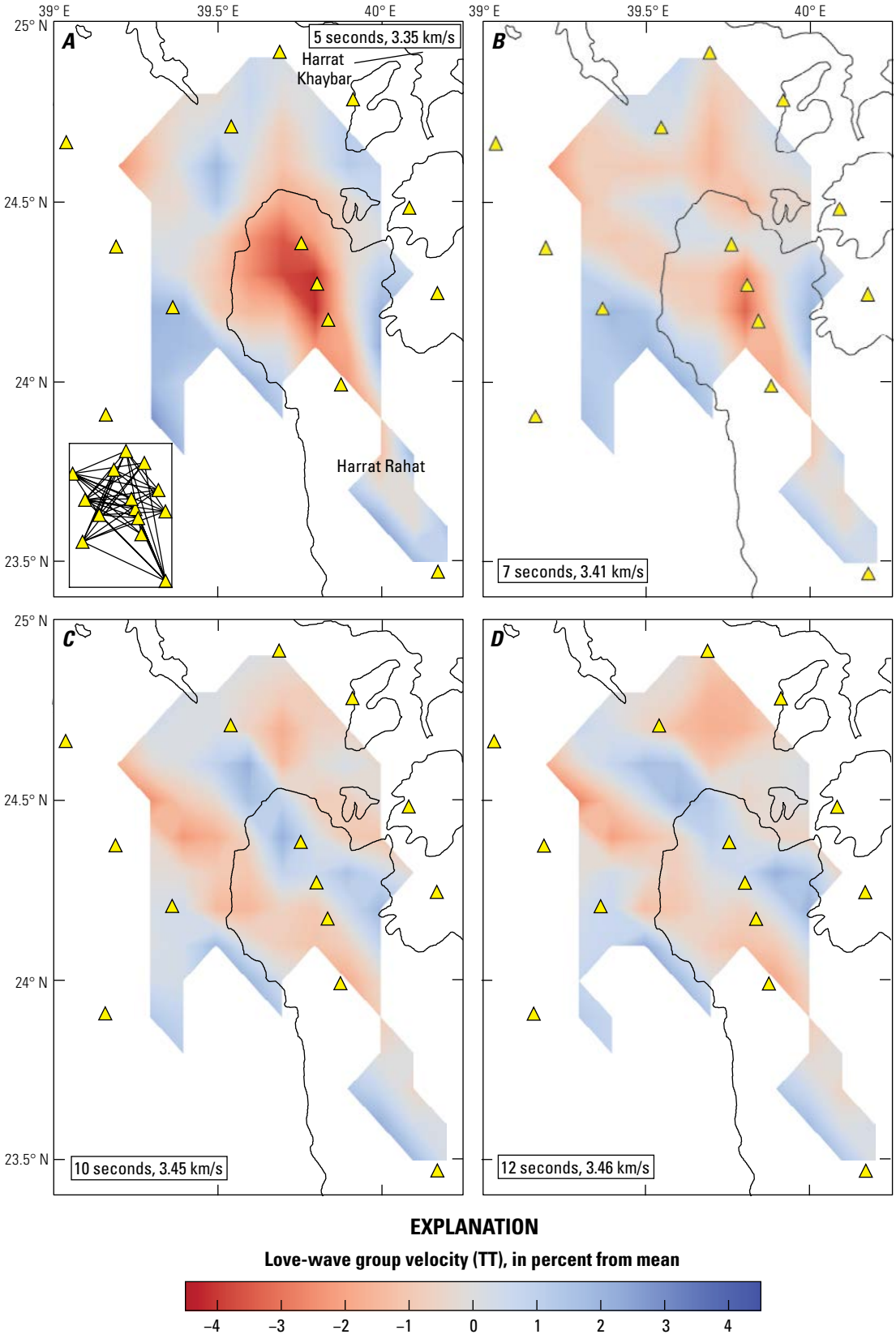

Figure 2.6. Maps of the northern Harrat Rahat area showing Love-wave group velocity as a percentage difference from the mean velocity using transverse-transverse (TT) cross correlations (44 station paths) for 5-second (*A*), 7-second (*B*), 10-second (*C*), and 12-second (*D*) periods. Harrat Rahat seismic stations are marked as yellow triangles, and the borders of nearby harrats are shown as black lines. The length of period and mean velocity, in kilometers per second (km/s), for each subplot are displayed in an inset, and station paths are displayed in an inset in the lower left corner of part *A*. Figures 1 and 13 in the main text show the name and positions of harrats (outlined in black) near Harrat Rahat on the Arabian Shield.

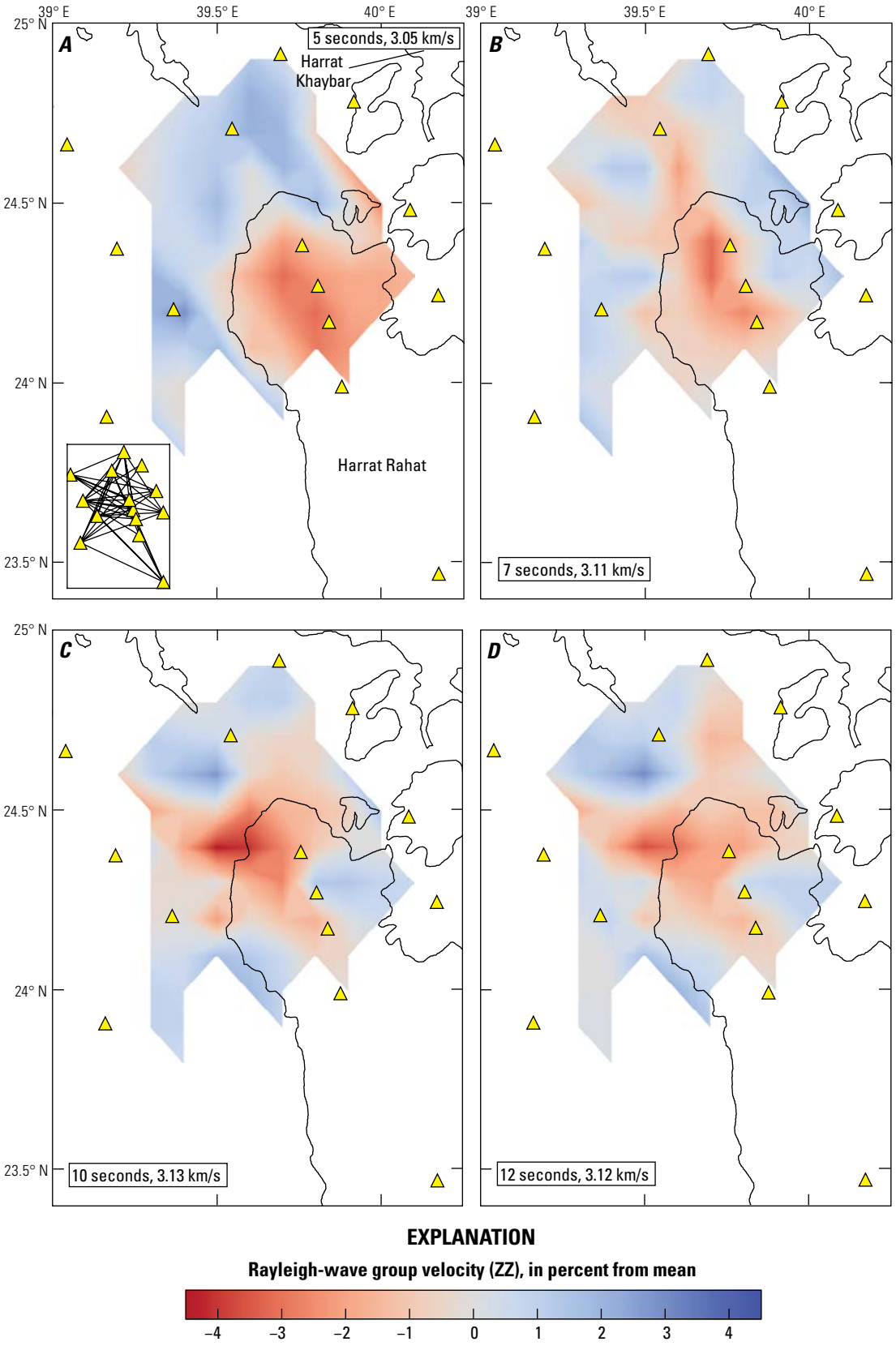

Figure 2.7. Maps of the northern Harrat Rahat area showing Rayleigh-wave group velocity as a percentage difference from the mean using vertical-vertical (ZZ) cross correlations (40 station paths) for 5-second (*A*), 7-second (*B*), 10-second (*C*), and 12-second (*D*) periods. Harrat Rahat seismic stations are marked as yellow triangles, and the borders of nearby harrats are shown as black lines. The length of period and mean velocity, in kilometers per second (km/s), for each subplot are displayed in an inset, and station paths are displayed in an inset in the lower left corner of part *A*. Figures 1 and 13 in the main text show the name and positions of harrats (outlined in black) near Harrat Rahat on the Arabian Shield.

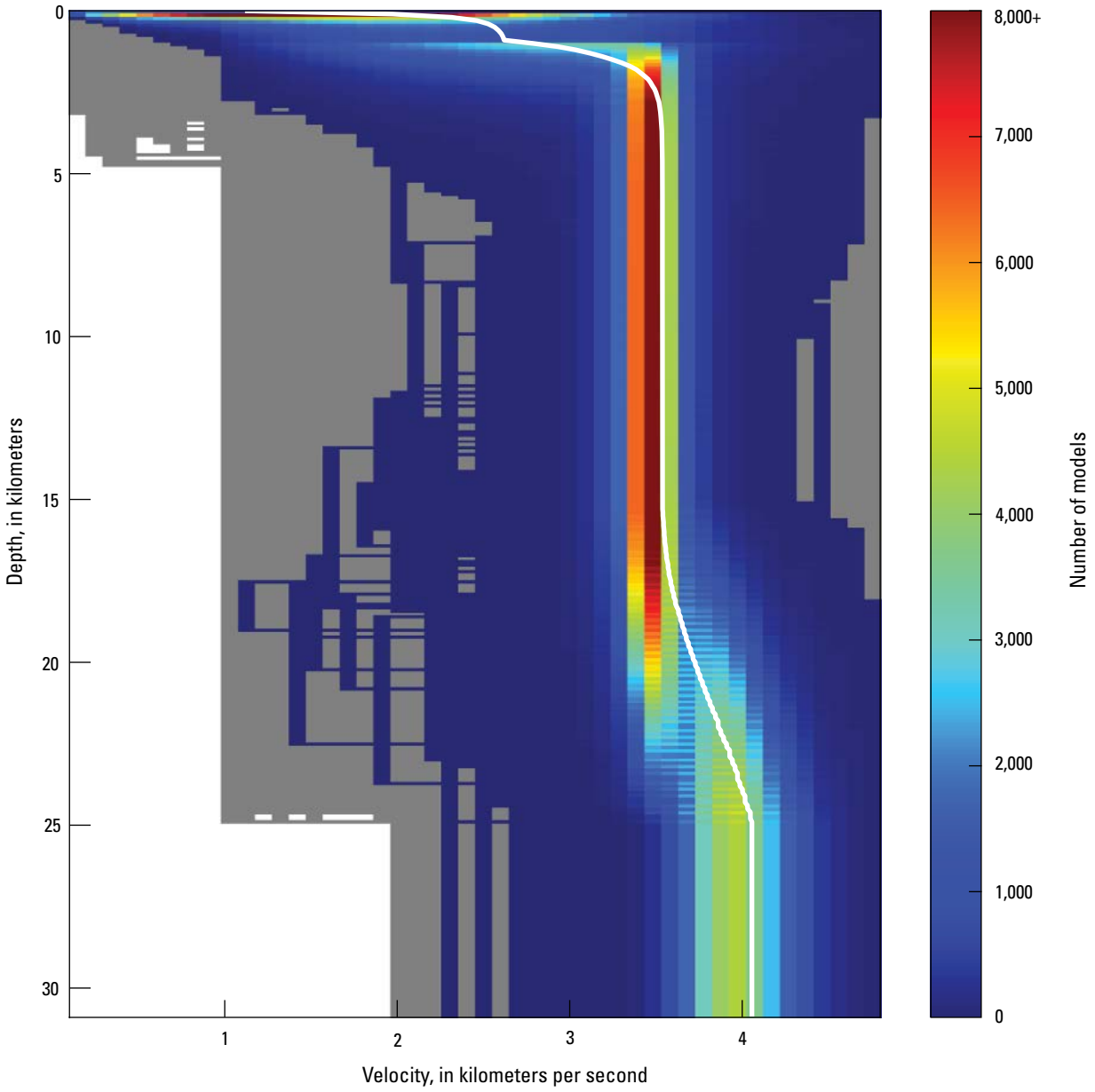

Figure 2.8. Graph showing shear-wave velocity inversion at lat 24.4° N., long 39.6° E. from Rayleigh-wave phase velocities using the radial-radial correlation. The weighted mean is displayed as a solid white line. Gray areas represent models below the misfit threshold.

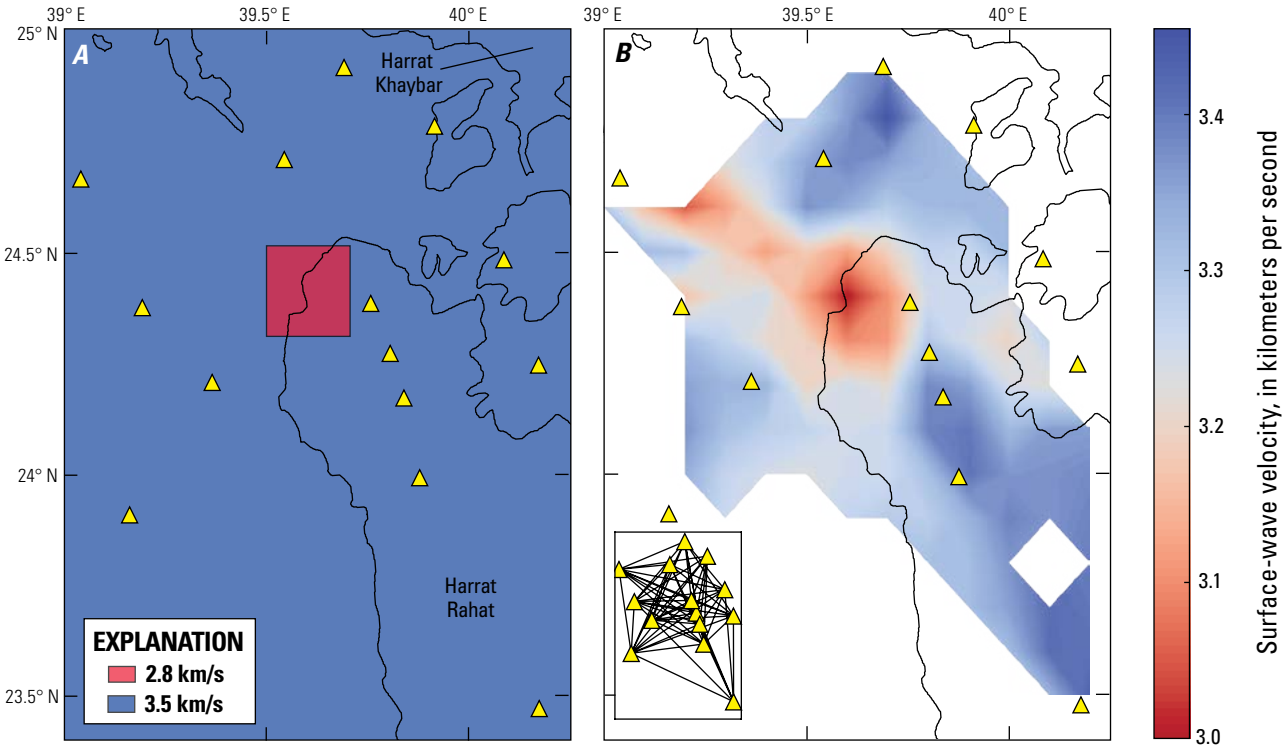

Figure 2.9. Maps of the northern Harrat Rahat area showing the checkerboard model (*A*) and surface-wave velocity (*B*), in kilometers per second (km/s), for a 0.2° x 0.2° slow-velocity feature using radial-radial phase velocity paths (60 station paths). Harrat Rahat seismic stations are marked as yellow triangles, and the borders of nearby harrats are shown as black lines. Station paths are displayed in an inset in the lower left corner of part *B*. Figures 1 and 13 in the main text show the name and positions of harrats (outlined in black) near Harrat Rahat on the Arabian Shield.

Appendix 3. Arabian Shield Additional Tables

Table 3.1. Tabulated minimum and maximum velocity boundaries used in the all-paths velocity threshold exclusion and the resulting number of cut dispersion curves.

[km/s, kilometer per second; RR, radial-radial; TT, transverse-transverse; ZZ, vertical-vertical]

Wave type	Minimum velocity (km/s)	Maximum velocity (km/s)	Cut dispersion curves
RR phase	2.9–3.2	3.5–4.0	15
TT phase	3.2–3.4	3.8–4.6	37
ZZ phase	2.9–3.2	3.5–4.0	30
RR group	2.7–2.9	3.4–3.7	187
TT group	2.7–3.0	3.8–4.2	47
ZZ group	2.7–2.9	3.4–3.7	117

Table 3.2. Parameters used in the Dinver inversion software.

[V_P, compressional-wave velocity; V_S, shear-wave velocity; km/s, kilometers per second; g/cm^3, gram per cubic centimeter; km, kilometer; —, not applicable]

Layer	V_P (km/s)	V_S (km/s)	Density (g/cm^3)	Interface depth (km)
Layer 1	2.00–6.50	1.16–3.76	2.67–2.73	0.5–5.0
Layer 2	5.50–7.00	3.18–4.05	2.67–2.73	10–25
Layer 3	5.75–7.25	3.39–4.14	2.67–2.92	15–30
Layer 4	6.25–7.50	3.53–4.24	2.86–2.92	30–40
Layer 5	6.50–8.50	3.67–4.80	2.86–2.92	35–50
Halfspace	7.50–8.50	4.21–4.78	3.2	—

Appendix 4. Arabian Shield Additional Figures

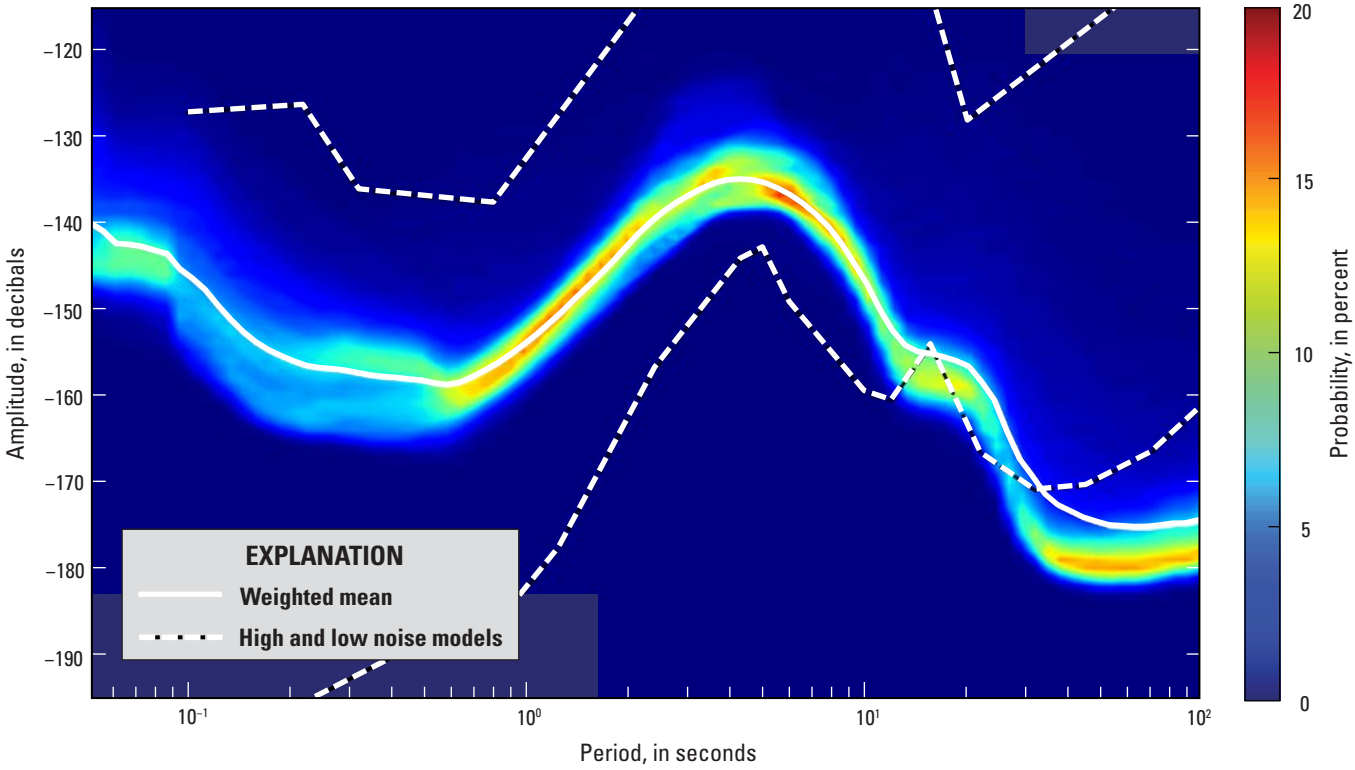

Figure 4.1. Diagram showing the probability density functions of station AFFS, vertical component. Each function is computed using the program PQLX (McNamara and Boaz, 2011) and the probability distribution is provided by the color bar. The new high and low noise models of Peterson (1993) are displayed as dashed lines.

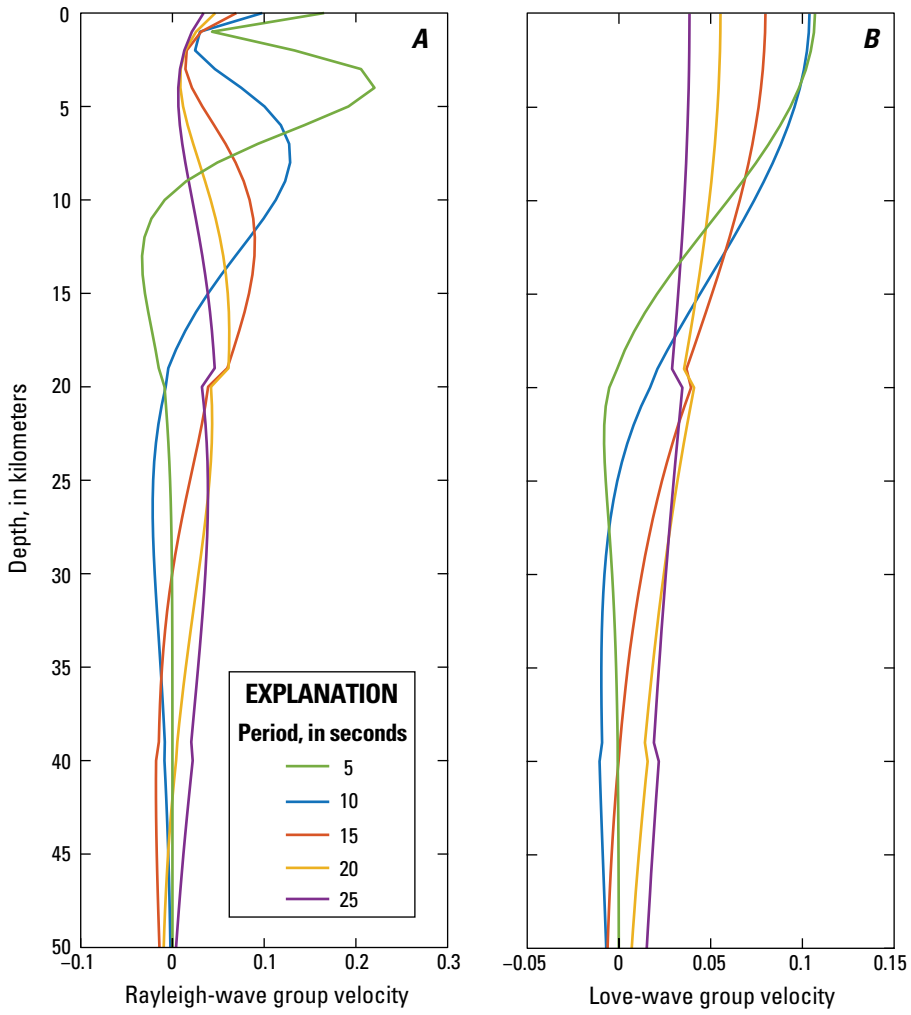

Figure 4.2. Graphs of Rayleigh-wave (*A*) and Love-wave (*B*) group velocity sensitivity kernels computed using the Senskernel software package (Levshin and others, 1989; Levshin, 2013).

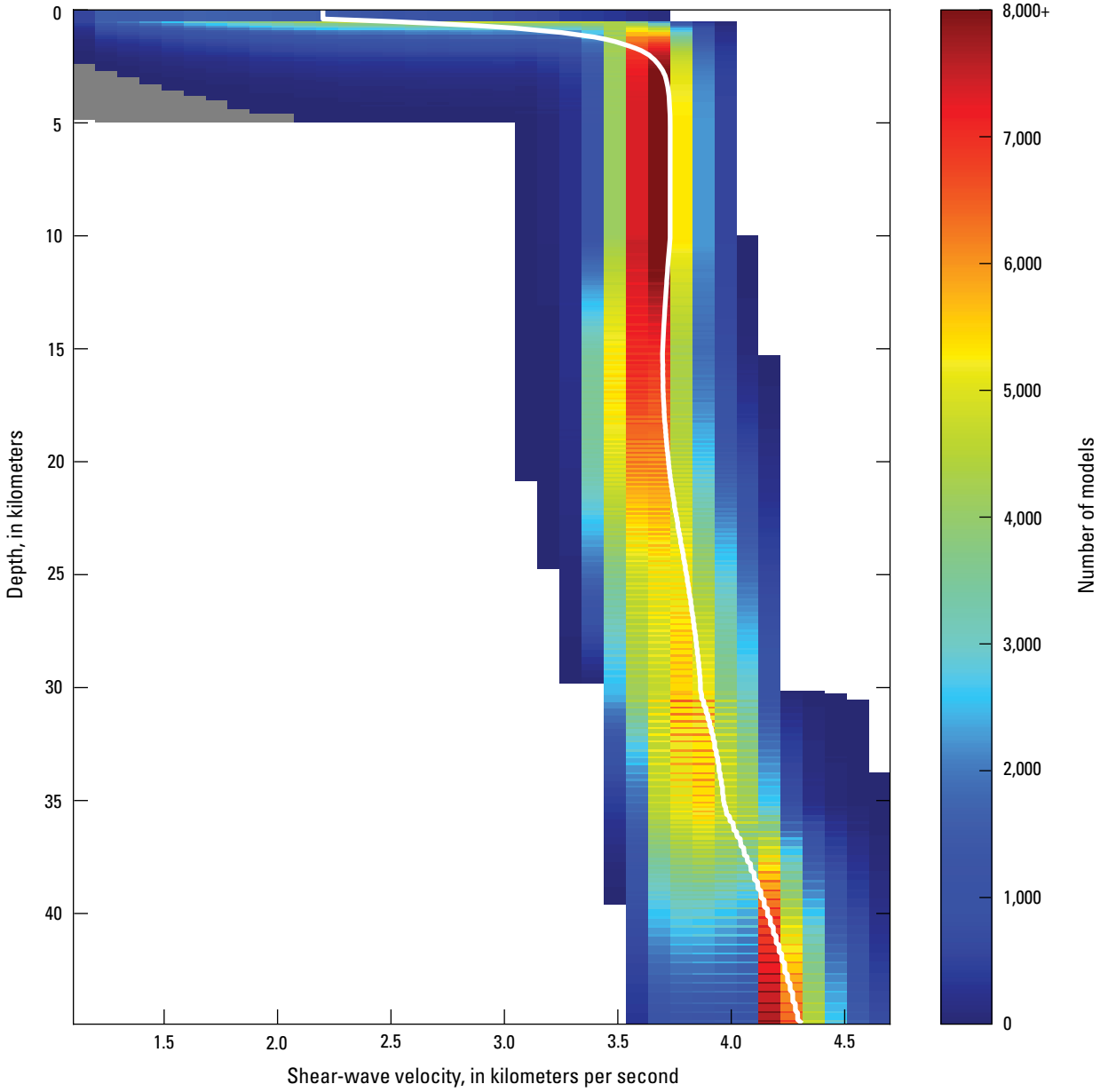

Figure 4.3. Graph showing shear-wave velocity using Dinver software inversions for the point at lat 23° N., long 41° E. The weighted mean is displayed as a solid white line. Gray areas represent models below the misfit threshold.

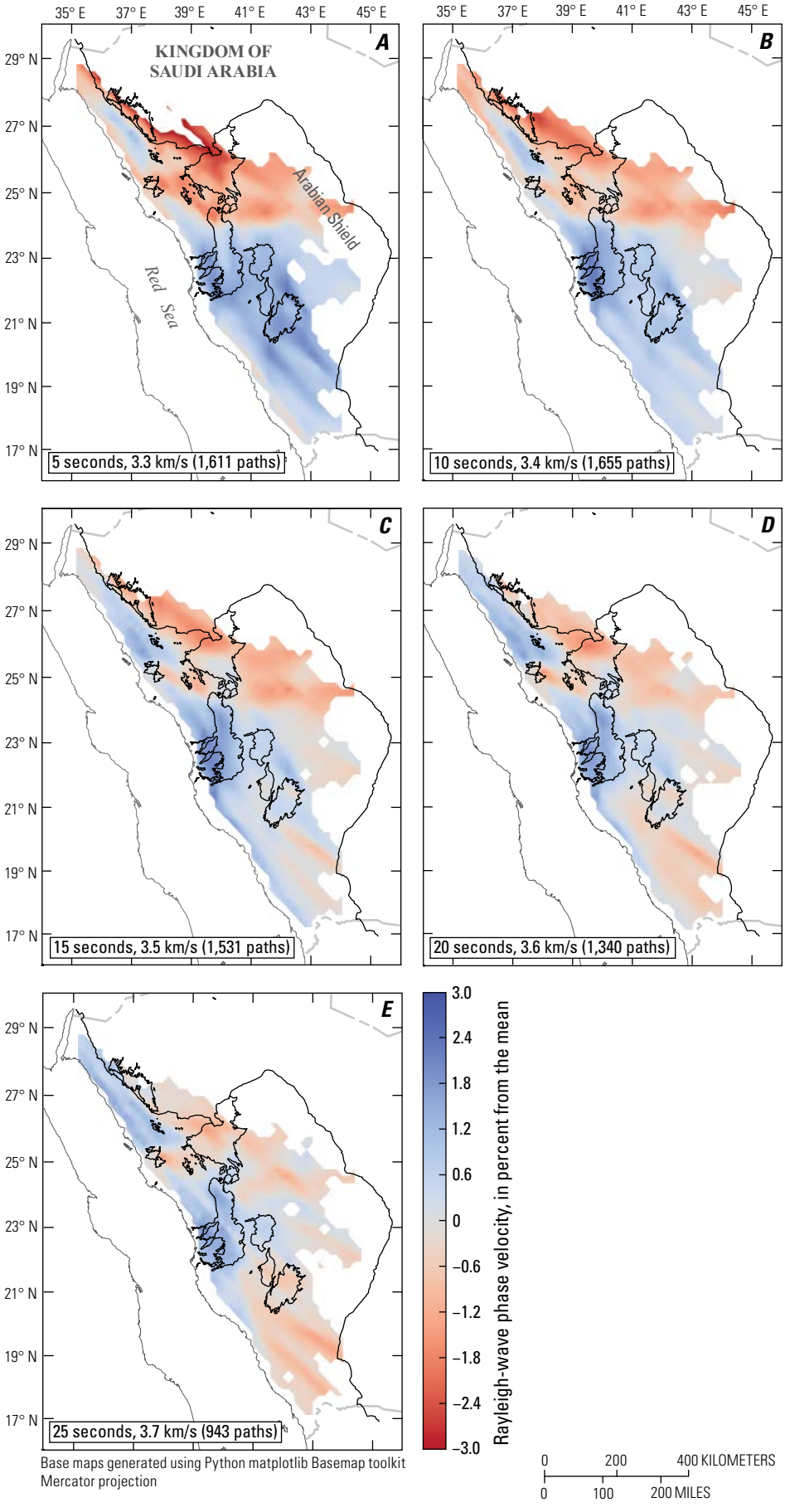

Figure 4.4. Maps of the northern Harrat Rahat area showing Rayleigh-wave phase-velocity as a percentage from the mean from the radial-radial cross-correlated component for 5- (*A*), 10- (*B*), 15- (*C*), 20- (*D*), and 25-second (*E*) periods. The period length, mean velocity, in kilometers per second (km/s), and number of station paths for each period are listed in insets.

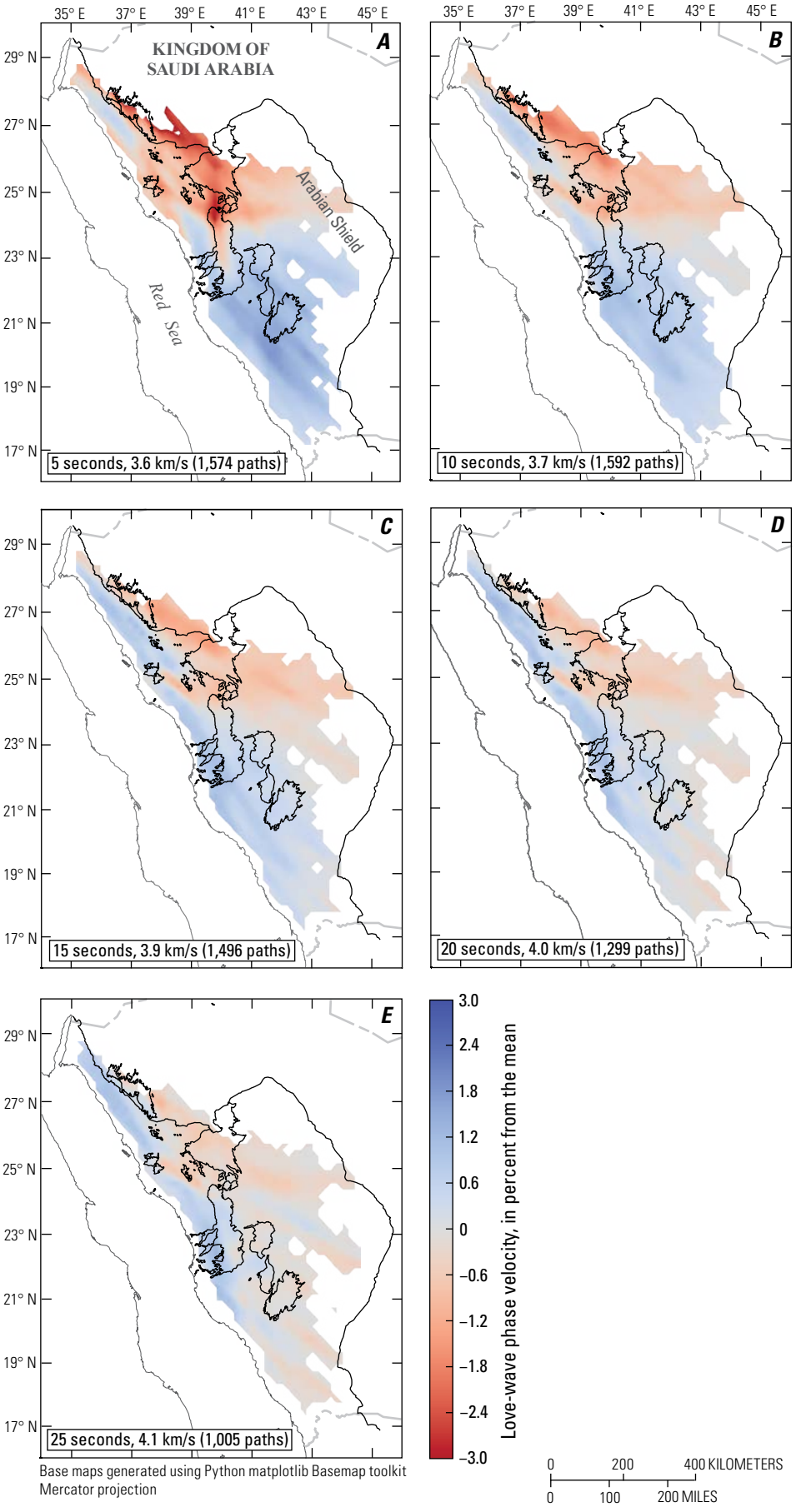

Figure 4.5. Maps of the northern Harrat Rahat area showing Love-wave phase-velocity from the transvers-transverse cross-correlated component for 5- (*A*), 10- (*B*), 15- (*C*), 20- (*D*), and 25-second (*E*) periods. The period length, mean velocity, in kilometers per second (km/s), and number of station paths for each period are listed in insets.

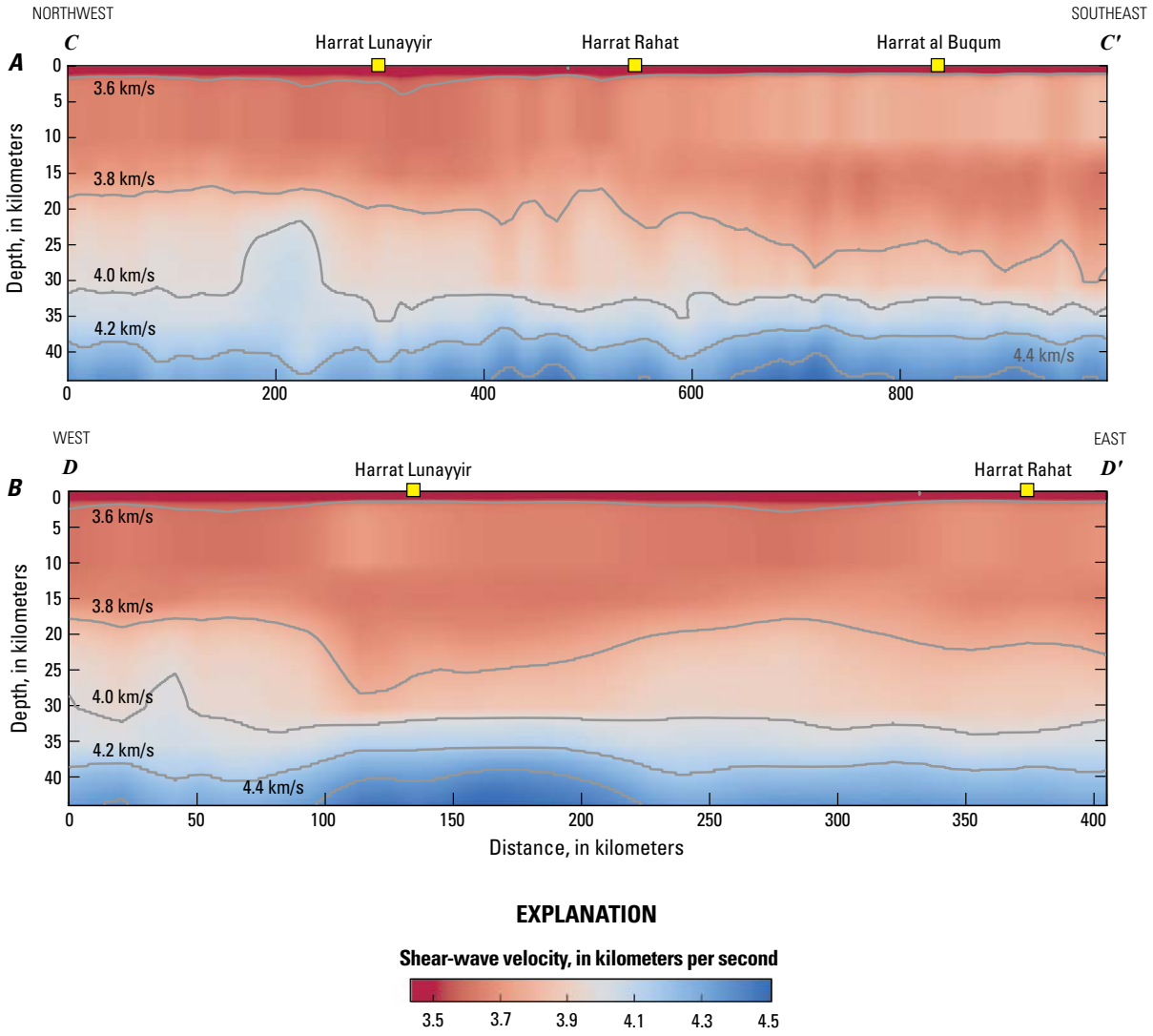

Figure 4.6. Cross sections *C*–*C*′ (*A*) and *D*–*D*′ (*B*) showing shear-wave velocity from an inversion of Love waves (transverse-transverse component). Individual harrat markers are shown as yellow squares on *A* and *B*, and locations of cross sections are shown on figure 23*A* in the main text.

Moffett Field Publishing Service Center, California
Manuscript approved August 30, 2022
Edited by Phil Frederick
Layout and illustration support by Cory Hurd

USGS

Civilini and others—**Ambient Seismic Noise Tomography of the Kingdom of Saudi Arabia**—Professional Paper 1862–N

ISSN 2330-9612 (print)
ISSN 1044-7102 (online)
https://doi.org/10.3133/pp1862N